



University of Tennessee, Knoxville
**TRACE: Tennessee Research and Creative
Exchange**

Doctoral Dissertations

Graduate School

8-2005

Fatigue Behavior of a Zirconium-Based Bulk Metallic Glass

William Hutchison Peter
University of Tennessee, Knoxville

Follow this and additional works at: https://trace.tennessee.edu/utk_graddiss

 Part of the [Materials Science and Engineering Commons](#)

Recommended Citation

Peter, William Hutchison, "Fatigue Behavior of a Zirconium-Based Bulk Metallic Glass. " PhD diss., University of Tennessee, 2005.
https://trace.tennessee.edu/utk_graddiss/4364

This Dissertation is brought to you for free and open access by the Graduate School at TRACE: Tennessee Research and Creative Exchange. It has been accepted for inclusion in Doctoral Dissertations by an authorized administrator of TRACE: Tennessee Research and Creative Exchange. For more information, please contact trace@utk.edu.

To the Graduate Council:

I am submitting herewith a dissertation written by William Hutchison Peter entitled "Fatigue Behavior of a Zirconium-Based Bulk Metallic Glass." I have examined the final electronic copy of this dissertation for form and content and recommend that it be accepted in partial fulfillment of the requirements for the degree of Doctor of Philosophy, with a major in Materials Science and Engineering.

Raymond A. Buchanan, Peter K. Liaw, Major Professor

We have read this dissertation and recommend its acceptance:

Chain T. Liu, Charlie R. Brooks, Charles S. Feigerle, Easo P. George

Accepted for the Council:

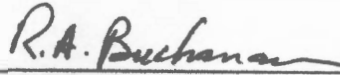
Carolyn R. Hodges

Vice Provost and Dean of the Graduate School

(Original signatures are on file with official student records.)

To the Graduate Council:

I am submitting hereby a dissertation written by William Hutchison Peter entitled "Fatigue Behavior of a Zirconium-Based Bulk Metallic Glass." I have examined the final paper copy of this dissertation for form and content and recommend that it be accepted in partial fulfillment of the requirements for the degree of Doctor of Philosophy, with a major in Materials Science and Engineering.



Raymond A. Buchanan,
Co-Major Professor



Peter K. Liaw
Co-Major Professor

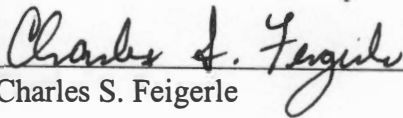
We have read this dissertation and recommend its acceptance:



Chain T. Liu



Charlie R. Brooks

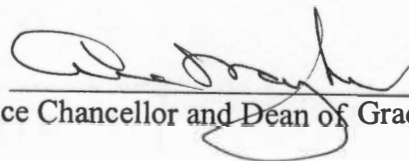


Charles S. Feigerle



Easo P. George

Accepted for the Council:



Vice Chancellor and Dean of Graduate Studies

Thesis
2005b
.P46

**FATIGUE BEHAVIOR OF A ZIRCONIUM-BASED BULK
METALLIC GLASS**

**A Dissertation Presented for the
Doctor of Philosophy Degree,
The University of Tennessee, Knoxville**

**William Hutchison Peter
August 2005**

DEDICATION

This dissertation is dedicated to my wife, Whitney S. Peter, for providing me an opportunity to return to graduate school, supporting my endeavors, and believing in my dreams; my sons, Hutchison R. Peter and Hayden W. Peter, for the inspiration to be as wise a father as possible and to set standards of higher education for my legacy; my parents, Wilbur H. Peter III and Janis L. Peter, for their love, values, support, and beliefs; my brother, David B. Peter, for his competitive spirit, devotion, and love; my grandmother, Doris B. Peter, for inspiring in all of her grandchildren the pursuit of the highest education (all of her grandchildren have received a post-graduate degree); my late grandmother, Margaret A. Hutchison, for encapsulating all that is good in humanity; my late grandfather, Wilbur H. Peter, Jr., for showing me how to enjoy life; my late grandfather, Ira B Hutchison, for the aspiration to be a grandson he could be proud; my father- and mother-in-law, Earl and Libby Sharp, for their encouragement; and the rest of my family and friends, for their love and support.

ACKNOWLEDGMENTS

Foremost, I would like to thank my two advisors, Drs. Ray Buchanan and Peter Liaw, whom I have had the great pleasure to study under. Their guidance, advice, and time have allowed me the opportunity to work in a very exciting field. I could not have asked for two more effective mentors.

Dr. Buchanan has been especially influential in the development of my love for materials science. He has taught me to approach science with an open mind, respect, inquiry, morality, and most of all passion. To date, I have not met a professor whom better epitomizes the importance of the evolution of knowledge from teacher to student. He is a great mentor, boss, and friend.

Dr. Liaw has been an irreplaceable guide in the importance of communication. Throughout my experience at the University of Tennessee, Dr. Liaw has been my biggest advocate for publishing my results, making outside contacts for collaborative research, early grant and proposal experience, and taking every opportunity possible to effectively present my research to leading scientists. The experience and knowledge I received from both of these men, I will cherish and utilize on a daily basis in my career and life.

I am particularly grateful to Dr. C. T. Liu presently at the University of Tennessee and formerly at the Oak Ridge National Laboratory (ORNL). I have been provided an extraordinary opportunity to study under his guidance, to become acquainted with leading scientists associated with his own work and research, and to use his research facilities. Dr. Liu provided advice on countless issues and provided the basis of the research topic

of this dissertation. He has taught me the importance of focusing the direction of research and making sure the end result is practical for application.

I would like to thank Drs. Charlie Brooks, Charles Feigerle, and Easo George at the University of Tennessee for agreeing to be on my dissertation committee, and the advice they provided me for my studies. I have known each of these talented and knowledgeable scholars and scientists since the beginning of my five years at the University of Tennessee. They were vital to ensuring my dissertation and research remained noteworthy, significant of science, methodic, and respectable to a degree in the doctor of philosophy.

There are several students that provided me with considerable help. Mr. Mark Morrison provided me with several samples, performed some of the corrosion tests used in my results, and worked closely with me to setup experiments in both corrosion and fatigue. Specifically, he and I worked closely in the testing of three and four point bend specimens. Mr. Seth Lawson has aided me in the polishing of my samples; he performed the hardness testing on my hydrogen charged specimens, and he will continue my work on developing composite bulk metallic glasses by performing compression and fatigue testing. Mr. Gongyao Wang has continued to work parallel with me in the study of bulk metallic glasses and their fatigue properties. On numerous occasions, we have shared results, he has helped me set up the load frame for mechanical testing, and we have provided advice to one another. Ms. Brandice Green has worked with me to perform corrosion tests of bulk metallic glasses in various electrolytes and with various processing conditions. Ms. Rejanah Steward has also provided advice and conducted complimentary

work in corrosion and fatigue. I would like to thank the rest of the IGERT and IMI NSF student participants for their help and advice regarding many aspects of my research.

I greatly appreciate Dr. Akihisa Inoue and Dr. Dmitri Louzguine for hosting me at the Institute of Materials Research, Tohoku University, Sendai, Japan. They graciously allowed me access to their facilities and equipment. Both provided me with valuable advice for the two months that I was in Japan. The Zr-based composite research could not have been performed without their help.

I would like to thank Drs. Roberto Benson, Hahn Choo, Joseph Spruiell, Takeshi Egami, David Joy, and Tai-Gang Nieh of the University of Tennessee; Drs. Joe Horton, Michael Brady, Ken Liu (formerly), Joachim Schneibel, and Sean Agnew (formerly) of Oak Ridge National Laboratory; Drs. Gary Harlow, and Robert Wei of Lehigh University; and Dr. Mitsunori Denda of Rutgers University for providing guidance and advice in each of their respective areas of expertise. Their perspectives helped develop areas of my research that I had not considered or that I did not have the wisdom to explain. I greatly appreciate the technical support and help of Mr. Cecil Carmichael, Jr., of ORNL; and Ms. Carol Winn, Mr. Greg Jones, and Mr. Doug Fielden of the University of Tennessee. Fabrication and preparation of my samples would not have been possible without the help of these individuals. Mr. Carmichael was irreplaceable in providing me with the expertise and experience in fabricating my materials. He is a very patient, knowledgeable, and kind individual. Mr. Fielden provided countless parts, services and machining to research related materials and equipment. Mr. Greg Jones and Ms. Carol Winn were both receptive and fervent to help in the operation and maintenance of scientific apparatuses.

I would like to thank Elsevier, American Physical Society, Nature Publishing Group, and the Material Research Society for allowing me the opportunity to reprint previously published figures from their respective publications (see individual figures and references).

Lastly, I would like to thank the National Science Foundation Integrative Graduate Education and Research Training (IGERT) Program on Materials Lifetime Science and Engineering (DGE 9987548), managed by Dr. C. Van Hartesveldt, Dr. L. Clesceri, Dr. W. Jennings and Dr. L. Goldberg; and the Division of Materials Science and Engineering, Department of Energy under contract DE-AC05-00OR22725 with Oak Ridge National Laboratory (ORNL) operated by UT-Battelle, LLC. for support of this research. The National Science Foundation is an important institution in the development of many young scientists.

ABSTRACT

Although the mechanical behavior of Zr-based bulk metallic glasses (BMGs) has been studied, fatigue studies in controlled environments and testing conditions have not been adequately performed or understood. Early fatigue examinations of rectangular bar specimens tested in bending had resulted in fatigue strengths substantially lower than anticipated [1,2,3,4,5]. Preliminary work performed by Peter et al. and Wang et al. on uniaxial button-head specimens have yielded in very different fatigue behavior with fatigue-endurance limits comparable to conventional high-strength, crystalline alloys [6,7,8,9,10]. Between all S-N results studied, the fatigue-endurance limits for Zr-based BMGs have been observed to range from 150 MPa to 1 GPa [1,2,3,4,5,6,7,8,9,10]. Testing conditions, sample preparation, and the quality of the amorphous alloy may provide the understanding for this variability in fatigue behavior.

In the following thesis, several investigations were engaged to better understand changeability in the fatigue behavior of a Zr-based BMG, $Zr_{52.5}Al_{10}Ti_5Cu_{17.9}Ni_{14.6}$ (at. %). The studies were primarily conducted to explain how the loading conditions, the sample preparation, the quality of the glass materials, the test environment, or the chemical composition affect the degradation behavior of BMGs. Fabrication, corrosion, metallography, and cyclic loading were types of investigations performed.

Fatigue testing was conducted in air and vacuum environments. By comparing the results, the environmental effects due to water vapor (in air) on the fatigue lifetime of BMG-11 were evaluated. It was concluded that water vapor does not have a detrimental effect on the fatigue lifetime of BMG-11. Indeed, the observed lifetimes in vacuum were

shorter than those in air. Early fatigue tests in vacuum with and without the use of an ionization gauge seemed to indicate that the dissociation of the residual water vapor to atomic hydrogen in vacuum via a hot tungsten-filament ionization gauge could be a factor in the shorter fatigue lifetimes in vacuum than in air. Further testing has disproved this hypothesis. Closer examinations of the surface of multiple samples has led to the discovery of mechanical wear and fused copper (from copper grips) near the crack initiation site.

Because of the possible impact the ionization gauge may have had on the fatigue behavior of BMG-11, hydrogen-charged samples were tested in air and compared to uncharged samples in order to understand any detrimental effects hydrogen may have on the fatigue lifetime around the fatigue-endurance limit. Though the ionization gauge did not seem to play a detrimental role in the fatigue lifetime of amorphous samples tested in vacuum, charged hydrogen embrittles the material with increases in hardness values and lower fatigue lifetimes for cathodically-charged samples. These results could impact Zr-based BMGs' usefulness in hydrogen-rich environments.

Fatigue studies were performed on button head, uniaxial specimens with different surface finishes in order to better understand the influence the average surface roughness and/or critical surface defects may have on the fatigue behavior. It was hypothesized that geometric, surface flaws could lower the observed life of a BMG sample by shortening the crack initiation phase and providing local stress concentrators. Careful studies of surface conditions indicate that fatigue-endurance limits are greatly impacted by the average surface roughness with possible reductions over fifty percent. Lastly, a

rectangular bend-bar sample was finished with a coarse grit paper on the tension side of the sample, and observed for the location of crack initiation.

Four-point and three-point bending fatigue studies were conducted to observe the effect of variability in loading conditions versus uniaxial tension studies, and to observe any impact from testing volume on the fatigue life of BMG-11. Both, three point and four point bend results seemed to exhibit slightly better fatigue behavior compared to the uniaxial tests. However, little difference was observed between three- and four-point bending. These results are similar to those found with a preliminary study of uniaxial specimens with varying testing gauge lengths.

Lastly, a study was performed to better understand the effect crystallinity has on the fatigue behavior of Zr-based bulk metallic glasses. The crystalline phases of BMG-11 have an extremely low ultimate bending strength, around 100 MPa, and are very brittle. Any interfaces between crystalline impurities and the glassy matrix are prime locations for crack-initiation sites. A large volume fraction of crystallinity has been shown to dramatically lower the fatigue lifetime of a Zr-based BMG. This careful study of fatigue behavior leads to the conclusion that the detrimental effect crystallinity and geometrical surface defects have on the fatigue-endurance limit and the fatigue lifetime explain the variability in previously reported results.

TABLE OF CONTENTS

Chapter/Section	Page
CHAPTER 1: INTRODUCTION	1
CHAPTER 2: REVIEW OF LITERATURE	6
2.1 History of Amorphous Alloys	6
2.2 Microstructure	8
2.2.1 <i>Atomic Ordering</i>	8
2.2.2 <i>Early Modeling of an Amorphous Alloy</i>	8
2.2.3 <i>Modeling of Atomic Arrangements in Metallic Glasses</i>	9
2.2.4 <i>Preferential Chemical Ordering</i>	10
2.2.5 <i>Possibility of Spinodal Decomposition in a Glass</i>	11
2.2.6 <i>Amorphous States in Solid Ceramics Compared to Alloys</i>	11
2.3 Fabrication	12
2.3.1 <i>Importance of Alloying</i>	12
2.3.2 <i>Eutectic Compositions</i>	13
2.3.3 <i>Cooling Rate Parameters</i>	14
2.3.4 <i>Amorphous Alloys to Metallic Glasses</i>	15
2.3.5 <i>Bulk Metallic Glasses</i>	15
2.3.6 <i>Complications in BMG Casting</i>	16
2.4 Corrosion Resistance of Metallic Glasses	19
2.4.1 <i>Corrosion Behavior of a Zr-Based Bulk Metallic Glass</i>	20
2.4.2 <i>Author's Studies of Cyclic Polarization Curves in 0.6 M NaCl</i>	20
2.5 Mechanical Behavior	28
2.5.1 <i>Monotonic Fracture</i>	29
2.5.2 <i>Monotonic Fracture Morphologies</i>	33
2.5.3 <i>Environmental Effects on Tensile Fracture</i>	36
2.5.4 <i>Fracture Toughness</i>	37
2.5.5 <i>Cyclic Fatigue and Fracture</i>	38
2.5.6 <i>Fatigue Morphology</i>	43
2.5.7 <i>Environmental Effects on Fatigue</i>	43
2.6 Critical Issues	45
CHAPTER 3: EXPERIMENTAL PROCEDURES	48
3.1 General Overview of Experiments Conducted	48
3.2 Sample Preparation and Material	50
3.3 Production of Bulk Metallic Glass Composites	52
3.4 Dynamic Polarization Curves with Scratch Testing in 0.05 M Na₂SO₄	54
3.5 Cyclic Polarization Curves in 0.6 M NaCl of Pre-Etched BMG Samples	56
3.6 Hydrogen-Charging Samples for Fatigue Testing	56
3.7 Tensile-Tensile, Uniaxial Fatigue Testing In Air of Notched Button-Head Samples	58
3.8 Tensile-Tensile, Uniaxial Fatigue Testing In Vacuum of Notched Button-Head Samples	59

3.9	Tensile-Tensile, Uniaxial Fatigue Testing In Air of Notched Button Head Samples with Various Surface Finishes.....	60
3.10	Fatigue Testing of BMG Button Head Samples with Different Test Gauge Lengths (Changing the Area and Volume Tested)	61
3.11	Three- and Four-Point Bend Fatigue Testing In Air of Rectangular Beam Specimens	61
3.12	Scanning Electron Microscopy	63
CHAPTER 4: RESULTS AND DISCUSSION		64
4.1	Amorphous Structure and Fabrication	64
4.2	Production of Bulk Metallic Glass Composites.....	65
4.3	Polarization Curves and Scratch Testing in 0.05 M Na ₂ SO ₄	67
4.3.1	<i>Cyclic Polarization Curve in 0.05 M Na₂SO₄</i>	67
4.3.2	<i>Dynamic Polarization Curve with Scratch Tests in 0.05 M Na₂SO₄</i>	67
4.4	Comparison of Vacuum and Air Fatigue Behavior	68
4.4.1	<i>Results</i>	68
4.4.2	<i>Discussion</i>	69
4.4.3	<i>Scanning Electron Microscopy of Button-Head Uniaxial Specimens</i>	73
4.4.4	<i>Observed Striation Spacings Compared to Stress Intensity Ranges</i>	79
4.5	Fatigue Results of Hydrogen-Charged Samples	82
4.6	Limited Fatigue Results of Varying Testing Gauge Length	87
4.7	Fatigue Results of Varying Surface Finish	88
4.7.1	<i>Results</i>	88
4.7.2	<i>Crack Initiation from a Critical Geometric Flaw</i>	90
4.8	Fatigue Results of Three- and Four-Point Bending and Comparing These With Uniaxial Results.....	91
4.8.1	<i>General Results and Discussion</i>	91
4.8.2	<i>Crystallinity and the Its Effect on Bend Testing of BMGs</i>	93
CHAPTER 5: CONCLUSIONS		97
CHAPTER 6: FUTURE RESEARCH & INTEREST		103
REFERENCES.....		105
APPENDIX.....		119
VITA.....		188

LIST OF TABLES

Table	Description	Page
A-1	Polarization Curve Properties for Amorphous and Crystalline BMG-11 Tested in 0.6 M NaCl.	120
A-2	BMG-11 Element Amounts.	121
A-3	Crystallization Temperature for Variations of BMG-11 with Additions of Pd.	121
A-4	Polarization Curve Properties for Amorphous BMG-11 Tested in 0.05 M Na ₂ SO ₄ .	122
A-5	U.S. Grit Number Convention Versus Surface Roughness for BAM-11.	122
A-6	Reduction of Fatigue Endurance Limit for Conventional, High-Strength Steels and BAM-11.	123
A-7	Hardness of Hydrogen-Charged BAM-11 Button-Head Samples.	123

LIST OF FIGURES

Figure	Description	Page
A-1	Relationship of Glass Transition Temperature, with Cooling Rates, and Sample Thickness.	124
A-2	Bernal's Steel Ball Model.	124
A-3	A Two-Dimensional Representation of a Dense Cluster-Packing Structure.	125
A-4	Two Dimensional Concentration Map of Pd-Based BMG.	125
A-5	Phase Diagram of Zirconium-Nickel with Glass Forming Ranges Identified.	126
A-6	TTT Diagram Illustrating the Glass Transition Temperature, the Liquidus Temperature, and the Critical Cooling Rate.	126
A-7	TTT Diagram Illustrating Various Heating Rates on the Crystallization Temperature of a Metallic Glass.	127
A-8	Many of the Possible Fabrication Methods Prior to 1990.	127
A-9	As-Cast 6.4 mm Diameter Specimen of BMG-11 ($Zr_{52.5}Al_{10}Ti_5Cu_{17.9}Ni_{14.6}$, at. %) and the Mold Used for Casting.	128
A-10	BSE Images of Pure and Commercial Grade BAM-11 Near Center of Ingot.	128
A-11	SEM Image of Porosity on the Fracture Surface of a Fatigue Specimen Caused by Trapped Inert Gas During the Drop-Casting of a Zr-Based BMG.	129
A-12	SE Image of Radial Machine Marks And a Large Geometric Defect on the Outside Surface of a Round Bar Fatigue Specimen.	129
A-13	Optical Micrograph Image of Etched BMG-11 As-Cast 6.4 mm Diameter Specimen Illustrating Small Bands of Crystallinity.	130
A-14	Corrosion Rates of Amorphous and Crystalline Cu-50Zr Alloy in Various Environments.	130

A-15	Optical Photomicrograph of An As-Cast BMG-11 Sample.	131
A-16	Optical Photomicrograph of Crystalline BMG-11 After Annealing Treatment at 600°C for Five Hours.	131
A-17	X-Ray Diffraction Patterns Taken from Amorphous and Crystalline BMG-11 Samples.	132
A-18	X-Ray Diffraction Patterns Taken from Two Different Crystalline BMG-11 Samples.	132
A-19	Schematic Cyclic-Anodic-Polarization Curves.	133
A-20	Average Cyclic-Anodic-Polarization Behaviors of Amorphous and Crystalline BMG-11 with 600-Grit Surface Finish in Aerated 0.6 M NaCl Solution at Room Temperature.	133
A-21	Results of Electrochemical Parameters for Cyclic-Anodic-Polarization Tests of Amorphous and Crystalline BMG-11 with 600-Grit Surface Finish.	134
A-22	Average Cyclic-Anodic-Polarization Behaviors of Amorphous and Crystalline BMG-11 with Metallographically-Polished Surface Finish in Aerated 0.6 M NaCl Solution at Room Temperature.	134
A-23	Results of Electrochemical Parameters for Cyclic-Anodic-Polarization Tests of Amorphous and Crystalline BMG-11 with Polished Surface Finish.	135
A-24	Secondary Electron Image of Amorphous Corrosion Sample After Being Tested in 0.6 M NaCl Solution.	135
A-25	Secondary Electron Image of the Porosity in the Amorphous Corrosion Sample After Being Tested in 0.6 M NaCl Solution.	136
A-26	Back-Scattered Electron Image of Porosity in the Amorphous Corrosion Sample After Being Tested in 0.6 M NaCl Solution.	136
A-27	Secondary Electron Image of a Pit in a Crystalline Corrosion Sample After Being Tested in 0.6 M NaCl Solution.	137
A-28	Back-Scattered Electron Image of a Pit in a Crystalline Corrosion Sample After Being Tested in 0.6 M NaCl Solution.	137

A-29	“Illustration of an individual atomic jump, the basic step for macroscopic diffusion and flow.”	138
A-30	Shear Band Near Crack Tip.	138
A-31	SEM of an Overload Fracture Surface of a Zirconium-Based BMG.	139
A-32	Secondary Electron Image of the Overload Fracture Surface of a Zr-Based Metallic Glass.	139
A-33	Tensile Fracture Surface of Amorphous ZrAlCuPd Alloy with Varying Percents of Volume Fraction (V_f) of Nanocrystallization.	140
A-34	Fracture Toughness Versus Anneal Time.	140
A-35	SEMs of an Overload Fracture Surface for a Metallic Glass and 5% Crystallized Sample.	141
A-36	Fatigue Crack Growth Results for $Zr_{41.2}Ti_{13.8}Cu_{12.5}Ni_{10}Be_{22.5}$ BMG, 300-M Ultrahigh Strength Steel, and 2090-T81 Aluminum Lithium Alloy.	141
A-37	S-N Testing Results for $Zr_{41.2}Ti_{13.8}Cu_{12.5}Ni_{10}Be_{22.5}$ BMG, 300-M Ultrahigh Strength Steel, and 2090-T81 Aluminum Lithium Alloy.	142
A-38	BMG-11 Specimen Geometry for Fatigue Testing in Air and Vacuum.	142
A-39	Stress-Range / Fatigue-Life Data of Notched BMG-11 Specimens Tested in Air and Compared with the Fatigue Endurance Limits of High-Strength Alloys.	143
A-40	Stress-Range / Fatigue-Life Data of Various BMGs.	143
A-41	Stress-Range/Fatigue-Life Data of Notched $Zr_{41}Ti_{14}Cu_{12}Ni_{10}Be_{23}$ Specimens Tested in Air with $R = 0.1$ and a Frequency of 10 Hz.	144
A-42	Secondary Electron Image of Shear Steps in an Overload Fracture Surface.	144
A-43	SE Image of an Overload Fracture Surface for a Metallic Glass Illustrating Vein Morphology.	145
A-44	Secondary Electron Image of the Division Between the Fatigue (Left) and Overload (Right) Fracture Surfaces.	145

A-45	Fatigue-Crack Growth Rates in Amorphous $Zr_{41.2}Ti_{13.8}Cu_{12.5}Ni_{10}Be_{22.5}$ for Various Stress Intensity Ranges in Three Environments.	146
A-46	Fatigue-Crack Growth Rates at Constant $\Delta K = 1.5 \text{ MPa(m)}^{0.5}$ in Amorphous $Zr_{41.2}Ti_{13.8}Cu_{12.5}Ni_{10}Be_{22.5}$ in 0.5 M NaCl.	146
A-47	BMG-11 Sample After Mixing by Arc Melting, but Before Drop Casting.	147
A-48	The Initial BMG-11 Specimen Geometry for Fatigue Testing in Air and Vacuum.	147
A-49	Volume / Surface Area Specimen Geometries for Uniaxial Fatigue Testing.	148
A-50	Four-Point Bending Setup, Three-Point Bending Setup, and Beam Geometry for Fatigue Studies.	148
A-51	Amorphous Sample with Crystal Starlet Spiral.	149
A-52	X-Ray Diffraction Patterns of As-Cast 2 mm Diameter Ingots of a $Zr_{52.5}Ni_{14.6}Al_{10}Ti_5Cu_{(17.4-Y)}Pd_Y$, at. %, BMG where Y is 2.5, 5, 7.5, or 10.	149
A-53	X-Ray Diffraction Pattern of As-Cast 6 mm Diameter Ingot of a $Zr_{52.5}Ni_{14.6}Al_{10}Ti_5Cu_{10.4}Pd_{7.5}$, at. %, BMG.	150
A-54	Differential Scanning Calorimetry of As-Cast 2 mm Diameter Ingot of a $Zr_{52.5}Ni_{14.6}Al_{10}Ti_5Cu_{15.4}Pd_{2.5}$, at. %, BMG.	150
A-55	X-Ray Diffraction Pattern of 2 mm Diameter Ingot of a $Zr_{52.5}Ni_{14.6}Al_{10}Ti_5Cu_{15.4}Pd_{2.5}$, at. %, BMG After Annealing for Ten Minutes at the Crystallization Temperature.	151
A-56	X-Ray Diffraction Pattern of 2 mm Diameter Ingot of a $Zr_{52.5}Ni_{14.6}Al_{10}Ti_5Cu_{13.9}Pd_5$, at. %, BMG After Annealing for Ten Minutes at 20° K Above the Crystallization Temperature.	151
A-57	Anodic-Polarization Behaviors of Amorphous BMG-11 in Aerated 0.05 M Na_2SO_4 Solution at Room Temperature with the Surface Undisturbed.	152
A-58	Anodic-Polarization Behaviors of Amorphous BMG-11 in Aerated 0.05 M Na_2SO_4 Solution at Room Temperature.	152

A-59	Stress-Range / Fatigue-Life Data of Notched BMG-11 Specimens Tested in Air and Vacuum with $R = 0.1$ and a Frequency of 10 Hz.	153
A-60	Stress-Range / Fatigue-Life Data of Notched BMG-11 Specimens Tested in Air and Vacuum With the Results of the Fracture Location.	153
A-61	Schematic Illustrating Possible Atomic Hydrogen Production and Absorption into the BMG.	154
A-62	Stress-Range / Fatigue-Life Data of Notched BMG-11 Specimens Tested in Air and Vacuum, Comparing Results of the Samples Tested with the Ionization Gauge On and with the Ionization Gauge Off.	154
A-63	Stress-Range / Fatigue-Life Data of Notched BMG-11 Specimens Tested in Air and Vacuum with All the Present Diversifications.	155
A-64	SE Image of the Side of a Fractured Fatigue Specimen, Tested in Vacuum.	155
A-65	Secondary Electron Image of Copper Smearred Near the Crack Initiation Site.	156
A-66	Secondary Electron Image of Oxide Near Copper Grip Location of Sample Tested in Air.	156
A-67	Energy Dispersive Spectrum Map for K_{α} Copper Energy Level of the Outside Surface of the Round Bar Specimen.	157
A-68	Secondary Electron Image of All Three of the Distinct Fracture Morphologies.	157
A-69	Secondary Electron Image Illustrating Large and Mid-Size Striations.	158
A-70	Secondary Electron Image of Side Profile of Beam Specimen.	158
A-71	Secondary Electron Image Illustrating Mid-Size and Small Striations.	159
A-72	Secondary Electron Image of Mirror-Like Surface Near Crack Initiation Location.	159
A-73	Secondary Electron Image of the Vein Morphology Present in the Overload Fracture Surface of Sample 1 After Fatigue Test at 698 MPa.	160

A-74	Secondary Electron Image of the Vein Morphology Present in the Overload Fracture Surface of Sample 1 After Fatigue Test at 698 MPa.	160
A-75	Backscattered Electron Image of the Overload Fracture Surface of Sample 2 After Fatigue Test at 977 MPa.	161
A-76	Backscattered Electron Image of the Vein Morphology on the Shear Lip of Sample 2 After Fatigue Test at 977 MPa.	161
A-77	Backscattered Electron Image of the Vein Morphology and a Liquid Droplet on the Shear Lip of Sample 2 After Fatigue Test at 977 MPa.	162
A-78	Secondary Electron Image of the Fatigue Fracture Surface Around the Crack Initiation Site of Sample 1 After Fatigue Test at 698 MPa.	162
A-79	Secondary Electron Image of the Crack Initiation Site of Sample 1 After Fatigue Test at 698 MPa.	163
A-80	Backscattered Electron Image of the Crack Initiation Site of Sample 1 After Fatigue Test at 698 MPa.	163
A-81	Secondary Electron Image of a Crack Branching in the Low Area of the Planar Area of Sample 1 After Fatigue Test at 698 MPa.	164
A-82	Secondary Electron Image of the Area Surrounding the Crack Initiation Site of Sample 1 After Fatigue Test at 698 MPa.	164
A-83	Secondary Electron Image of the Outer Surface of the Crack Initiation Site at a 10° Tilt of Sample 1 After Fatigue Test at 698 MPa.	165
A-84	Secondary Electron Image of the Fracture Surface of Sample 2 at Low Magnification After Fatigue Test at 977 MPa.	165
A-85	Secondary Electron Image of the Crack Initiation Site of Sample 2 After Fatigue Test at 977 MPa.	166
A-86	Secondary Electron Image of the Protrusion in Proximity of the Crack Initiation Site of Sample 2 After Fatigue Test at 977 MPa.	166
A-87	Backscattered Electron Image of the Plateau of the Protrusion of Sample 2 After Fatigue Test at 977 MPa.	167

A-88	Backscattered Electron Image of the Dimpling Found on the Top of the Plateau of Sample 2 After Fatigue Test at 977 MPa.	167
A-89	Backscattered Electron Image of the Area Surrounding the Protrusion of Sample 2 After Fatigue Test at 977 MPa.	168
A-90	Backscattered Electron Image of Striations Near the Protrusion of Sample 2 After Fatigue Test at 977 MPa.	168
A-91	Backscattered Electron Image of the Crack Initiation Site of Sample 2 After Fatigue Test at 977 MPa.	169
A-92	Secondary Electron Image of the Depression of Sample 2 After Fatigue Test at 977 MPa.	169
A-93	Secondary Electron Image of Crack Branching at Bottom of Depression of Sample 2 After Fatigue Test at 977 MPa.	170
A-94	Secondary Electron Image of Crack Branching of Sample 2 After Fatigue Test at 977 MPa.	170
A-95	Backscattered Electron Image of Crack Branching of Sample 2 After Fatigue Test at 977 MPa.	171
A-96	Secondary Electron Image of Crack Branching of Sample 2 After Fatigue Test at 977 MPa.	171
A-97	Secondary Electron Images of Crystals in an As-Cast Amorphous Alloy.	172
A-98	Optical Microscopy Image of Crystalline Band in Polished and Etched BMG-11 Sample And Secondary Electron Image of Fracture Surface of Fatigue Sample Tested in Air.	172
A-99	Secondary Electron Images of Air Sample Tested at 907 MPa for $N_f = 282,785$ Cycles, and Vacuum Sample Tested at 750 MPa for $N_f = 5.8$ Million Cycles.	173
A-100	Crack Striation Spacings for Small, Medium, and Large Striations of Two Samples Tested in Air Versus the Stress Intensity Range Divided by Young's Modulus.	173
A-101	Crack Growth Rates for Small Striations of Two Samples Tested in Air Versus the Stress Intensity Range.	174

A-102	Secondary Electron Images of Fatigue Striations.	174
A-103	Stress-Range / Fatigue-Life Data of Notched BMG-11 Specimens Tested in Air, but Cathodically-Charged with Hydrogen.	175
A-104	Secondary Electron Image of Crack Initiation Surface of a Specimen Tested in Air, but Cathodically-Charged with Hydrogen.	175
A-105	Secondary Electron Image of the Fatigue Surface of a Specimen Tested in Air, but Cathodically-Charged with Hydrogen.	176
A-106	Secondary Electron Image of Overload Fracture Surface of a Specimen Tested in Air, but Cathodically-Charged with Hydrogen.	176
A-107	Secondary Electron Image of a Shear Lip of a Specimen Tested in Air, but Cathodically-Charged with Hydrogen.	177
A-108	Stress-Range / Fatigue-Life Data of Notched BMG-11 Specimens Compared with Specimen Geometries A and B, and Gilbert et al.'s Results.	177
A-109	Relative Locations of Crack Initiation/ Fracture Surface for Geometry A and Geometry B.	178
A-110	Surface Roughness, R_a , Versus Particle Size of Silicon Carbide Grinding Paper for BMG-11.	178
A-111	Surface Roughness, R_a , Versus U.S. Designated Grit Number of Silicon Carbide Grinding Paper for BMG-11.	179
A-112	Comparing the Stress-Range / Fatigue-Life Data of Notched BMG-11 Specimens Tested in Air with Various Finishes.	179
A-113	Fatigue Endurance Limit Versus the Surface Finish for BAM-11.	180
A-114	Secondary Electron Image of Crack in a Square Beam, 3-Point Bend Specimen Finished with 180 Grit Paper.	180
A-115	Secondary Electron Image of the Two Crack Initiation Locations in a Square Beam, 3-Point Bend Specimen Finished with 180 Grit Paper.	181
A-116	Secondary Electron Image of the Severe Crack Branching that Occurs to a Square BMG-11 Beam Tested in 3-Point Bending with 180 Grit Paper Finish.	181

A-117	Stress-Range / Fatigue-Life Data of 3-Point Bending, 4-Point Bending, and Uniaxial BAM-11 Specimens Tested in Air.	182
A-118	Stress-Range / Fatigue-Life Data of 3-Point Bending and, 4-Point Bending.	182
A-119	Stress-Range / Fatigue-Life Data of 3-Point Bending and 4-Point Bending BMG Specimens Tested in Air Designating Whether the Sample Came from the Top or the Bottom of the Ingot.	183
A-120	Secondary Electron Image of Fracture Surface in the Fatigue Region of 3-Point Bend Specimen that Failed Near 13,000 Cycles.	183
A-121	An In-Lens, Secondary Electron Image of the Surface Finish Near the Corner of a Polished Beam Specimen Before Testing.	184
A-122	Stress-Range / Fatigue-Life Data of 3-Point Bending, 4-Point Bending and Uniaxial BAM-11 Specimens Tested in Air with Low Results from Samples Made Using New Arc Furnace.	184
A-123	Optical Micrographs of Two Samples Tested at 1,100 MPa and Compared with a BMG-11 Sample that Underwent 1 M Cycles at 900 MPa.	185
A-124	Optical Micrographs and X-Ray Diffraction Patterns of Two Samples Tested at 1,100 MPa and Compared with a BMG-11 Sample that Underwent 1 M Cycles at 900 MPa.	185
A-125	Optical Micrograph, X-Ray Diffraction Pattern, and Secondary Electron Image of the Sample Tested at 1,100 MPa and Failed at 8,552 Cycles.	186
A-126	Secondary Electron Images of Fatigue Area of Fracture Surface of Specimen T4.	186
A-127	Optical Micrograph, X-Ray Diffraction Pattern, and Secondary Electron Image of the Sample Tested at 1,100 MPa and Failed at 9,562 Cycles.	187

NOMENCLATURE

A	ampere
at. %	atomic percent
E_{corr}	corrosion potential
T_x	crystallization temperature
i	current density
$^{\circ}\text{C}$	degrees celsius
σ_L	fatigue endurance limit
S-N	fatigue stress - life
GPa	giga-pascals
T_G	glass transition temperature
Hz	hertz
K	kelvin
R	load ratio
MPa	mega-pascals
T_M	melting temperature
M	meter
μm	micrometer
mA	milliamp
mm	millimeter
mV	millivolts
M	molar
N	number of cycles
Pa	pascal
%	percent
E_{pit}	pitting potential
E_{pp}	protection potential
s	second
cm^2	square centimeter
σ	stress
ΔK	stress intensity range
$\Delta\sigma$	stress range
V	volt
wt. %	weight percent

Abbreviations

Al	aluminum
BSE	back-scattered electron
Be	beryllium
BAA	bulk amorphous alloy
BAM	bulk amorphous metal
BMG	bulk metallic glass

C(T)	compact test specimen
Cu	copper
H ₂ O	distilled water
EDM	electrical discharge machine
Au	gold
D ₂ O	heavy water
Li	lithium
MTS	material test system
Ni	nickel
ORNL	Oak Ridge National Laboratory
OM	optical microscope
Pd	palladium
ppm	parts per million
SCE	saturated calomel electrode
SHE	saturated hydrogen electrode
SEM	scanning electron microscope
SE	secondary electron
Si	silicon
SiO ₂	silicon oxide
NaCl	sodium chloride
Na ₂ SO ₄	sodium sulfate
TTT	temperature-time-transition
Ti	titanium
Zr	zirconium

CHAPTER 1: INTRODUCTION

Though it has been a decade and a half since the development of "bulk metallic glasses" (BMGs), amorphous alloys with fabrication diameters larger than 1 mm [11,12], and half a century since the development of amorphous alloys in general, the development of new chemical-based bulk amorphous alloy systems, and their new exciting properties has continued to generate scientific interest. Metallic glasses are alloys with no long-range and limited short-range atomic ordering [13]. Their atomic bonding continues to be metallic, but the structure is amorphous, similar to a metal in its liquid state. This condition provides metallic glasses with remarkable properties.

Traditionally, amorphous metals have been used mainly in the commercial field of electronics. Their soft magnetic properties have impelled metallic glass into such uses as transformers, transducers, magnetic shielding, delay lines, magnetic heads, and security systems [14]. Historically, fabrication limitations have kept the thickness of manufactured specimens below one millimeter [11,12] with the majority of metallic glasses fabricated prior to the last two decades having an average sample thickness of fifty micrometers [15]. The size limitation does not pose a large problem for soft magnetic production as it was used, but it does limit other fields of applications. In the early 1990s, a large break-through in innovative alloy compositions allowed the production of metallic glasses with thickness over one millimeter [11,12]. These new compositions have been labeled "Bulk Metallic Glasses" (BMGs), "Bulk Amorphous Alloys" (BAAs), or "Bulk Amorphous Materials" (BAMs). Since then, samples have

been produced with diameters up to eighty millimeters [11], and many other systems of BMGs have been developed (e.g. Iron, Copper, Nickel, Titanium, etc).

Bulk metallic glasses have exhibited extraordinary properties. Strength and toughness values of bulk metallic glasses are much greater when compared to the alloy's crystalline phase [11,2], and are comparable to conventional high-strength alloys. Zr-based BMGs have shown an ultimate tensile strength between 1.7 and 2 GPa [16,17], and recently, Fe-based BMGs have shown compression strengths above 4 GPa [18]. The fracture toughness of $Zr_{41.2}Ti_{13.8}Cu_{12.5}Ni_{10}Be_{22.5}$ BMG is $55 \text{ MPa}\sqrt{\text{m}}$ [1,3]. These alloys have low Young's moduli that result in incredible elastic properties, around 90 GPa for most Zr-based BMGs. Certain BMG components have experienced two percent tensile strain without any macro-plastic deformation [16]. Initial corrosion studies have shown that, in general, amorphous metals containing at least two metallic elements are more corrosion resistant than their crystalline counterparts [19,20]. However, the complete role that the amorphous structure plays in corrosion resistance has not been identified. Historically, the amorphous state creates alloys with densities slightly lower than the same alloy crystallized, 0.5 to 2 percent reduction [21]. Hardness values are good for most compositions. In a Vicker's hardness test, a Zr-based BMG had a hardness value of 500 kg/mm^2 [22]. Several studies on wear properties have been performed, and report decent wear properties [23,24].

The exciting characteristics and the ability to manufacture in much larger sizes have led to BMGs being used in new commercial applications. Currently, applications in the biomedical, automotive, aircraft, and sports industries are being investigated. BMGs are being used for casings of electronic equipment, hinges for cellular phones,

components of tennis racquets, watch cases, other jewelry, armor piercing ammunition, and surgical blades. Their ability for net-shape fabrication, similar to polymer fabrication, is promising; eliminating the requirements of expensive machining and polishing required for other fabricated alloy components. New commercial applications warrant more detailed and comprehensive research. Most of these applications place the bulk metallic glass components in structural conditions.

Therefore, the lifetime science of these advanced materials must be studied. Answers need to be ascertained to such questions as: “How will bulk metallic glass components handle long-term fatigue?”, “Do mechanisms in metallic glasses leading to failure occur more in the manner of a metal or a glass?”, and “How does the environment affect the lifetime of these materials?”. Understanding the mechanisms that lead to monotonic loading failure is a highly researched subject at the present date. However, only a handful of schools have studied the cyclic loading behavior of bulk metallic glasses. Arguably, this area could be more important in study than monotonic loading since BMGs have reported good tensile strengths [16,17,18], early fatigue studies showed low endurance limits [1,2,3,4,5], and most structural applications place the component in cyclic loading over large time periods.

The lack of bulk plastic deformation may indicate the possibility for a perfect amorphous alloy, without constraint, to exhibit a fatigue endurance limit that approaches the ultimate tensile strength [25]. This idealistic hypothesis has not been realized. Metallic glass fatigue samples have undergone six hundred loading cycles at 99% of the fracture strength with an R ratio (minimum stress divided by maximum stress) of 0 in tension [25]. This phenomenon is interesting compared to high-strength alloys that can

only sustain a few cycles at stress magnitudes approaching the ultimate tensile strength. However, the results of some fatigue testing on a $Zr_{41.2}Ti_{13.8}Cu_{12.5}Ni_{10}Be_{22.5}$ BMG have been quite different. One particular study has shown the fatigue-endurance limit for this BMG to be six to eight percent of the tensile strength [1,2,3,4,5]. Based on the above ideal belief, six to eight percent is an extremely low value. More recent studies conducted at the University of Tennessee have shown this same composition and other Zr-based alloys to have very good fatigue-endurance limits, comparable or higher than conventional crystalline materials [6,7,8,9,10]. Obviously, other factors must play a paramount role in affecting the fatigue behavior of amorphous metals.

The primary goal of this thesis is to resolve the variability within fatigue results of bulk metallic glasses. A literature survey is provided to adequately understand current issues at hand with BMGs. Then, an array of studies conducted for this thesis will be covered in order to better understand the fatigue behavior of BMGs. First, the fabrication and microstructure will be discussed since a large portion of this thesis went into the production of these glassy alloys. All samples were fabricated at the Oak Ridge National Laboratory (ORNL) or at the University of Tennessee, Knoxville (UT). This is an important note since few academic facilities can fabricate such glasses at the present time, and fabrication to testing in the same facilities and by the same individuals can implement a good deal of laboratory control otherwise not possible. Next, corrosion studies will be addressed to understand the electrochemical behavior. Corrosion studies were conducted in salt water (0.6 M NaCl), and water containing a small concentration of non-reacting salt (Na_2SO_4). The electrolytes and the sample preparation was arranged in

such a matter as to understand the effect the environment may have on the degradation of BMG samples under cyclic loading conditions.

Fatigue studies were the bulk of work performed in this thesis. Tests were conducted in various environments and loading conditions. Samples tested in air were compared with fatigue tests in vacuum to observe any detrimental effects that the air with humidity has on the degradation of BMGs. Humidity did not play a detrimental role in the degradation of BMG samples in air. In fact, lower lifetimes and more variability was observed in vacuum results. The possible effect of hydrogen embrittlement due to a tungsten filament used in an ionization gauge monitoring vacuum pressure was examined. A few fatigue specimens were cathodically-charged with hydrogen to understand if hydrogen embrittlement is a concern in fatigue of BMGs. Three-point and four-point bending studies were conducted and compared to results of uniaxial test specimens. Notched, uniaxial specimens were finished with different grinding papers to analyze the effect of average surface roughness on the fatigue behavior. This work also indicates the impact of severe flaws or machine markings on the lifetime of BMGs. Lastly, several fracture surfaces and corrosion samples after testing were observed under a scanning electron microscope (SEM) to help identify mechanisms that caused failure and to better understand the amorphous structure. The end result of these experiments was to better understand the variability in fatigue-endurance limits and the fundamental degradation of bulk metallic glasses.

CHAPTER 2: REVIEW OF LITERATURE

2.1 History of Amorphous Alloys

Prior to the last half century, humankind only recognized solid metal alloys as having a crystalline, or periodic, atomic structure [13]. This is largely due to the high fluidity, non-directional atomic bonding associated with molten alloys. Only in the last five decades has the notion of a metal with no crystal lattice and complete atomic disorder become apparent. Scholars have thought a nickel-based amorphous alloy had been fabricated using chemical deposition for the later part of the nineteenth century [26]. However, the absence of diffraction techniques could not prove whether the material was amorphous or crystalline. In 1960, Duwez documented the first procedure to produce a completely amorphous metal [13,26]. He attained an amorphous phase at room temperature in an Au-Si composition by quenching directly from the melt. His theory behind the experiment was if a metal cooled fast enough from a liquid, super-quenched, the metal would hold its liquid atomic arrangement at room temperature, and therefore, a solid alloy with an amorphous structure would be fabricated. The experiment was achieved by propelling a liquid alloy drop from a gun onto a thermally conductive surface [13]. The gun would propel the drop fast enough to spread it into a thin film when it hit the surface, and thus, achieve incredibly high cooling rates. After his effort was a success, other scientists set out to achieve amorphous alloys, with experiments similar to Duwez.

Since Duwez's accomplishment, many different metallic compositions have been made into amorphous alloys. However, cooling rates have historically been on the order

of 10^5 K/s to 10^8 K/s [11,12]. Figure A-1 illustrates some of the compositions and cooling rates [11]. *[All figures and tables are located in the Appendix.]* Because of the very high cooling rates, amorphous metal samples have been largely limited to specimens with diameters below one millimeter prior to the early 1990s [11,12]. However, several Pd-based and Pt-based compositions were developed by Chen and Turnbull in the 1960s with diameters between 0.5 mm and 5 mm [12,27,28], but the cost of production was not warranted for most applications, and these alloys' potentials were never realized. Amorphous alloys were fabricated by a diverse group of methods in the 1960s and 1970s. Electro-deposition, splat quenching, spray deposition, and powder fabrication are just a few methods used during this time period [29]. Upon the fabrication of certain amorphous alloys by ribbon and tape forming techniques, a new group of compositions were referred to as metallic glasses [15]. These techniques were the primary method of fabrication used in the mid-70s to the mid-80s.

In the last decade, new fabrication and composition approaches have caused the cooling rates to drop as low as 1 K/s, and specimen sample sizes have become as large as 80 millimeters [11]. Cast specimens of the new compositions are commonly referred to as "Bulk Metallic Glasses" (BMGs), "Bulk Amorphous Alloys" (BAAs), or "Bulk Amorphous Materials" (BAMs). With the recent advances in bulk fabrication, a more diversified and economical group of testing procedures have been accomplished. Mechanical testing and environmental effects have become consequential topics for study with the possibility of larger cross sections. Many metallic glasses can achieve higher fracture strengths, higher fracture toughness values, and longer life spans than their

crystallized counterparts [1,2,3,4,11]. These qualities support the newfound interest in BMGs for structural applications.

2.2 Microstructure

2.2.1 Atomic Ordering

Metallic glasses exhibit a limited local order [30,31,32,33,34]. The specific composition of the metallic glass will determine the amount of the local order obtained. The limited local order in amorphous metals is due to topological and chemical ordering. This order is usually small polyhedral formations. However, icosahedral (having 20 sides) clusters have been reported [31]. This is in agreement with hard sphere models by Miracle illustrating the possibility of having coordination numbers as large as 10 or 12 [31]. Computer simulation has shown icosahedral symmetry can be developed without having translation symmetry, and is therefore not like ordering found in crystallinity [35,36,37]. No long-range order is found in BMGs. However, medium-range ordering, or the extent of local ordering, is being investigated [31,33].

2.2.2 Early Modeling of an Amorphous Alloy

Two models were developed early to describe the atomic structure of metallic glasses: “continuous random network” and “microcrystalline” [35,38]. The former represents metallic glasses more closely since local order does not spontaneously grow when heat is applied. Bernal was the first to establish a model to prove the ability to form an amorphous metal based on “continuous random network” [39]. This model illustrates the elementary spatial and structural aspects of an amorphous metal at an atomic level, and is still often quoted in describing the atomic arrangement. Bernal set out to either prove or disprove the ability of non-directional spheres to form in a complete

state of chaos and maintain a high density/low volume. His first modeling work was with a football bladder, used because of its unusual shape, and steel balls to represent the atoms [39]. The balls were poured into the bladder. Then, rubber strips were tightly bound around the bladder to exert a compressive force, the bladder was kneaded to facilitate rearrangement, and a molten mineral wax was used to set the spheres [39]. The end result can be observed in figure A-2. Bernal found that the steel balls were completely random, and a high density was obtained [39]. Bernal's model did lack three important parameters that are present in metallic glasses: different size spheres representing the different atom sizes used in an alloy, the model spheres were hard which is not entirely accurate [39], and most importantly, the model lacked any chemical preferences of the arranged atoms. Since Bernal's original model, elaborate computer simulations have been used to simulate the packing of various-sized soft spheres. Pair correlation functions have been applied to these simulations, and have shown statistically preferred pairing [35]. This constitutes the local ordering. However, Bernal's model represents the essential topological characteristics of an amorphous metallic element at room temperature, and is still an important model for describing to the laymen the physical ability to arrange an alloy in an amorphous state.

2.2.3 Modeling of Atomic Arrangements in Metallic Glasses

More recent modeling has constructed clusters of solute ordered atoms surrounded by solvent atoms [31,33,34]. The solute clusters allow for the capacity of short-range ordering. However, the random positioning of solvent atoms around these clusters prevents any long range ordering. Historically, the short range order of the solute clusters has been thought to be icosahedral [31,32]. Recently, Daniel B. Miracle has

provided a structural model for metallic glasses, the dense cluster packing model [33], where up to three distinct solutes exist: primary face centered cubic packings, followed by secondary octahedral and tetrahedral clusters. Solute clusters are idealized as spheres. Solvent atoms lie in the first coordination shell of these solute clusters. Internal strains prevent any long range ordering. Figure A-3 is an illustration depicting this model. The model has been shown to correspond well with experimental radial distribution functions, and allows efficient, dense packing. The model also shows the ability for medium range ordering (~0.7 to 1.0 nm [33]) to occur in an amorphous alloy. Hufnagel has also recently commented about the existence of medium range ordering of metallic glasses and techniques that can be used to identify this ordering [40].

2.2.4 Preferential Chemical Ordering

Flores et al. [41], Damonte [42], and Asoka-Kumar et al. [43] performed positron annihilation spectroscopy on BMG samples. In a Zr-based BMG containing Ti ($Zr_{52.5}Ti_5Cu_{17.9}Ni_{14.6}Al_{10}$), Damonte and Asoka-Kumar et al. independently found a change in the chemical ordering around Ti atoms [42,43]. They also found a fluctuation of free space associated with particular atoms. Positron annihilation spectroscopy is the measure of time between the positron being implanted and then annihilated in a solid [41]. Positrons annihilate at a slower rate in areas of greater free volume (less surrounding electrons for annihilation). This would include locations such as vacancies, grain boundaries, and porosity for materials in general. For amorphous alloys, this includes larger volumes of free space where atoms cannot fit due to surrounding atoms' configurations, or "atomic scale open-volume regions" [44]. In Damonte's and Asoka-Kumar et al.'s research, they found greater amounts of free volume surrounding Zr, Ti,

and Al atoms than the free volume around Ni and Cu [42,43]. In another Zr-based BMG containing Ti ($Zr_{46.7}Ti_{8.3}Cu_{7.5}Ni_{10}Be_{27.5}$), Flores et al. found similar results [41]. Ti and Zr atoms were associated with higher amounts of free volume, and Be, Ni, and Cu were associated with being more tightly packed. Flores et al. also conducted positron annihilation spectroscopy on strained samples, and found that Zr was associated with larger amounts of free space at the expense of Ti [41]. The above research suggests that at an atomic level free space is not homogeneously dispersed; free space is associated with certain elements.

2.2.5 Possibility of Spinodal Decomposition in a Glass

The last atomic mechanism that departs from total disorder is local spinodal decomposition. Miller et al. performed atom probe studies on Pd-based metallic glasses [45]. They compared their experimental frequency distributions of one metallic glass ($Pd_{40.5}Cu_{40.5}P_{19}$) with binomial modeling and with the Pa model (a model based on the spinodal decomposition). Miller et al. found a significant deviation from the binomial modeling; in fact, the Cu and P distributions fit the Pa model more closely. Miller et al. also provided a two-dimensional concentration map illustrating Cu-enriched/P-depleted and P-enriched/Cu-depleted regions of a nanometer scale as shown in figure A-4. Though this research was not conducted on a Zr-based BMG, it proves the possibility of limited spinodal decomposition during solidification while still maintaining an amorphous structure.

2.2.6 Amorphous States in Solid Ceramics Compared to Alloys

A parallel between metals in an amorphous phase and silicate glasses (e.g., amorphous SiO_2), which have traditionally taken very little effort to form an amorphous

solid in many compositions, should exist. However, this parallel is limited. Glasses establish an amorphous phase naturally. Their covalent bonds greatly increase the amount of time required for atoms to rearrange [46]. The powers of these directional bonds are evident in the ability to blow and form glass with long cooling periods, and still sustain the same amorphous atomic structure. The bonds formed in most metals are not directional [47]. This makes them by nature less viscous during resolidification [46]. Prior to Duwez's experiments with Au-Si, a large debate was over the possibility of forming a metallic glass.

2.3 Fabrication

2.3.1 Importance of Alloying

In the fabrication of metallic glasses, the overall goal achieved is a solidified gas or liquid metal with atoms stabilized in an amorphous configuration. This is accomplished by quenching the liquid form fast enough that the atoms do not have sufficient time to rearrange into their crystalline form. Cooling rates play a major role in the fabrication of metallic glasses. Theoretically, any metal could be fabricated into a metallic glass if cooled fast enough [46]. However, today's cooling methods are not fast enough to restrain the high fluidities in single metallic elements at atmospheric pressure. By using two or more elements of varying atom sizes, the fluidity decreases, and there are longer atomic rearrangements for precipitation [46]. An important fact to keep in mind is that the glassy state of an alloy is a meta-stable phase. This is not the equilibrium state of the material, and therefore, the alloy would rather precipitate into a crystalline phase.

Historically, elements additional to the base metal have made up twenty percent or higher of the overall composition [48]. As described earlier, metallic glasses exhibit some limited local atomic order. Bernal's model represented a single metallic element with one atom size. Occasionally in this model, local tetrahedral atomic ordering was found. Each tetrahedral arrangement creates a void in a single element atomic structure. When the voids in Bernal's model are aggregated, twenty percent of the overall composition is void [48]. This simple correlation provides one insight into the importance of alloying in the fabrication of metallic glasses.

2.3.2 Eutectic Compositions

Although two or more elements are required to fabricate metallic glasses, this poses a complex condition. Each element to be alloyed may have a very different melting temperature, and tendency for crystallization. The two or more elements must not form a secondary phase during solidification. Therefore, those alloys that have the best glass forming abilities are systems with deep eutectic compositions [46]. Any precipitation introduces (a) crystalline phase(s) to the glass. Once a phase precipitates out of the solution, the chemical composition of the remaining alloy has changed and continued crystallization is likely. Some amorphous-crystalline composites have been formed, but they are limited and require special "diffusion-control" elements to prevent the entire glass from crystallization. Figure A-5, a Ni-Zr phase diagram, illustrates, by brackets, the percentage ranges at which a nickel-zirconium alloy would be ideal for forming a metallic glass [46]. Each addition of another element into the alloy increases the complexity of the glass forming process from the standpoint of heats of mixing between elements.

2.3.3 Cooling Rate Parameters

The three critical temperatures that are of great importance are the melting/liquidus temperature, the glass transition temperature, and the crystallization temperature [49,50,51]. The melting temperature, T_M , or liquidus temperature, T_L , is the temperature which signifies the transition from a liquid to a solid, or vice-a-versa. The glass transition temperature, T_G , is the temperature at which the alloy is considered as a glass where atoms have frozen into their amorphous state, and is physically marked by great increases in the viscosity [50]. However, the alloy will still become crystalline if held at or below this temperature for an indefinite period of time. In respect to cooling a melt alloy, the closer the glass temperature is to the melting temperature (the closer T_G/T_M is to one), the more likely the sample will become a metallic glass [49]. The crystallization temperature, T_X , is the temperature at which crystallization begins, devitrification, for a given heating/cooling rate and alloy composition. Figure A-6 is a Temperature-Time-Transformation (TTT) diagram illustrating the relationship between time and temperature [49]. The graph illustrates that if the material is held close to a temperature between the melting temperature and the glass transition temperature for any length of time, a crystal lattice will be formed. The time axis is on a log scale. This shows the importance of the time that it takes to get from the melting temperature to the glass transition temperature. The slowest, steady reduction in the temperature of an alloy that will still form a glass is referred to as the critical cooling rate [46]. Figure A-7 illustrates various heating rates for a given glassy alloy. Please note that higher heating rates provide higher crystallization temperatures. Over the last half century, the

transformation curve has steadily moved to the right as better glass forming alloys have been discovered.

2.3.4 Amorphous Alloys to Metallic Glasses

Figure A-8 lists most of the possible fabrication techniques prior to 1990 [29]. Splat quenching was the test method used by Duwez [13,29]. The most common three methods of forming a metallic glass prior to the 1990s were by filament, ribbon, or tape extraction. All three methods involved extracting a hot melt through an orifice onto a thermally conductive plate, usually made of copper, spinning or conveying at moderate to high speeds [29]. Filaments were extracted in short sections. Ribbons were extracted in greater lengths by pressing the melt through a circular orifice in a continuous fashion and cooling the melt quickly by rotating the plate at a high velocity. The speed of the plate helped the cooling process. The last common method, tapes, was performed much like ribbons, but instead of a circular orifice, the orifice was a slit allowing for wide specimens.

2.3.5 Bulk Metallic Glasses

Since 1990, three empirical rules have been followed that have allowed for large increases in sample sizes [11,12,16]. The three rules are:

- 1) multi-component of three or more elements,
- 2) significant difference in atomic size ratios (>12%),
- 3) and negative heats of mixing.

These three empirical rules have led to alloys with longer required time for atomic rearrangements leading to precipitation, lower atomic mobility, higher viscosity, larger glass transition temperature to melting temperature ratios, lower critical cooling rates,

and much larger test specimen diameters. Diameters have been reported as large as eighty millimeters [11]. The increase in size has allowed for commercial fabrications and applications. Valid fracture toughness testing, stress-lifetime curves, and studies of crack initiation, propagation, and failure are now possible. A surge of fracture mechanics research has been conducted on metallic glasses in just the last few years.

The manufacturing process for BMGs uses conventional concepts, but greater control over the fabrication environment is required. The alloying elements are first arc-melted in an inert gas, such as argon. They are then mixed together in their liquid state. While still liquid, the sample is squeezed, dropped, injected, or vacuum cast into a copper mold where it is cooled. After solidification, the sample is possibly machined, then polished, and finally inspected for any irregularities or flaws. A metallic glass has a unique mirror-like appearance immediately after casting compared to many crystalline alloys. Zirconium-based BMGs are still some of the best glass forming alloys since zirconium atoms have a large atom size; this allows for significant differences in atomic ratios.

2.3.6 Complications in BMG Casting

Casting of metallic glasses is a good fabrication technique for creating sample sizes large enough for possible mechanical application for research, commercial, and industrial components (figure A-9 is an as-cast Zr-based BMG ingot and the copper mold used for casting). However, the casting method introduces complications. Some of these complications or imperfections of casting are discussed below.

Trace amounts of oxygen are still present in the arc melting and casting environment. Since several of the used elements are good oxidizers (i.e., Zr and Ti),

oxide impurities are present in most cast BMG samples. The amount of oxygen is dependent on the oxidizing characteristics of the elements, the purity level of the elements used, and the purity level of the “inert gas”. High amounts of oxygen are known to cause crystallization [52]. Liu et al. compared a pure alloy (PA) Zr-based BMG, as would be made in a controlled research environment, with a commercial grade alloy (CA) of the same chemical composition [52]. The difference between the CA and the PA was the purity level of the zirconium used. The as-cast oxygen content for the CA and PA BMGs were ~3,000 ppm and ~590ppm, respectively. After etching the samples, Liu et al. observed the alloys under both optical and electron microscopy. No crystallization or grains were observed in the PA material, but grains of significant size (~ 10 μm) were found in the CA material. Figure A-10 shows SEM images of the CA and PA material. It is the author’s feeling that even smaller amounts of oxygen may change the scale of the short-range atomic order and introduce localized areas of long-range order in the vicinity of the oxygen.

An experienced furnace operator should be able to thoroughly melt all pure elements into a well-mixed molten alloy. However, elements with higher melting temperatures still may be found unalloyed in small pockets from time to time. An inhomogeneous appearance and shrinkage of the ingot/button usually are indicators that the alloy is not sufficiently mixed. Very small pockets of unalloyed material may not cause shrinkage and may result in an amorphous material except at the particular location.

Squeeze, drop, and injection casting methods all introduce porosity to the molten alloy. The inert gas that is backfilled into the furnace chamber gets incorporated into the

molten alloy while mixing and dropping. During solidification, some of these gas bubbles escape and others do not. In the case of injection or squeeze casting, the inert gas is used to push the melt out of the injection quartz tube. Likewise, the injection gas gets trapped into the molten alloy, and some may not escape solidification. Some of this porosity is visible to the naked eye and may be up to a few millimeters. Porosity in Zr-based BMGs has the appearance of a small concave mirror when exposed by cutting or fracture. Figure A-11 is an example of the porosity in an as-cast Zr-based BMG.

Machining marks are great locations for crack initiation and propagation for glassy materials depending on the shape of the indentation [53]. Most as-cast ingots are machined using an EDM, a lathe, SiC grinding paper, or some other tool to shape the BMGs into testing specimens or into commercial, structural components themselves. Therefore, machining is required, and creating a perfect polish after machining is not time and/or monetarily effective. Since BMGs are brittle materials (no bulk plastic deformation), grinding marks may be even more effective in initiating cracks than in crystalline alloys. The shape of the grind mark may also create a localized stress concentration. If the indentation from machining comes to a sharp enough point, the local stress state may be sufficient to cause yielding even though the nominal stress is below the yield stress [54]. All materials are susceptible to crack initiation from surface marks or scratches, and most failures initiate from the surface [54]. However, glassy materials have great reductions in their strength from surface defects when discussing tensile loading, even compared to other materials [53]. Figure A-12 is an SE image of both machine marks and a large geometric defect.

Lastly, small bands of crystallinity may be found usually within the outside area of the cast ingot cross section. However, the location can vary depending on the quality of the glass/sample. Figure A-13 is an example of crystallinity in an otherwise amorphous alloy. The chemistry of these micro-crystallites will vary with the composition of the BMG. These small bands of crystallites are from the interface of the molten alloy and the copper mold. The area percentage of these crystallites with respect to the total cross-sectional area of an ingot is very small, and varies from one location to another. Often these crystalline bands will not be found.

2.4 Corrosion Resistance of Metallic Glasses

Overall, the corrosion resistances of metallic glasses are very good [19,20,55]. Grain boundaries and second-phase precipitates are not present in metallic glasses. The material is purely homogenous. This feature drastically reduces the effects of preferential or localized corrosion. However, the process of corrosion is still electrochemical. Therefore, the chemical composition is still a dominating characteristic affecting the corrosion resistance of the material. The ability of the alloy to form a stable passive film is the paramount objective. Historically, binary amorphous metal-metal alloys have had better corrosion resistance than their crystalline counterparts [20]. Figure A-14 summarizes corrosion penetration rates (CPR) for a fifty atomic percent copper and fifty atomic percent zirconium amorphous alloy compared with its crystalline state [56]. Except for where this alloy is very corrosion resistant, the amorphous state proves to have much lower corrosion rates. However, the corrosion resistance of a metallic glass never excels that of the nobler of the two elements. Therefore, the addition of the passive metal is in fact creating a more passive film. The crystallization of the binary system allows for

phases with increased atomic percentages of the poor corrosion resistant element, and possible galvanic conditions.

2.4.1 Corrosion Behavior of a Zr-Based Bulk Metallic Glass

BMGs have proven to follow the same general rule as above; however, with larger sizes, a better understanding of corrosion mechanisms can hopefully be ascertained. Many of the BMG's are zirconium-based. Titanium-based bulk metallic glasses are presently of intense interest. Zirconium and titanium are very similar. They form a very good passive film in water and salt-water solutions [57]. However, zirconium when coupled with copper is susceptible to localized corrosion in salt-water solutions. Limited corrosion studies of BMGs have been conducted due to the relative novelty of the field.

Schroeder, Gilbert, and Ritchie conducted corrosion tests on a zirconium-based metallic glass, $Zr_{41.2}Ti_{13.8}Cu_{12.5}Ni_{10}Be_{22.5}$, in 0.5M NaCl (approximately equivalent to seawater), and compared the results with the same test performed on its crystalline form [58]. The amorphous samples proved to be slightly more corrosion resistant than the crystalline samples, but the results were very similar. Both forms underwent localized corrosion. Localized corrosion is contrary to previous results conducted on thin ribbon metallic glasses.

2.4.2 Author's Studies of Cyclic Polarization Curves in 0.6 M NaCl

The electrolyte used in the investigation performed by Peter et al. [55] was 0.6 M NaCl in distilled water, which simulated seawater [61] similar to the above experiment conducted by Schroeder et al. [58]. Bulk Metallic Glass 11, BMG-11, was the Zr-based metallic glass used in Peter et al.'s experiments. Developed at California Institute of

Technology, Pasadena, California, the atomic composition is $Zr_{52.5}Al_{10}Ti_5Cu_{17.9}Ni_{14.6}$ [16,59,60]. This metallic glass was chosen because of its ease of forming an amorphous structure, its chemical composition, its potential use in biomedical applications, and the established dependability of its fabrication at ORNL over the last several years. Amorphous and crystalline annealed samples were tested

Drop-cast round-bar ingots of BMG-11 6.4 mm in diameter were fabricated at ORNL [61]. The ingots were cut to a reasonable length for corrosion and/or metallography samples (~10 mm) using an electrical discharge machine (EDM). The EDM created localized high temperatures in the material, but any crystallization was extremely localized and removed by grinding.

Amorphous samples to be crystallized for metallography or corrosion testing were placed in a vacuum furnace [61]. The furnace was preheated to 600 °C. The entire glass tube that was the chamber was evacuated to 10^{-6} torr by use of a mechanical and turbo pump in succession. The samples were in the glass tube during the vacuum process, but were not placed into the furnace until an adequate vacuum was achieved. The samples remained in the furnace for 5 hours and then were removed.

Metallography samples of both annealed and as-cast samples, 6.4 mm in diameter by ~1.6 to 3.2 mm in thickness, of the amorphous alloy were placed in resin, cured, and polished to a 0.5 μ m finish. These samples were etched with a nitric-hydrofluoric acid solution and observed with optical microscopy for crystalline regions. Figure A-15 is the micrograph of an as-cast amorphous sample of BAM-11, and figure A-16 is the micrograph of an annealed crystalline sample of BAM-11. Crystals were evident in the annealed sample. X-ray diffraction analyses were conducted on other samples using a

Philips X'pert X-Ray Diffractometer to characterize the structure. Figure A-17 is the x-ray diffraction pattern of the crystalline and amorphous materials [61]. Figure A-18 illustrates some of the variation in crystallization from sample to sample with the same heating treatment. Differences in the pattern may occur from the quality of the glass of the as-cast specimen.

Corrosion samples were drilled and hand-tapped approximately 2 mm into the specimen. A brass screw was placed into the sample. They were then placed in a mold with resin and cured. Amorphous and crystalline BMG-11 samples were tested with two surface conditions: (1) metallographically polished to a 0.5 μm diamond-paste finish, and (2) ground to a 600-grit SiC finish, which simulated an industrial finish. The samples were first ground with descending grit-sized papers to ensure the elimination of large scratches, defects, and/or pits. The samples' final grinding was usually conducted with a 600-grit paper (ANSI/CAMI). For those samples that were tested with a 600-grit finish, no further surface treatment was required, and the cyclic polarization test was conducted within a couple of hours. Those samples to be polished were then placed in weighted molds. The molds were subsequently positioned on a polymer head, vibratory polishing bowl with a 0.3 micron-alumina slurry. The sample was left for two to three hours on the bowl. They were then placed in another bowl with a 0.5 micron diamond paste for one to two hours. Testing was conducted immediately after removal from the polishing bowl.

A nonconductive epoxy was placed along the metal-resin interface prior to being tested. The exposed surface area of the metallic glass sample was measured. The electrolyte was measured and poured into a two-liter beaker. A saturated calomel reference electrode was first checked and then inserted into the electrochemical cell. The

brass screw of the metallic glass sample holder was attached to the working electrode via a j-tube. A plastic washer ensured that there was no electrolyte-brass interface. The counter electrode was attached to a small rectangular sheet of platinum, a very noble metal. The electrodes were attached to the potentiostat. The three electrodes were then placed into the electrolyte and held in place with the working and counter electrode surfaces close to each other, but not touching.

Electrochemical cyclic-anodic-polarization tests were conducted on the BMG-11 amorphous and crystalline samples using an EG&G Princeton Applied Research Model 263A Potentiostat/Galvanostat with EG&G 352 SoftCorr III computer software. Before each polarization scan was initiated, the corrosion sample was allowed to stabilize in the electrolyte for either one hour or until the corrosion potential, E_{corr} , changed by no more than 2 mV over a five-minute time period. The scan was started at 50 mV below E_{corr} and continued in the positive direction until an anodic current density of 10^4 mA/m² was reached. At this point, the scan direction was reversed, and the scan was continued in the negative direction until the original potential was reached. The potential scan rate was 0.17 mV/s.

In analyzing the cyclic-anodic-polarization behavior, a number of corrosion-related parameters were evaluated. These parameters are identified in the schematic polarization curves of Figure A-19, which illustrate typical behavior with regard to localized corrosion susceptibilities [61]. The plots are potential (relative to the SCE reference electrode) versus the logarithm of the external-circuit current density, where the current density is the measured external-circuit current divided by the specimen area. The controlled specimen potential can be regarded as the "driving force" for corrosion,

and the anodic current density is directly related to the specimen corrosion rate [86]. The potential scan is started below the corrosion potential, E_{corr} . At E_{corr} , the current density goes to zero, and then increases to a low and approximately constant anodic value ($\sim 10 \text{ mA/m}^2$ in Figure A-19) in the passive range. In this range, a thin oxide/hydroxide film, a passive film, protects the material from high corrosion rates [86]. If the current density decreases when the potential scan direction is reversed, as in path 1, the material is shown to be immune to localized corrosion. However, if on the potential up scan, the current density suddenly increases, and remains high on the down scan, until finally decreasing to the passive-region value, as in path 2, the material is shown to undergo a form of localized corrosion (pitting corrosion in this case). The potential at which the current density suddenly increases (pit initiation) is known as the pitting potential, E_{pit} , and the potential at which the current density returns to the passive value is defined as the repassivation potential or the protection potential, E_{pp} [86]. Between E_{pit} and E_{pp} , pits are both initiating and propagating. In the case of path 2, pits will not initiate at E_{corr} , the natural corrosion potential. Therefore, the material will not undergo pitting corrosion under natural corrosion conditions. If, on the other hand, path 3 is exhibited, where E_{pp} is below E_{corr} , the material will undergo pitting corrosion at surface flaws or after incubation time periods. In terms of overall resistance to pitting corrosion, two parameters are important, $[E_{\text{pit}} - E_{\text{corr}}]$ and $[E_{\text{pp}} - E_{\text{corr}}]$. Higher values of both are desirable to reflect high values of E_{pit} and E_{pp} , relative to E_{corr} .

The corrosion rate under natural corrosion conditions, i.e., at E_{corr} , is related to the corrosion current density, i_{corr} , which must be determined by extrapolative procedures or one of several analytical methods. In this study, the polarization-resistance method was

used to evaluate i_{corr} [86]. The corrosion penetration rate (CPR, $\mu\text{m}/\text{year}$) was calculated by the application of Faraday's law:

$$\text{CPR} = 0.327 (Mi_{\text{corr}})/\rho p \quad (2-1)$$

where M (g/mol), m , and ρ (g/cm^3) are the atom-fraction-weighted values of atomic weight, ion valence, and density for the alloy elements, and i_{corr} (mA/m^2) is the corrosion current density.

Table A-1 contains all of the critical corrosion parameters for the cyclic polarization curves performed on amorphous and crystalline BMG-11 samples in the 0.6 M NaCl electrolyte [61]. The average cyclic-anodic-polarization curves for the amorphous and crystalline BMG-11, with 600-grit surface finishes, in the 0.6 M NaCl solution, are shown in Figure A-20. Three to four replicate tests were run for each condition, with the specimens being taken from different ingots, so that both experimental error and material variability could be evaluated. Both the amorphous and crystalline materials were in the passive state at the natural corrosion potentials, E_{corr} [61]. The corrosion current densities (i_{corr}) and corrosion penetration rates (CPRs) were evaluated to be $1.2 \pm 0.6 \text{ mA}/\text{m}^2$ and $1.3 \pm 0.7 \mu\text{m}/\text{year}$, respectively, for the amorphous material, and $0.5 \pm 0.3 \text{ mA}/\text{m}^2$ and $0.6 \pm 0.3 \mu\text{m}/\text{year}$, respectively, for the crystalline material. These corrosion rates are extremely low and reflective of the passive state. Therefore, the concerns for these materials are their resistances to the onset of pitting corrosion.

The statistical analyses of the various electrochemical parameters are presented in Figure A-21, where the error bars represent \pm one standard deviation [61]. It is seen that

no statistical differences were observed between the amorphous and crystalline materials for the corrosion potentials (E_{corr}), pitting potentials (E_{pit}), or $[E_{\text{pit}} - E_{\text{corr}}]$. However, the differences in protection potentials (E_{pp}) and $[E_{\text{pp}} - E_{\text{corr}}]$ were statistically significant, with the amorphous material having higher values in both cases. In accordance with prior discussion, the latter result indicates that the amorphous material is more resistant to the onset of pitting corrosion under natural corrosion conditions.

The average cyclic-anodic-polarization curves for the amorphous and crystalline BMG-11 specimens in the metallographically-polished condition, in the 0.6 M NaCl solution, are shown in Figure A-22 [61]. Again, both the amorphous and crystalline materials were in the passive state at the natural corrosion potentials, E_{corr} [61]. The corrosion current densities (i_{corr}) and corrosion penetration rates (CPRs) were evaluated to be $8 \pm 13 \text{ mA/m}^2$ and $9 \pm 15 \text{ }\mu\text{m/year}$, respectively, for the amorphous material, and $14 \pm 13 \text{ mA/m}^2$ and $15 \pm 14 \text{ }\mu\text{m/year}$, respectively, for the crystalline material [61]. Although these corrosion rates are approximately 10 times higher than evaluated for the rougher 600-grit surface finish, they are still quite low and representative of the passive state. A possible reason for the higher corrosion rates observed for the smoother, polished surface condition (an unusual situation) relates to the time interval between the last surface-finish operation and the immersion of the specimen in the electrolyte. For the polished condition, the time interval was less than five minutes, whereas for the 600-grit condition, it was on the order of one hour. Therefore, for the polished specimens, less time was available for the formation and thickening of air-formed oxides, and this effect could have resulted in higher corrosion rates.

The statistical analyses of the electrochemical parameters for the specimens in the polished condition are given in Figure A-23 [61]. It is seen that no statistical differences were observed between the amorphous and crystalline materials for the corrosion potentials (E_{corr}) or [$E_{\text{pit}} - E_{\text{corr}}$]. However, the differences in pitting potentials (E_{pit}), protection potentials (E_{pp}) and [$E_{\text{pp}} - E_{\text{corr}}$] were statistically significant, with the amorphous material having higher values in all three cases. Again, this latter result indicates that the amorphous material is more resistant to the onset of pitting corrosion under natural corrosion conditions in the 0.6 M NaCl solution, relative to the crystalline material.

Several corrosion samples after being tested in 0.6 M NaCl were examined by SEM. Both crystalline and amorphous samples underwent localized or pitting corrosion. The surface characteristics were slightly different. Crystalline samples contained pits that were regular in shape and evenly distributed. Amorphous samples contained pits that were large, irregular shaped and more sporadically distributed.

An amorphous sample was examined using the capabilities of the SEM [61]. Figure A-24 is an SE image of the overall sample surface. From examining most of the surface, no difference in chemical composition was noted. However, one area contained a defect. Figures A-25 and A-26 are SE and BSE images, respectively, of this area. These defects were most likely near-surface porosity since irregular round shapes were **visible** in both images. Possible reasoning for the location of pits and their initiation were not determined.

Several images of a crystalline sample after corrosion testing were also taken with the SEM [61]. Figures A-27 and A-28 are the SE and BSE images, respectively, of a pit.

An EDS Spectrum was taken of this area, and then analyzed for chemical composition. A slight increase in copper, two to four percent difference, was found. The fact there was a large contrast in appearance between the SE and BSE images suggested that a copper-rich precipitate was in the area of the pit initiation. However, a more accurate method of acquiring chemical compositions is required for verification.

2.5 Mechanical Behavior

The mechanical behavior of BMGs is of great interest because of their incredible strengths and very low Young's moduli. Most zirconium-based bulk metallic glasses have a tensile strength between 1,500 to 2,000 MPa and a Young's modulus of around 90 GPa [2,16]. These values are quite exceptional compared to many high strength steels (i.e., 4340 steel, aircraft quality, with a tensile strength of 1,634 MPa and a Young's modulus of 207 GPa) [62]. Not only is the strength greater for the amorphous phase compared to the crystalline phase, but also fracture toughness values are greatly increased, and fatigue lifetimes are enhanced [1,2]. By understanding the mechanics of an amorphous phase, an overall better understanding of the effects of atomic ordering can be achieved, and steps can be made in maximizing the mechanical benefits of metallic glasses. This is an important area of study since fracture mechanisms involved with amorphous metals are poorly understood compared to their crystalline counterparts.

In sections 2.2.3 to 2.2.5, the author explained topological and chemical ordering on an atomic scale. Local ordering, increased free volume, and diffusion may have enough occurrences along a given orientation to allow for preferred or localized fracture to occur. Inhomogeneities on a atomic scale allow for deformation to occur in an amorphous alloy. First, the author will review monotonic fracture. Fracture morphology

will be compared with the possible mechanisms occurring. After discussing monotonic fracture, fatigue or cyclic loading will be discussed. Finally, we will review the effects of environment.

2.5.1 Monotonic Fracture

BMGs deform in one of two fashions: homogenous or heterogeneous deformation [35,63,64]. Nieh et al. performed tests on Zr-base and La-base BMGs at different temperatures and at different load or strain rates [64]. In the supercooled liquid region (SCL), the temperature range between the crystallization temperature, T_X , and the glass transition temperature, T_G , a Zr-based BMG exemplified homogenous deformation while still a glass [64,65,66,67]. Nieh reported this occurs to almost 70 % of the T_g temperature. In this temperature region, the glass deforms with significant plasticity (Nieh et al. reported elongation up to 600%) and is found to be ductile similar to traditional oxide glasses in the SCL [64]. The BMG behaves in a Newtonian or a non-Newtonian manner, depending on the strain rate and the temperature. The lower the temperature and the higher the strain rate the higher possibility of non-Newtonian flow. The term Newtonian flow is usually used in relation to the viscosity of fluids when a shear load is applied. In a Newtonian fluid, the fluid will experience a shear stress proportional to the strain rate. Nieh et al. conducted tensile tests at 683 K (within the SCL) on sheet specimens from as-cast material [64]. At low strain rates, the behavior was Newtonian. At high strain rates the behavior was non-Newtonian. At high strain rates (samples exhibiting non-Newtonian behavior), TEM images reveal an amorphous matrix with nano-sized crystallites of Zr_2Ni and Zr_2Cu and local lattice fringes. The nano-sized crystallites were directly related to the deviation from Newtonian behavior.

Heterogeneous deformation of BMG specimens tested at temperatures well below the glass transition temperature (e.g., room temperature) has been reported since the 1970s [63,68,69,70]. Similar to crystalline metals, BMGs deform in an elastic manner up to the yield strength. For the most part, BMGs can be identified as isotropic. However, this is not always the case. Residual stresses can be induced into the alloy from directional heterogeneous solidification in the casting or ribbon forming process [71]. The compressive residual stresses are most prevalent in the extreme outer layer.

For the present essay, the heterogeneous deformation is most important. The homogenous deformation at higher temperatures or lower strain rates illustrates the change in fracture mechanisms as more energy is administered into the system, and more time is provided for equilibrium. Heterogeneous deformation occurs in localized shear bands or serrations. Typically, these shear bands are in the order of 20 to 40 nm [35]. A large amount of plastic strain occurs at these localized regions (~ 10 % or more) [35]. However, the plastic deformation of the entire specimen is usually quite low (~ 2 to 3 %) [16]. The overall low plastic strain illustrates the localized nature of the deformation.

There are two schools of thought as to how shear bands are formed in BMGs [72]. The first thought is that viscosity in shear bands decreases due to increases in the free volume in this region. There are three known processes that can change the free volume in a local area: diffusion, annihilation, and stress-driven creation [73]. In loaded samples, stress-driven creation is most strongly emphasized. Spaepen best illustrates this effect in a cartoon, figure A-29, from a paper he published in 1977 [63]. This paper is one of the most highly referenced papers regarding the creation of free volume in metallic glasses. As a shear load is applied, atomic bonds are stretched, and a hard sphere atom is

squeezed into a neighboring hole in which it once would not fit [63]. This leaves an even larger gap with a lower density in the local area. Relaxation is competing against this effect, but as the load is increased the increase in free volume becomes more favorable. As this continues, the viscosity in this region decreases, the material locally softens, and the cross section of the specimen is lowered. Finally, the material softens to the point that the material fractures. The deformation is termed as almost perfectly plastic from the drastic softening of the localized material, and the mechanism of fracture is termed Taylor instability [1,2,3,4,5]. A “vein” pattern or a branching river structure is observed on the fracture surface. This is the structure left from the softening of the material.

The second of the two hypothesis is that stored energy from elastic deformation is converted to local adiabatic heating as the load on the specimen increases. At a certain load, the local heat exceeds the glass transition temperature, or even possibly the melting temperature, and the viscosity decreases by several orders of magnitude, softening the material. Temperatures can be calculated in excess of the melting temperature for many of these BMGs if all elastic energy went into adiabatic heat at a localized plane. IR thermography has shown high temperature increases [74,72] at fracture. However, some of these tests were conducted with high strain rates and the temperature evolution was not observed before fracture. Other tests, conducted by Flores et al. using an IR camera to observe the temperature changes in Mode I and Mode II fracture tests, found the temperatures to not be adequate for softening, but they could reduce the viscosity [75]. Nevertheless, crystallization has been observed on the fracture surface in droplets associated with the vein morphology.

It is most likely that the former hypothesis is correct. However, the role of adiabatic heat on the fracture surface after overload is not well known. It is the author's opinion that increases in free volume soften the material. After the material fractures, the elastic energy that is not translated into plastic energy is transformed into adiabatic heat. The heat and the softened surface, from change in free volume, help together to form the vein like patterns with some localized crystallinity. The hypothesis of lowering viscosity by increasing free volume is supported by three individual findings. Li et al. used high resolution TEM on tensile specimens of a Zr-based BMG ($Zr_{57}Ti_5Cu_{20}Ni_8Al_{10}$) after loading, and found significant increases of free volume in shear bands than in areas outside the shear bands [76,77]. Figure A-30 is a HRTEM image they took of a shear band. The lighter areas reveal high concentrations of voids that were left behind in shear bands with a diameter of one nanometer. The reader should note that this diameter is after failure (unloading), and would be after free volume coalesced into voids. These voids were only located in the shear bands, and not in the bulk of the specimen. Pampillo etched Pd-based metallic glass samples after plastic deformation [69]. The shear bands showed preferential etching. This indicates the chemical potential has changed, possibly by increases in free volume. Lastly, Kim et al. performed nanoindentations on Zr-based BMG samples [78]. The nanoindentation produced deformation in the form of shear bands. Crystallization was observed near these shear bands. Since nanoindentation is loading with an ultra-fine scale point of contact, very little adiabatic heat is produced. Therefore, crystallization can occur with high stress levels and does not require glass transition temperatures. The above studies strongly suggest the softening mechanism in metallic glasses is from increases in free volume.

2.5.2 Monotonic Fracture Morphologies

A recent study by Ritchie et al. describes the morphology of a Zr-based bulk amorphous alloy via scanning electron microscopy after undergoing monotonic, bending fracture [1]. Shear steps were visible along the length of the fracture surface. Figure A-31 is a good example of typical shear steps on the fracture surface, as viewed by SEM. A “vein” morphology typical of amorphous metals on the fracture surface was found at a microscopic level. This morphology is close in nature to what is observed during the “separation of grease or adhesive films” [1]. “Liquid droplets” were found along intersections of these vein patterns [1]. Figure A-32 illustrates both the vein patterns and liquid droplets (arrows), as typically found in BMGs. The liquid droplets are thought to be associated with the large release of heat upon tensile fracture.

Liu et al. describes both the tensile and compressive fracture properties and morphologies of a Zr-based bulk amorphous alloy [16]. These tests were conducted on 7 mm diameter drop cast ingots of $Zr_{52.5}Al_{10}Ti_5Cu_{17.9}Ni_{14.6}$ (at. %). Under tensile loads, the bulk amorphous alloy was found to have fracture strengths up to 1,750 MPa [16]. The fracture surface was at a 34-degree slant from the loading direction [16]. Shear steps were visible throughout the fracture surface. A two percent elastic strain was witnessed during testing, but no bulk plastic deformation was observed. A “vein” morphology typical of amorphous metals was found at a microscopic level at the fracture surface. This morphology is close in nature to what is observed during “separation of grease or adhesive films”, and is related to Taylor instability [1,2]. “Liquid droplets” were found at various intersections of these vein patterns [16]. Sparks and a loud popping sound were

heard at the time of fracture. Young's modulus was determined to be 89 GPa, which is very low [16].

Under compression testing, the fracture strength was found to be 1,870 MPa [16]. The fracture surface was at a 45-degree slant compared to the loading direction [16]. Shear steps and shear bands were visible throughout the fracture surface. An elastic strain of 2 percent, and a bulk plastic strain of 0.5% were observed [16]. The elastic limit in compression was found to be very close in value to the fracture strength in tension.

When the above compression and tension testing results are compared, conclusions can be drawn on the mechanisms at work. The metallic glass specimens exhibited shear bands and shear steps when failure occurred in both tension and compression [16]. Shear is by far the largest mechanism causing failure. The 55-degree surface in tension versus the 45-degree surface in compression is illustrative that normal stresses may play a significant role in the shear-band formation of metallic glasses. The above results illustrate the absence of general slip mechanisms that are a major contribution to the deformation of many crystalline metals. The absence of slip is understandable; there is no crystalline lattice to facilitate the continuous movement of dislocations. To further amplify this point, Figure A-33 illustrates tests conducted by Inoue in which samples containing varying amounts of nano-crystals in a metallic glass matrix, Zr-10Al-20Cu-10Pd, were loaded to failure in tension [11]. The resulting slope of the fracture surface illustrates the mechanism of failure for the individual samples. A completely amorphous alloy to around 40 volume percent crystallinity failed at or greater than a 45-degree angle compared to the loading direction. The slanted fracture surface reveals failure occurred in plane-stress or in shear type. The sample with 46 percent

nano-crystals by volume failed at a 90-degree angle illustrating fracture mechanisms caused mainly by plane-strain and/or normal stresses [11]. Obviously, by comparison, the larger the volume fraction of amorphous phases the higher degree of failure in shear.

As mentioned before, the Zr-based bulk metallic glass, $Zr_{52.5}Al_{10}Ti_5Cu_{17.9}Ni_{14.6}$, exhibited a high tensile fracture strength, 1,750 MPa [16]. The mechanical energy applied to the specimen during the tensile test is released as heat at the fracture surface. Metallic glasses have relatively low melting temperatures. The metallic glass stores the energy until the specimen fails. The black body temperature has been measured as high as 3,175K for some BMGs [79]. During fracture, the specimen actually underwent localized areas of melting along the shear bands [16]. These localized areas are the visible “liquid droplets”. At some of these droplets, the material is in its crystalline form. The sparks following fracture are another result of the heat release in the test specimen. The heat triggers rapid oxidation at the fracture surface causing a popping sound and sparks.

In review, monotonic fracture theory and modeling are well in tune with the morphology observed on the fracture surface. Even the areas that are not as well known (e.g., adiabatic heating effects) have been researched, and better understood. The predominant theme the author wants the reader to take from the last two sections is that fracture is heterogeneous with localized areas of plastic deformation, or shear bands that undergo an increase in free volume, and therefore experience softening to the point of fracture.

2.5.3 Environmental Effects on Tensile Fracture

The recent work by Liu et al. also studied how various testing environments affected the magnitude of the tensile strength [16]. BAA-11, $Zr_{52.5}Al_{10}Ti_5Cu_{17.9}Ni_{14.6}$ (at. %), samples were tested at room temperature in air, water, vacuum, and dry oxygen. Zr, Al, and Ti are all highly susceptible to hydrogen embrittlement. Hydrogen embrittlement involves absorption of hydrogen into the material at locations where hydrogen gas is evolved through a cathodic reaction. The various environments were used to investigate the degree of susceptibility of the amorphous alloy to hydrogen embrittlement and/or stress corrosion.

Tensile strengths and elastic properties were similar for all four environments [16]. This result shows that either this zirconium-based metallic glass is not susceptible to hydrogen embrittlement during tensile testing or that other mechanisms are masking the hydrogen effects. Vacuum-annealed samples were submerged in distilled water, H_2O , and heavy water, D_2O , for three days. Results from a laser desorption mass spectrometer readings indicated absorption of atomic hydrogen and deuterium (D, an isotope of hydrogen), respectively. “These results provide direct evidence that BAA-11 reacts with moisture and generates atomic hydrogen in the material” [16]. Other mechanisms must be masking any hydrogen embrittlement. Suh et al has also cited that hydrogen can also retard crack propagation by hydrogen atoms occupying the large free volume spaces that would contribute to decreasing viscosity [80,81]. Therefore, hydrogen would have one of two effects: embrittlement or decreasing the free volume.

2.5.4 Fracture Toughness

Ritchie, Schroeder, and Gilbert studied monotonic fracture toughness values of a bulk amorphous metal and its crystalline form [1,2,5]. These tests were conducted on 3 or 7-mm thick compact test specimens (C(T)) of $Zr_{41.2}Ti_{13.8}Cu_{12.5}Ni_{10}Be_{22.5}$. Samples were tested either as amorphous, 5 volume percent nano-crystalline, or completely crystalline. The 5 volume percent nano-crystalline samples were achieved by heat treating the samples for twelve hours at 633 K, and the completely crystalline samples were heat treated for twenty-four hours at 723 K.

Figure A-34 illustrates the relationship between the fracture toughness and annealing time. The completely amorphous samples had an average fracture toughness of approximately $58 \text{ MPa}\sqrt{\text{m}}$ [1,2,5]. Both the partially-crystallized and fully-crystallized samples had fracture toughness values of approximately $1 \text{ MPa}\sqrt{\text{m}}$. These two types of samples were so brittle that when the sample was being pre-cracked, the force resulted in catastrophic failure. The partially-crystallized and fully-crystallized samples were then tested by Vickers hardness tests, and converted to fracture toughness. There is a 5,700% difference between the amorphous and crystallized alloys.

Figure A-35 is SEM images of the fracture surfaces. The photomicrograph on the left is the fracture surface of the amorphous material, and that on the right is the fracture surface of the partially crystallized material at the same magnification. Notice that though metallic glasses do not illustrate plastic strain at a macroscopic level, there is plastic deformation on a microscopic level of the fracture surface [1,2,5]. The fracture surface of the partially crystallized alloy is fairly featureless and looks much more like localized brittle fracture.

The incredible fall-off rate of fracture toughness with respect to the annealing time that was found in this experiment is not typical of all metallic glasses. Some metallic glasses exhibit a small increase in fracture strength and toughness with volume fraction percents between 5 and 30 percent nano-crystallization [11]. However, the toughness goes drastically down when samples with over 30 percent nano-crystallization are tested.

2.5.5 Cyclic Fatigue and Fracture

In sharp contrast to monotonic fracture, very little literature is available on the fracture mechanics involving cyclic loading of BMG samples. Even less literature exists on the atomic modeling and theory of crack propagation. Most of the fatigue work on metallic glasses has been done in the last seven years [1,2,3,4,5,6,7,8,9,10]. Prior to BMGs, metallic glasses were too small to do any practical fatigue testing. More interest has recently emerged since application is possible. With the new found interest in fatigue testing of BMGs, modeling and documented fatigue mechanisms should be short to follow. However, only foundation work has currently been laid down for understanding fatigue fracture mechanics.

In the 70s, Lance Davis came up with a notion that the lack of bulk plastic deformation in metallic glasses indicated the possibility for a perfect amorphous alloy, without constraint, to exhibit a fatigue endurance limit that approaches the ultimate tensile strength [82]. This idealistic hypothesis has not been realized largely due to a “perfect” amorphous alloy being impossible to fabricate (i.e., no short range order, no diffusion, no porosity, no crystallization, etc). Metallic glass fatigue samples have undergone six hundred loading cycles at 99% of the fracture strength with an R ratio of 0

in tension [25]. This phenomenon is interesting compared to high-strength alloys that can only sustain a few cycles at stress magnitudes approaching the ultimate tensile strength. However, the results of some fatigue testing on a $Zr_{41.2}Ti_{13.8}Cu_{12.5}Ni_{10}Be_{22.5}$ BMG have been quite different. In fact, certain fatigue studies have shown the fatigue endurance limit for this BMG to be six to eight percent of the tensile strength [1,2,3,4,5]. Based on the above ideal belief, six to eight percent is an extremely low value. Since these low results, Peter et al. [6,7] and Wang et al. [8,9,10] have both found much higher fatigue endurance limits (around 50% of the tensile strength). Obviously, variability is an important issue in the study of fatigue behavior of BMGs.

Gilbert, Schroeder, and Ritchie present data for cyclic fatigue crack propagation rate tests and stress-life measurements of a $Zr_{41.2}Ti_{13.8}Cu_{12.5}Ni_{10}Be_{22.5}$ BMG, and compare the results to high-strength polycrystalline materials, 300-M ultrahigh strength steel, and 2090-T81 aluminum-lithium alloy [1,2]. The cyclic fatigue crack propagation rate tests were conducted on 7-mm thick C (T) specimens. The stress-life measurements were performed on 3 x 3 x 50-mm rectangular beams.

A comparison of metallic glass to high strength polycrystalline metals allows for a clear understanding of the fracture mechanics involved with metallic glasses and how they relate to crystalline materials. Cyclic fatigue crack propagation rate tests were conducted at a frequency of 25 Hz, and a load ratio (R), minimum load divided by maximum load, of 0.1 to 0.5 [1,2]. The results are shown in Figure A-36. Fatigue threshold stress intensity factor ranges were determined by decreasing the stress intensity factor range to a point where crack growth rates were below 10^{-10} m/cycle. The resulting fatigue threshold stress intensity factor ranges for the steel, the aluminum, and the

amorphous metal were 7 MPa√m, 2 MPa√m, and 3 MPa√m, respectively [1,2]. These values are very similar. The amorphous alloy maintained a stable fatigue crack that illustrated a crack advancing mechanism of blunting and resharping. This is the identical type of advancing mechanism that is found in both the steel and aluminum [1,2]. Similar crack growth rates at applied stress intensity factor ranges were found in all three samples; in fact, the amorphous alloy's crack growth rates are just slightly below the other two alloys. The metallic glass did exhibit some scatter in the crack growth data; this is attributed to compressive residual stresses in the outer layers. Overall, the amorphous alloy demonstrated many of the same fatigue crack characteristics of the high strength steel and aluminum. The results of a cyclic fatigue test conducted on the crystallized alloy were also indicated in the literature [2]. Data followed a vertical trend with large increases in crack growth rate with negligible increases in the stress intensity range. Cracking was very unstable in the crystallized alloy, and catastrophic failure occurred immediately after loading [1,2]. This type of result illustrates the brittleness of the crystallized version.

The fatigue stress-life (S-N) behavior of metallic glass showed very different results than the fatigue crack growth test [1,2]. Figure A-37 illustrates the results of this test. The test was conducted by four-point bending in air. The frequency was held at 25 Hz, and the load ratio was 0.1. Fatigue lifetimes were much shorter than the high strength polycrystalline alloys. Fatigue limits could not be detected until the stress amplitude was below 5% of the ultimate tensile strength [1,2]. Upon viewing the fracture surface with a SEM, extensive slip-band formation and slip steps were visible on the metallic glass.

Stress-life behavior and cyclic fatigue crack growth rate testing exhibited contradictory results [1,2]. In cyclic fatigue crack growth rate testing, the BMG was observed to have characteristics very close to those of high strength polycrystalline materials. In the stress-life behavior test, the BMG was inferior with respect to the high strength polycrystalline alloys. The above phenomenon can only be explained by crack initiation [1,2]. The cyclic fatigue crack propagation rate samples were C(T) specimens. These specimens are pre-cracked prior to conducting the test. The life-stress specimens are beams that are carefully checked for any initial cracks. The end result is that crack initiation in metallic glasses is much more sensitive to the applied stress than the crack initiation in either the steel or the aluminum.

The author also conducted fatigue tests on a Zr-based BMG (BMG-11) in air [6,7]. However, the air S-N fatigue results were drastically different from those observed by Ritchie et al [1,2,3,4,5,6,7]. Radial notched, round bar specimens were tested in uniaxial tension with a R ratio of 0.1. Figure A-38 is the fatigue specimen geometry, and the gripping system used. A stress concentration between 1.45 and 1.55 is associated with the notch. Samples were notched to avoid complications with porosity. The surface was finished to 5 μm .

The fatigue endurance limit (σ_L), based on the stress range, for the BMG-11 samples tested in air was approximately 907 MPa [6,7], as shown in figure A-39. The fatigue ratio (σ_L divided by the ultimate tensile strength) for the BMG-11 was 0.53, based on the ultimate tensile strength of 1,700 MPa. The average relative humidity for the tests performed in air was 45%, and ranged from 40 to 55 %. For BMG-11, the fatigue ratio, 0.53, was much higher than Ritchie et al.'s reported values of 0.06 to 0.08 [1,2,3,4,5,6,7].

When comparing BMG-11 with high-strength alloys and crystalline zirconium, figure A-39, the fatigue endurance limit of BMG-11 is comparable or higher than the other materials [6,7]. Also, the fatigue ratio for BMG-11, 0.53, is a relatively high value. Most alloy steels have a fatigue ratio between 0.35 and 0.60 [54,83]. BMG-11 is at the higher end of this range. Many high-strength steels with comparable ultimate tensile strengths have lower fatigue ratios.

Others have performed similar S-N fatigue tests on Zr-based BMGs and found similar results. Wang et al. performed tests on $Zr_{50}Al_{10}Cu_{40}$, $Zr_{50}Al_{10}Cu_{30}Ni_{10}$, and $Zr_{41.2}Ti_{13.8}Cu_{12.5}Ni_{10}Be_{22.5}$ with the same testing conditions as discussed for Peter et al.'s studies [8,9,10]. They found similar results to Peter et al. with fatigue endurance limits ranging from 615 to 1,000 MPa, and fatigue ratios between 0.3 and 0.45. Figure A-40 is an S-N plot containing Wang et al.'s, Peter et al.'s, and Gilbert et al.'s results [1,2,3,4,5,6,7,8,9,10]. One of Wang et al.'s studies found that varying the amount of oxygen present impacts the fatigue lifetime and fatigue-endurance limit of a Zr-based BMG [8]. Two fabrication batches of the $Zr_{41.2}Ti_{13.8}Cu_{12.5}Ni_{10}Be_{22.5}$ BMG were used for fatigue lifetime data. Batch 59 contained less oxygen than batch 94. Oxygen quantities were not provided. The fatigue lifetime and fatigue-endurance limit of the material with more oxygen were lower. Figure A-41 is an S-N plot of the results of the two batches. The fatigue-endurance limit showed a thirteen percent difference between the two batches. Oxygen can have a major impact on the fatigue behavior of bulk metallic glasses.

The other major conclusion of Wang et al.'s paper [8] is that the same chemical composition made at different times, by different processes, or by different people can

have a wide range of fatigue-endurance limits. The fatigue-endurance limit of Batch 59 was 703 MPa. This value is over a 350% increase compared to Ritchie et al.'s reported fatigue-endurance limit. Several conditions could have made the difference between Ritchie et al. and the results of Peter et al. and Wang et al.[1,2,3,4,5,6,7,8,9,10]. These conditions will be addressed in section 2.6, critical issues.

2.5.6 Fatigue Morphology

Ritchie et al. described the morphology of fatigue samples after overload fracture [1]. Two distinct morphologies were present. Close to the crack initiation site, the surface was observed to be smooth. Upon closer examinations, striations could be observed. Figure A-42 is a micrograph of this area. Several papers written by this group mention that these striations are analogous with individual cycles and are caused by the crack going through a sharpening and then blunting condition [1,2,3,4,5]. Unlike the fatigue area, the fracture overload surface was very rough [1]. Figure A-43 is a micrograph of this area. At higher magnification, this area had a "vein" morphology very similar to fracture surfaces of samples tested in tensile fracture. Figure A-44 is the division between these two morphologies, and the beginning of the overload fracture.

2.5.7 Environmental Effects on Fatigue

In the last few years, more experiments have focused on the effects that the environment has on the fracture and fatigue behavior of zirconium-based BMGs [1,2,5,6,7,80,81,84]. The current research involving the environment has not been a surprise since most metals are greatly influenced by corrosion and corrosion fatigue. In fact, in 1995, it was estimated that \$300 billion of the US economy was annually spent on the direct results of corrosion and corrosion fatigue [85]. This figure does not include

money spent on indirect results such as loss of wages, over-design costs, and loss of products. With so many components being influenced by corrosion and corrosion fatigue, a fundamental understanding of the influence of the environment on the failure of metallic glasses is important.

Ritchie et al. studied fatigue testing in air, de-ionized water, and 0.5 M NaCl [5]. By testing in these three environments, it can be seen whether corrosion fatigue and/or hydrogen embrittlement are detrimental to the fatigue life. Figure A-45 illustrates the results. The water produced only a slight detriment to the fatigue life compared to air. The sample in the 0.5 M NaCl solution was greatly affected by its environment. The curves are also very different in shape. The air and water curves follow a traditional Paris's Law. The crack growth rate for any stress intensity factor range value between 1.5 and 10 MPa√m for the sample tested in air can be modeled by the following equation and values:

$$da / dN = C \Delta K^m, \quad (2-2)$$

where da/dN = crack length rate, m/cycle

$$C = \sim 2.3 \times 10^{-10} \text{ MPa}\sqrt{\text{m}}$$

$$m = 1.6 \text{ m/cycle,}$$

and ΔK = stress intensity factor range MPa√m [5].

The results of the sample tested in air fit relatively well to the model. The sample tested in 0.5M NaCl did not follow this equation for the stress intensity factor ranges that are

shown. Obviously, some other mechanism is greatly increasing the crack growth rate. This phenomenon could be explained by corrosion, corrosion fatigue, or hydrogen embrittlement. Ritchie et al. also conducted tests in the 0.5 M NaCl electrolyte while applying an electrochemical potential to the specimen [5]. Figure A-46 illustrates the results. Potentials below -750 mV(SCE), supporting a highly cathodic reaction, would generate atomic hydrogen. In turn, this would have increased the acceptability of hydrogen embrittlement, had the sample been susceptible to it in this environment. Ritchie et al. started the test at -900 mV(SCE), and stepped the potential up after the crack growth rate stabilized for a period of time [5]. The crack growth rate increased as the potential increased, and then stabilized at -750 mV(SCE). This indicates that the large increases in crack growth rates may not be due to hydrogen embrittlement, but rather to an anodic reaction such as pitting corrosion [5].

The sample fracture surface morphologies were very different between the air, water, and 0.5M NaCl. The air and water had rough local crack growth steps close to final failure [5]. At threshold values, the surface was relatively smooth. In the 0.5 M NaCl solution, the fracture surface was smooth throughout the entire surface with very large steps and micro cracking. The 0.5M NaCl sample failed due to corrosion and stress corrosion cracking. The air and water samples failed largely by fatigue mechanisms.

2.6 Critical Issues

It is the author's hypothesis that it is impossible to create a perfect amorphous alloy with current techniques, because any fabrication process, including casting or ribbon forming, is not perfect. There will always be directional solidification, minute amounts of impurities, interfaces with solids, machining flaws, and other complications.

Bulk metallic glasses are metastable phases. New compositions are good glass formers, but little changes in fabrication can easily cause them to precipitate into a crystalline phase, even if the crystallization is only localized. Therefore, it is difficult to perceive a BMG as a “perfectly” homogenous material. However, treating BMGs as idealized homogenous materials with localized areas, or pockets, of impurities will probably be sufficient in assessing the fatigue behavior of BMGs.

The author suggests that it is the casting characteristics discussed in section 2.3.6 that cause an otherwise homogenous material to have preferable locations for failure, and variability in fatigue results as discussed in section 2.5.5. In sections 2.2.3 to 2.2.5, the imperfections that could cause heterogeneity on atomic level were discussed. These are the inherent characteristics that make an amorphous alloy. Separating the micro- and macro-scale flaws from the intrinsic atomic scale chemical and topological structures is important in understanding the true mechanical behavior of BMGs. Crystallinity, porosity, machining marks, and unmixed elements can all act as stress concentrators, depending on the placement in a structural component. These fabrication flaws can decrease the local strength of the BMG. These imperfections may play significant roles in low fatigue-endurance limits. They can also serve as specific locations for environmental assisted degradation such as corrosion, hydrogen/oxygen embrittlement, stress corrosion cracking, and corrosion assisted fatigue. The effect of the flaws is important for industrial applications. Large batch alloys fabricated in commercial settings are not often as well quality-controlled as small batches fabricated in academic environments. Therefore, “real” parts will contain imperfections, and fatigue behavior based on this quality of material is important. However, knowledge of the fatigue

behavior of high quality BMG components is academically important for determining possible applications. If the main factors causing degradation are recognized, there is a possibility to lower these impurities and improve the mechanical characteristics.

The present time is an exciting time to experiment with metallic glasses. A large amount of foundation work has been laid out, but an understanding of the key mechanisms that cause corrosion, corrosion fatigue, and fatigue in metallic glasses are not well understood. In the following section, studies were carefully arranged to better recognize the mechanisms with the most detrimental effects. By discovering these mechanisms and correcting for them, BMG samples may have much higher fatigue limits.

CHAPTER 3: EXPERIMENTAL PROCEDURES

The primary goal of this dissertation was to resolve undecided issues regarding the fatigue properties of a Zr-based BMG. Careful attention was provided to predetermining the experiments conducted to acquire particular information. Each experiment resulted in certain aspects of the material that when combined together helped to better identify the materials behavior. Fabrication, microscopy, corrosion, and fatigue were some of the procedures performed in order to conduct this research.

3.1 General Overview of Experiments Conducted

Test results can be greatly influenced by the homogeneity and perfection of the amorphous material. Metallic glasses are complex and are not found naturally. They are a meta-stable phase. Over given amount of time, they would diffuse into their stable crystalline state. However, the time span required for most present day compositions would be much longer than the in-service lifetime of a structural component. Therefore, there is very little concern for room temperature conditions. However, elevated temperatures, such as during the casting process, could tremendously speed up crystallization. This places specific importance in the fabrication process of amorphous alloys. The author fabricated his own BMG at ORNL. Most possible complications in forming an amorphous material were apparent and avoided by having conducted the entire fabrication process in a controlled manner by the author. Time and careful attention were provided to fabrication.

Defect free, amorphous samples were the main objectives in sample preparation. Samples were observed with optical microscopy (OM) to ensure an amorphous phase.

Careful etching and polishing techniques were used to identify any crystalline regions present. X-ray diffraction patterns were used to verify the absence of long-range order in the amorphous materials and the presence of long-range order in the crystalline materials. Samples for fatigue testing were radiographed to detect porosity and/or small masses of unmixed pure elements. Corrosion samples were carefully polished to ensure that no scratches or defects were present on the surface of the sample. Any irregularities in the surface geometry could have affected results.

Corrosion studies were performed in water containing a small concentration of Na_2SO_4 . Pitting potentials, corrosion potentials, corrosion current densities, passive current densities, protection potentials, and active current densities were several of the parameters that were obtained by polarization curves [86]. These results indicated the corrosion resistance of the BMG in the designated electrolyte. Several characteristics of importance were whether the sample was passive or active at its natural corrosion potential, whether the sample underwent localized corrosion, and if the pitting potential was relatively close in magnitude to the corrosion potential. Testing the sample in water (plus Na_2SO_4) helped to indicate if the metallic glass was susceptible to corrosion in water, or even humidity. The shape of the polarization curves was important in indicating the natural tendencies of the material in the electrolyte.

Fatigue tests were conducted in air and compared with fatigue experiments performed in vacuum to observe any detrimental effects that the humidity in air had on the degradation of the metallic glass. The tests were designed to identify the possibility of corrosion, corrosion fatigue, and/or hydrogen embrittlement due to water vapor. Stress-life curves were recorded and compared for tests conducted in air and in vacuum.

These curves illustrated whether or not humidity had an effect on fatigue lifetimes, and the degree of influence. Some fracture surfaces were studied in the SEM. By understanding the morphology of the fatigue fracture surface, the mechanisms that caused failure can be more readily identified. Four-point bend studies were conducted in air and compared with the results of those tested in uniaxial loading to determine any differences in loading conditions. Samples charged with hydrogen and cyclically loaded in air were used to observe the detrimental effects of hydrogen embrittlement on the fatigue lifetime of BMGs. Studies of test specimens with different geometries and various surface finishes were performed to understand the effect of testing volume/surface area and average external defect size, respectfully, on the fatigue lifetime and fatigue-endurance limit. Lastly, samples with increased amounts of crystallinity were tested in three-point and four-point bending to analyze its effect on the overall fatigue behavior.

3.2 Sample Preparation and Material

Bulk Metallic Glass 11, BMG-11, was the Zr-based metallic glass used in these experiments. Developed at California Institute of Technology, Pasadena, California, the atomic composition is $Zr_{52.5}Al_{10}Ti_5Cu_{17.9}Ni_{14.6}$ [16,87,88]. This metallic glass was chosen because of its ease of forming an amorphous structure, its chemical composition, its potential use in biomedical applications, and the established dependability of its fabrication at ORNL over the last several years.

Drop-cast round-bar ingots of BMG-11 were fabricated at ORNL and the University of Tennessee. The samples were manufactured by arc melting in an inert gas environment. A total of eighteen grams of the various elements were mixed in a copper crucible. Table A-2 lists the weights of the metals used. Pure zirconium turnings (99.5

wt. % Zr), copper (99.99 wt. % Cu), nickel (99.99 wt. % Ni), titanium (< 550 ppm oxygen, < 110 ppm carbon), and aluminum (99.99 wt. % Al) were placed in the crucible after being weighed. Pure zirconium turnings were placed on the side of the crucible to act as getters. The arc melt furnace chamber was closed. Several cycles of vacuuming and backfilling the chamber with argon, an inert gas, were performed. Each cycle decreased the presence of impurities in the chamber. The cycling ended with backfilling the chamber to 250 torr below atmospheric pressure. An arc was initiated, and the material was melted and mixed for a few minutes. The sample was then flipped and mixed again. This process was repeated approximately four more times to ensure proper mixing and homogeneity. Figure A-47 is a photograph taken after the sample has been flipped and mixed several times. The chamber was then brought to the atmospheric pressure, and the sample was taken out of the chamber and weighed. Sample losses were noted. If the loss was greater than 0.003 grams, the fabrication of the sample was terminated. If the loss was negligible, the sample was then placed in the head of a drop cast mold and the chamber was closed. The process of vacuuming and backfilling the chamber with an inert gas was again performed. An arc was initiated, and the alloy dropped into the water-cooled copper mold. The sample was cast into a 6.5 mm diameter, round-bar specimen with a length of approximately 76 mm. The weight was then again recorded to account for material loss.

Radiographs, with a resolution of 0.1 mm or less, were taken of the round-bar ingots to locate any porosity, and to ensure that limited porosity would be present in the testing section of the fatigue specimens. The ingots were cut to length for fatigue, corrosion, and metallography samples for various tests using an electrical discharge

machine (EDM). The EDM created localized high temperatures in the material, but any crystallization was extremely localized and removed by grinding.

Amorphous samples to be crystallized for metallography, mechanical testing, or corrosion testing were placed in a vacuum furnace. The furnace was preheated to 600 °C. The entire glass tube that was the chamber was vacuumed to 10^{-6} torr by use of a mechanical and turbo pump in succession. The samples were in the glass tube during the vacuum process, but were not placed into the furnace until an adequate vacuum was achieved. The samples remained in the furnace for 5 hours and then were removed.

Metallography samples, 6.4 mm in diameter by ~ 1.6 to 3.2 mm in thickness, of the amorphous alloy were placed in resin, cured, and polished to a 0.5 μm finish. Some of these samples were etched with a nitric-hydrofluoric acid solution and observed with optical microscopy for crystalline regions. X-ray diffraction analyses were conducted on other samples using a Philips X'pert X-Ray Diffractometer to characterize the structure.

3.3 Production of Bulk Metallic Glass Composites

Collaborative research was conducted between the University of Tennessee, Knoxville, Tennessee and the Institute for Materials Research, Tohoku University, Sendai, Japan to design a procedure for fabricating nano-composite bulk metallic glasses (i.e., amorphous matrix and nanometer-sized crystalline phases). BAM-11, $\text{Zr}_{52.5}\text{Al}_{10}\text{Ti}_5\text{Cu}_{17.9}\text{Ni}_{14.6}$, was used as a base composition. Small amounts of palladium were added to this composition with a reduction of copper. The above composition was determined from an extensive literature review. One important article in determining to use Pd was written by Yavari et al. [89]. In this article, Yavari et al. had used small amounts of Pd in a similar bulk metallic glass composition, and found metastable,

quasicrystalline, and solid solution composites. Small amounts of Pd allow for diffusion controlled annealing of the glass. The exact compositions used in this study were:

$Zr_{52.5}Ni_{14.6}Al_{10}Ti_5Cu_{(17.9-x)}Pd_x$ (at. %), where $x = 0, 2.5, 5, 7.5,$ and 10 .

Each composition was mixed using an electric-arc furnace. A similar procedure was used as described in section 3.2. The alloy was then crushed into fine particles and placed in a quartz tube with a fine hole at the bottom. The quartz tube and contents were heated using an induction ring inside a vacuumed chamber. The temperature was monitored by an infrared camera. At $900^{\circ}C$, the sample was injected into a copper mold using a back pressure of argon, 1.5 kgf/cm^2 . Samples were either made into 2 mm or 6 mm diameter ingots.

Ingots were cut into smaller lengths to be used for x-ray diffraction, annealing, and differential scanning calorimetry using a diamond blade rotary saw. All samples were scanned using a 2θ range of 20° to 80° . Special note was made regarding the shape of the amorphous halo, and whether crystalline peaks were present.

Each of the five compositions were used for differential scanning calorimetry. A heating rate of $40^{\circ}C/sec$ was employed. The samples were stopped prior to melting, ~ 825 K. Special note was made for each sample regarding the crystallization and glass transition temperatures. Sections of each composition were placed in quartz tubes. The tube was then evacuated. The ends were sealed using an arc weld. The vacuum sealed samples were then annealed for 7 or 10 minutes at the following temperatures:

$$T_x + Y,$$

where T_x is the primary crystallization temperature, and Y is either 0, 10, or 20 degrees Kelvin. The heat treated samples were then used for x-ray diffraction once again. Changes in the amorphous curve were observed.

3.4 Dynamic Polarization Curves with Scratch Testing in 0.05 M Na₂SO₄

In order to provide the electrochemical data on the possible corrosion effects of condensed water vapor in fatigue testing of the BMG, cyclic and dynamic polarization tests, and scratch tests, were performed in distilled water containing 0.05 M Na₂SO₄ [6]. The small amount of sodium sulfate, which was regarded as non-aggressive, was added to the distilled water to provide adequate electrical conductivity for the electrochemical test. Samples used for the corrosion studies were drilled and hand-tapped approximately 2 mm into the specimen. A brass screw was placed into the sample. The corrosion samples were then placed in a mold with resin, cured, and ground to a P4,000-grit (FEPA, Federation of European Producers of Abrasives) or 1,200 (U.S. Standard) SiC finish, which corresponded to the surface finish of the fatigue specimens. The samples were ground within an hour of starting the corrosion testing to ensure a controlled thickness of the passive film. A nonconductive epoxy was placed along the metal-resin interface. The exposed surface of the sample was measured, and the surface area was calculated. The electrolyte was measured and poured into a two-liter beaker. A saturated calomel reference electrode was first checked and then inserted into the electrochemical cell. The brass screw of the metallic glass sample holder was attached to the working electrode via a j-tube. A plastic washer ensured that there was no electrolyte-brass interface. The counter electrode was attached to a small rectangular sheet of platinum, a very noble metal. The electrodes were attached to the potentiostat. The three electrodes

were then placed into the electrolyte and held in place with the working and counter electrode surfaces close to each other, but not touching.

Two electrochemical cyclic-anodic-polarization tests were conducted on the BMG-11 amorphous samples using an EG&G Princeton Applied Research Model 263A Potentiostat/Galvanostat with EG&G 352 SoftCorr III computer software [6]. Before each polarization scan was initiated, the corrosion sample was allowed to stabilize in the electrolyte for either one hour or until the corrosion potential, E_{corr} , changed by no more than 2 mV over a five-minute time period. The scan was started at 50 mV below E_{corr} and continued in the positive direction until an anodic current density of 10^4 mA/m^2 was reached or the potential was taken to an approximate value of 1,700 mV(SCE). At this point, the scan direction was reversed, and the scan was continued in the negative direction until the original potential was reached. The potential scan rate was 0.17 mV/s. In analyzing the cyclic-anodic-polarization behavior, a number of corrosion-related parameters were evaluated. These parameters are identified in the schematic polarization curves of Figure A-19, which illustrate typical behavior with regard to localized corrosion susceptibilities. This figure was described in section 2.4.2 in detail. Path 1, where the material is shown to be immune to localized corrosion is the appropriate path for BMG-11 tested in 0.05 M Na_2SO_4 .

Lastly, a third test was conducted of a dynamic polarization curve. The potential was scanned to 750 mV(SCE). At 100 mV above the corrosion potential, the sample was scratched with a diamond stylus to intentionally remove the protective passive film in a small region [6]. The sample was scratched thereafter every 100 mV for approximately 10 s. The anodic current density was monitored to determine whether the film would

reform, and if so, the reformation (repassivation) kinetics. This particular test also was related to the fatigue studies, in that, during corrosion fatigue, shear-band movement to the surface will break the passive film. In order for the environment to have a minimal effect on fatigue properties, the passive film must reform quickly.

3.5 Cyclic Polarization Curves in 0.6 M NaCl of Pre-Etched BMG Samples

The electrolyte used in this investigation was 0.6 M NaCl in distilled water, which simulated seawater. Amorphous BMG-11 samples were tested with a 600-grit SiC finish, which simulated an industrial finish. Immediately after grinding the surface of the corrosion samples, the sample was immersed in an undiluted nitric-hydrofluoric acid solution, containing 20 mL nitric acid and 0 to 0.2 mL of hydrofluoric acid for 5 to 30 seconds. Sample preparation and testing procedures were similar to section 3.4.

A similar etching solution was originally used to observe any possible presence of a crystalline phase in metallography and corrosion samples. Preliminary corrosion studies of Peter et al. were conducted using polished and etched BMG samples [55]. Two to five drops of hydrofluoric acid were used in 40 mL of nitric acid. These tests showed scattered results, but a very high average pitting potential. Later in the same study, samples were not etched because of the possible effects that the etching could have on the surface of the sample (i.e., more stable passive films for amorphous samples and etched surface defects in the crystalline samples). However, further study of this area could prove useful in developing a corrosion resistant, pre-treatment for Zr-based BMGs.

3.6 Hydrogen-Charging Samples for Fatigue Testing

In this experiment, the electrolyte used was a 1 N Sulfuric Acid Solution. This solution was chosen because of the high hydrogen activity; the pH was below 0.3.

Nitrogen was introduced into the electrolyte to eliminate dissolved oxygen, and deaerate the solution. This trend also kept the atomic hydrogen from quickly combining with the dissolved oxygen to form water. Once again, an EG&G Princeton Applied Research Model 263A Potentiostat /Galvanostat with EG&G 352 SoftCorr III computer software was used to create a potential difference between the Zr-based BMG and the saturated calomel reference electrode. However, this time it was used to create a cathodic potential difference. The EG&G equipment was used as a galvanostat in this procedure by keeping the current, and therefore the current density (area of the sample did not change during the test), constant. A constant, cathodic current density of 20 mA/cm^2 was used; this led to a potential difference of -0.75 to -0.95 V (SCE) . Since the goal was to supply electrons, the conventional current flow was away from the sample.

Prior to submersing the fatigue sample, both the bottom half and the top half were wrapped in non-conductive tape. Then, the bottom half of the specimen was placed in a non-conductive epoxy. Only the testing gauge section of the sample was visible, and not covered in any way. In this case, it was only the notched region, see section 3.5 for testing geometry and specifics. The surface area to be exposed to the electrolyte was measured. The current was then calculated to ensure a 20 mA/cm^2 current density. The sample was submersed only so that the testing section was below the surface of the electrolyte. In doing so, the user was trying to safeguard against areas outside the testing area cathodically charging. The sample was held at a current density of 20 mA/cm^2 for a total of 22 hours. The sample was observed for any pitting and/or corrosion byproduct. After charging, the tape and epoxy were removed from the samples. They were then viewed with a stereomicroscope to ensure no corrosion. Even though the sample was

being held at a highly negative potential, these steps must be made since the pH of the solution is extremely low. The samples were then tested in air following the procedure explained in section 3.5. The cyclic testing was initiated within 6 hours of charging. Micro-hardness testing was performed on hydrogen-charged samples to compare as-cast versus charged samples. A 500 gram load was used.

3.7 Tensile-Tensile, Uniaxial Fatigue Testing In Air of Notched Button-Head Samples

Careful attention was provided to fatigue specimens during the cutting and machining processes. Samples were arranged in a manner to minimize porosity, and to keep porosity out of the testing section. By prearranging the cutting and the notching of the test section, premature fracture due to porosity was largely eliminated. The samples made into fatigue specimens were machined with a lathe and then ground. The samples were then polished using a P4,000-grit (FEPA, Federation of European Producers of Abrasives) SiC paper to a 5 μm finish within one to two hours of initiating the fatigue tests. Figure A-38 shows the button-head geometry that was used for the majority of the fatigue specimens. The gripping system and the specimen geometry were modified versions of that used by Dr. Ken Liu (ORNL) for testing ceramics and other brittle materials. Preliminary results indicated a conventional button-head geometry resulted in premature fracture at low stress ranges (~ 670 MPa). Figure A-48 is the initial testing geometry. Cracks would initiate at the localized points of contact of the gripping system before cracks initiated in the reduced section of the test specimen. One air test and one vacuum test performed at a stress range of 1,066 MPa were recorded because the stress range was high enough that this problem was not encountered. The modified gripping

system used largely eliminated the problems with the initial gripping system by increasing the area of contact.

A Material Test System (MTS) Model 810 load frame was used for fatigue testing. The machine was aligned within 50 μ strain prior to use, and as required. Samples were tested at various stress ranges with a load ratio (R), the minimum load divided by the maximum load, equal to 0.1 (i.e., $R = 0.1$), and a frequency of 10 Hz. Peak and valley load values for individual cycles were intermittently recorded for verification. Upon failure, samples were removed and stored for later examination by SEM.

3.8 Tensile-Tensile, Uniaxial Fatigue Testing In Vacuum of Notched Button-Head Samples

Prior to testing the specimens in vacuum, the chamber was evacuated and backfilled with ultra-pure argon or helium three times or more. A mechanical pump and a diffusion pump in series were used to evacuate the chamber. A gettering oven was employed to reduce impurities from the inert gas before entering the chamber. After the final backfill, the chamber was evacuated to 10^{-5} to 10^{-6} torr. An ionization gauge with a hot tungsten filament open to the chamber environment was used to monitor the vacuum at low pressure. The vacuum samples were tested in the same manner as the air specimens and at the same stress ranges.

Subsequent experiments were performed on fatigue specimens in vacuum without the prolonged use of an ionization gauge. The ionization gauge was turned off after recording the vacuum pressure, or was never used. In the first test of this series, a thermocouple was attached to the testing gauge section of the fatigue specimen. The

temperature was monitored by a digital read-out, and then recorded every 2,000 cycles and upon fracture. Also, tests were conducted where silica grease was administered to the fatigue specimens around the gripping section. Each of the above sets of circumstances were used to better identify the detrimental effect observed in vacuum for BMG-11 as discussed later in the Results and Discussion section.

3.9 Tensile-Tensile, Uniaxial Fatigue Testing In Air of Notched Button Head Samples with Various Surface Finishes

The samples were prepared in the same manner as in section 3.5. After polishing the sample completely with a 5 μm finish, random samples were chosen, and either a 180-grit finish (78 μm), a 400-grit finish (22 μm), or a P4,000/1,200 grit finish (5 μm) was applied to the notched testing gauge within a few hours of initiating the fatigue tests. A Riddensstock R-600 Profilometer was used at Oak Ridge National Laboratory to measure the arithmetical standard deviation of the surface roughness, R_a . Measurements were taken longitudinally along the sample. The profilometer moved in a direction parallel to the axis of loading, and perpendicular to the grinding marks. The measurement was performed on the notched region of the samples that had undergone the final grinding process. The surface roughness was then compared to the grit number, the grit particle size, and the fatigue results. The samples with different surface finishes were tested in the same manner as specimens discussed in section 3.5. Lastly, a rectangular beam specimen, as described in 3.11, was finished with 180 grit paper on only the tension side of the specimen prior to testing the sample in cyclic three-point bending at a stress range of 1,300 MPa. The sample was stopped every 500 to 1,000 cycles, and observed with a scanning electron microscope for any cracking.

3.10 Fatigue Testing of BMG Button Head Samples with Different Test Gauge Lengths (Changing the Area and Volume Tested)

Limited testing was performed on uniaxial specimens to observe any fatigue-endurance limit variance due to changes in testing surface area and/or volume. Specimen geometries were similar to those in sections 3.5 to 3.7. However, a gradual taper was implemented instead of a small/severe radial notch. This was to eliminate the large stress concentration factor associated with the notch. The stress concentration was less than two percent increase. The results listed in chapter four are nominal stress values. Two geometries were used. These geometries can be seen in figure A-49. Please note that the radial taper and the nominal testing cross section are the same for both geometries. The only difference is the testing gauge length, a single plane for geometry A and a 4 mm long cylinder for geometry B. Samples were finished and tested in the same manner as the notched specimens in section 3.5.

3.11 Three- and Four-Point Bend Fatigue Testing In Air of Rectangular Beam Specimens

Samples also were studied in three- and four-point bend loading as well as uniaxial loading. Three- and four-point bend studies were performed by Mr. Mark Morrison and myself. Beam specimens machined to 3.5 mm in height, 3.5 mm in width, and 30 mm long were used. These dimensions were within 0.1 mm prior to the final stage of polishing (as-received from the machine shop). The length of each beam was cut from an as-cast ingot using an EDM. The samples height and width dimensions were ascertained by grinding the centered ingots. The sample was finally polished from 600 SiC paper to P 4,000 / 1,200 grit paper prior to testing. The last grinding marks were

oriented in the longitudinal direction, parallel to the bending stress direction. After the final polish, the height and width were measured a final time, and used to calculate the load required for the given stress range.

All bending experiments in the present study utilized an outer loading pin distance of 20 mm. The central pin was centered for three-point bending. The inner loading pin distance was 5 mm for four-point bending. The height-width ratio and the pin spacings were based on a mechanical fatigue paper written by Zhai et al [90]. These distances and dimensions maintained a constant maximum bending load for the entire span of the beam between the two inner pins for four-point bending. The bending fixture layout and beam dimensions can be seen in figure A-50.

A Material Test System (MTS) Model 810 load frame was once again used for fatigue testing. The machine was aligned within 50 μ strain when required. The bending loading fixture was comprised of a ball joint at the top connection of the loading head. This ensured there was not a supplementary load due to misalignment of the machine, or that the load was not evenly distributed amongst the pins. The loading head was centered before each test. Therefore, alignment was only required if the ball joint did not fall at the center of the loading head, and was not centered between the two inner pins / directly above the center pin. In uniaxial testing, the load frame was aligned before each test. Samples were tested at various stress ranges with a load ratio (R), the minimum load divided by the maximum load, equal to 0.1 (i.e., $R = 0.1$), and a frequency of 10 Hz. Peak and valley load values for individual cycles were intermittently recorded for verification. Upon failure, samples were removed and stored for later examination by SEM.

Several samples were annealed in a similar manner as listed in metallography, five hours at 600°C. These samples were fully crystalline and were similar in appearance to figure A-16. The author tried to test these samples in fatigue. However, the samples failed upon loading, and at very low stress levels. These results were used in comparison with samples that had been fabricated at the University of Tennessee in a new arc casting furnace and had observed low lifetimes.

3.12 Scanning Electron Microscopy

A LEO SEM, a S3500-Hitachi SEM and a S360-Cambridge Instruments SEM were used to view metallography specimens, and corrosion and fatigue samples after testing. Specimens were viewed under both backscattered and secondary electron methods. Chemical analyses of microscopic areas were performed using the ancillary fluorescent x-ray spectrometer [91]. Elements present and composition percentages were recorded. An in-lens SE detector on the LEO scope also was used to examine included areas not well observed by offset detectors. The SEM is an incredibly useful tool for studying fracture morphologies, investigating compositional differences, observing microscopic images that optical microscopy cannot resolve, and identifying fracture mechanisms.

CHAPTER 4: RESULTS AND DISCUSSION

4.1 Amorphous Structure and Fabrication

Over fifty drop cast samples, ~ 6.5 mm in diameter and ~ 76 mm long, were fabricated for the following studies. Random samples were cut using the EDM for metallography slices on the top, bottom, and middle (where possible). Various samples were polished, etched, and observed for crystalline structures. Results were good with very little to no crystallinity present for the majority of samples fabricated at ORNL. The limited crystallinity found was in the form of small starlets, approximately a micrometer in size. These starlets sometimes formed thin spirals just inside the circumference of the sample. The band-widths of these spirals were on the order of 100 micrometers. Figure A-51 is an example of a spiral at a low magnification. The limited amount of crystallinity was in agreement with BMG-11 samples fabricated and observed at ORNL, and was acceptable for our testing purposes. The spirals were not present the entire length of the sample. The crystallinity was largely removed in the bulk of fatigue samples during the machining process. However, the crystallinity varied from sample to sample. The meta-stable nature of BMGs increases the difficulty in controlling this aspect. Metallography and x-ray diffraction do not ensure that the fatigue specimens are without any crystals the entire length of the specimen. Samples for corrosion testing were covered with an epoxy around the circumference. The epoxy covered the majority of the limited crystallinity. For both areas of study, only ingots without any non-uniform shrinkage during cooling, casting heads with a glassy mirror-like appearance, and

samples that underwent less than three thousandths of a gram weight loss were used to make specimens.

Samples that were annealed for crystallinity obtained a crystal structure. Specimen preparation for these samples was slightly more difficult due to their brittle nature. Crystallinity was observed in these samples by both microscopy and x-ray diffraction. The crystals as observed in optical microscopy were on the order of 500 nanometers to 6 micrometers. Figures A-15 and A-16 are good examples of the amorphous and crystal structure, respectively. X-ray diffraction patterns recorded for a crystalline corrosion sample and an amorphous metallography sample are presented in Figure A-17. This x-ray diffraction pattern for the amorphous sample contained no crystalline peaks. However, a wide peak identifying limited short-range order was present. The pattern for the crystalline sample contained crystalline peaks.

4.2 Production of Bulk Metallic Glass Composites

Over a two and a half month time period, collaborative research was performed between the University of Tennessee, and the Institute for Materials Research (IMR), Tohoku University, Sendai, Japan. Five different compositions were made in 2 mm and 6 mm diameter injection cast ingots. A total of 10 ingots were cast at IMR. X-ray diffraction patterns of as-cast 2 mm samples of all five compositions exhibited a broad amorphous peak from a 2θ value of 30 to 45 degrees. No crystallization peaks were present. Figure A-52 is the 2 mm diffraction patterns. The 0 % Pd, 2.5 % Pd, and 5 % Pd were still amorphous in the 6 mm diameter ingots. However, small crystalline peaks were observed in the x-ray diffraction patterns of the 7.5 % Pd and 10 % Pd ingots cast in 6 mm. Figure A-53 is the diffraction pattern of the 7.5 % Pd, 6 mm ingot; the highest

intensities of the crystalline peaks are indicated. Differential scanning calorimetry measurements were taken of the 2 mm samples. An example graph of the temperature versus the differential calorimetry is presented in figure A-54. The various crystallization temperatures are summarized in table A-3. The melting temperature was only observed in the 2.5 % Pd sample, as seen in A-54. The first heat treatment schedule was to anneal 2 mm samples of all compositions at their respective crystallization temperatures for seven minutes. All five of the samples were still amorphous, and had similar broad peaks comparable to the as-cast samples. A meeting with Dr. Inoue, IMR Director, was arranged. A new heat treatment matrix was developed where 2 mm and 6 mm diameter samples of the 2.5 %, and 5 % Pd material would be annealed for ten minutes at the crystallization temperature, ten degrees above the crystallization temperature, and twenty degrees above the crystallization temperature. Ten minutes at the crystallization temperature was enough to cause minor crystallization peaks in the 2.5 % Pd sample. The x-ray diffraction pattern can be seen in figure A-55. Ten minutes at twenty degrees above the crystallization temperature may have developed crystalline peaks in the 5 % Pd samples. However, it is difficult to decide if it is noise or actual peaks in figure A-56. In conventional x-ray diffractometers, resolution of crystalline phases is around 50-100 nm. Therefore, some crystallization could have occurred prior to the formation of crystalline peaks in the diffraction pattern. However, the original goal was to learn to fabricate BMG composites as per IMR casting and annealing procedures and using IMR equipment. In regards to this goal, the project was a success. The composite samples are in an ongoing compressive strength investigation by another colleague. If any of the samples exhibit high strengths, further research may be conducted on metallography and

fatigue studies to better understand the size of the crystalline phases and their effect on fatigue behavior.

4.3 Polarization Curves and Scratch Testing in 0.05 M Na₂SO₄

4.3.1 Cyclic Polarization Curve in 0.05 M Na₂SO₄

Table A-3 contains the critical corrosion parameters for the cyclic polarization curves performed on amorphous BMG-11 samples in a 0.05 M Na₂SO₄ electrolyte [6]. Figure A-57 shows the cyclic polarization curves for these tests. The amorphous material was in the passive state at the natural corrosion potential, E_{corr} , with a corrosion current density (i_{corr}) of 0.4 mA/m² and a corrosion penetration rate (CPR) of 0.4 μm/year [6]. This corrosion rate is extremely low relative to most materials. On reversing the potential scan direction, the current density decreased in magnitude, indicating that the amorphous material has no susceptibility to localized corrosion, at any potential, in this electrolyte. This is quite different than the electrochemical behavior in the 0.6 M NaCl electrolyte at high potentials.

4.3.2 Dynamic Polarization Curve with Scratch Tests in 0.05 M Na₂SO₄

The dynamic polarization curves for BMG-11 in water containing 0.05 M Na₂SO₄, for undisturbed and scratched conditions, are presented in Figure A-58. The periodic scratching (every 100 mV) to locally remove the passive film resulted in drastic anodic-current-density spikes (high local corrosion rates) [6]. However, in each case, when the scratching was stopped, the current density immediately decreased to the passive value, indicating rapid repassivation. As related to corrosion-fatigue testing in humid air (where a thin layer of condensed water could exist on the specimen surface), these results indicate that when shear bands move to the surface and create an offset,

thereby breaking the oxide film, and exposing a fresh, unprotected surface, that surface should immediately passivate. The very low corrosion penetration rate of this material in water and the ability of BMG-11 to quickly reform a passive film, limit the influence of corrosion mechanisms on the fatigue lifetime of this metallic glass in air or water.

4.4 Comparison of Vacuum and Air Fatigue Behavior

4.4.1 Results

Figure A-59 is the stress-range and number-of-cycles relationship for specimens tested in vacuum and compared with air (some of these results had previously been published) [6,7]. The vacuum data is represented by circles in this plot regardless of the use of an ionization gauge or the location of failure. The stress-range values reflect the stress concentration factor (K_t) of 1.55 or 1.48 [54,92] at the notched section of the specimens. Air results were mentioned previously in the literature survey, but have been updated to show current results. At a frequency of 10 Hz, no detrimental effects of water vapor in air were observed on the fatigue properties of BMG-11 [6,7]. In fact, the fatigue behavior in air produced longer lifetimes than in vacuum. This result seems to be produced by an environmental effect that is directly related to the vacuum condition since the air data contained less scatter than vacuum. Possible unfavorable conditions associated with the vacuum could be adiabatic heating from the lack of convective heat transfer, lack of beneficial environmental effects (e.g., oxygen to form an oxide), and/or complexities in the vacuum process that could generate detrimental species.

The scatter in the vacuum data made it difficult to determine a stress-to-life relationship for values around the fatigue-endurance limit [6,7]. However, high stress range lifetimes are similar to air results. Above 1,000 MPa, the vacuum and air data

share the same stress-to-life relationship. The fatigue-endurance limit for the BMG-11 samples tested in vacuum is still unknown. At least one sample tested at 907 MPa experienced an order of magnitude increase in number of cycles to failure. Samples tested at a stress range of 750 MPa, 150 MPa below the fatigue-endurance for samples tested in air, failed before ten million cycles. The data indicates a lower stress range improves the life expectancy of samples tested in vacuum. However, vacuum samples were achieving over one million cycles as high as 850 MPa. This suggests that the mechanism causing lower lifetimes in vacuum is environmental and time oriented.

4.4.2 Discussion

The majority of the vacuum specimens that were tested at or below 907 MPa failed near the gripping section instead of at the notched section. Only one specimen in air failed at the gripping section out of all the tests performed. Figure A-60 is the same S-N plot as before, but the location of the failure is noted. Interestingly, the gross stress at the gripping section for the samples tested near the air fatigue-endurance limit is only around 350 MPa. This is extremely low compared to an effective stress of 900 MPa, or a nominal stress (removing the stress concentration) of 650 MPa.

The ionization gauge monitors the pressure under high-vacuum conditions, and is open to the testing chamber. A hot tungsten filament is used in the gauge. The hot tungsten filament can dissociate residual water vapor into atomic hydrogen and oxygen [93]. If the test material is susceptible to hydrogen, BMG-11 could absorb the limited atomic hydrogen. In the following section, it has been shown that BMG-11 is susceptible to hydrogen. Figure A-61 is a schematic diagram illustrating this process. Even in small amounts, the absorbed hydrogen could embrittle certain materials. This embrittlement

could lower the time for crack initiation, and, hence, reduce the observed lifetime of the sample. George and Liu observed a similar phenomenon with Ni₃Al [93,94]. By turning off the ionization gauge, this potential source of atomic hydrogen, and the resulting decrease in fatigue life, would be eliminated.

Preliminary tests conducted in vacuum without the prolonged use of the ionization gauge seemed to result in improved fatigue lifetimes [6,7]. However, further studies without the use of the ionization gauge below the fatigue-endurance limit in air seemed to have similar results to those samples tested with the ionization gauge. The test results for both sets of vacuum data are shown in Figure A-62. From these results, it seems the ionization gauge does not play an active role in decreasing the fatigue lifetimes of the specimens tested in vacuum.

Almost all vacuum samples near or below the air fatigue-endurance limit failed outside the notched region, within the area of the gripping section, at low lifetimes compared to the air data. In fact, at a stress range of 907 MPa or less, eleven out of twelve samples tested in vacuum failed outside the testing section. This is compared to only one sample tested in air. All test results for the various conditions are provided in figure A-63. These results may be caused by more than one condition. Since specimens tested in air at this stress level have not shown this behavior, the vacuum environment may be the detrimental condition.

SEM images on one of the vacuum samples near the initiation site, exhibited scratch markings that were produced by the copper inserts of the grips. Figure A-64 is an SEM image of the scratches near the crack initiation site. The first inclination would be to assume the scratches create significant stress concentrators that prematurely generate

cracking. However, the movement of the copper pieces and the direction of the markings are parallel to the loading direction. This trend usually negates the effect of the markings to create local stress concentrators. Moreover, air results would probably be impacted by this mechanism as well since wear marks were also located on samples tested in air. However, the copper pieces may be removing the original oxide from the surface. In air, this oxide would be able to grow. In vacuum, this oxide will have difficulty re-passivating due to the low amount of oxygen. In the author's earlier work, it was suggested the loss of the oxide may increase the absorption of hydrogen, embrittling the localized area. As indicated above, further investigations exhibited no difference between results with and without the ionization gauge. However, the loss of oxide would allow a detrimental species to better infiltrate the glassy material.

In order to minimize the effects of wear in vacuum, one sample was painted with carbon paint near the gripping sections only, and another sample was covered with silicon grease near the gripping sections only. The paint and grease were used as a buffer between the copper grips and the material itself. The results of the tests can be observed in A-62. The carbon paint did not seem to greatly improve the number of cycles to failure. The silicon grease resulted in longer lifetimes than the rest of the vacuum results at this stress range with a performance of over one million cycles. However, this sample failed before ten million cycles. After failure, these two samples were examined. The paint and the silicon grease seemed to be mechanically removed with time. This feature could be the reason for the reduced lifetimes in comparison with the air sample that exceeded ten million cycles.

The possibility of detrimental effects due to adiabatic heating was tested. The fatigue sample tested at 977 MPa that failed at 31,994 cycles had a thermocouple attached to the notched section [6,7]. During the entire test, the temperature was recorded as 25 °C. The low fatigue lifetimes in vacuum do not appear to be caused by adiabatic heating. There was concern that localized plastic deformation (at/near the fracture surface) created heat that could not be removed by convection, only by conduction. The heat would then accelerate the crack growth by softening the material. However, the temperature of the notched section remained at 25 °C, indicating that no significant, macro-scale adiabatic heating occurred. Conversely, a thermocouple is not sensitive enough to measure the change in temperature at small space resolutions.

The last concern of the vacuum samples may be the reason for early failure. On most of the vacuum samples post-testing, a fused material could be seen on the outside surface of the specimen immediately in the area of crack initiation. Originally, it was thought that this material was softened bulk metallic glass. Figure A-65 exhibits the fused material as observed on vacuum samples near the crack initiation site. Using a secondary electron image, the material did not exhibit any contrasting differences from the base BMG material; this effect may be expected since secondary electrons are good at providing information regarding contour or topological differences, but are not good at indicating chemical differences. In the past, the absence of chemical contrasting had made it difficult to observe the extent of the fused material. Debris had been found on samples tested in air near the gripping section, but the material appeared loose, and was more of an oxide. Figure A-66 also had an image of such a sample tested in air. Energy Dispersion Spectroscopy (EDS) was conducted on both types of samples. The fused

material was extremely high in copper, and low in oxygen. Figure A-67 is an EDS map illustrating the observed spectrum for a K alpha energy level of copper for the vacuum sample. EDS of the loose material on the air specimen was high in oxygen. It could be that the copper grip removes the oxide from the surface of the sample. In vacuum, the oxide is not able to repassivate. The continued interface with copper particles and the heat associated with friction fuses the sample to the surface. This is made possible without having the protective oxide. Copper adsorption and embrittlement may occur. However, not much literature exists on this type of phenomenon. One article citing Russian workers observed copper embrittlement in commercial steels at 50°C [95]. However, the article was in regards to isotope reactors, and it was not clear if radiation played a part in this mechanism. Another possible mechanism is the diffusion of copper into the bulk metallic glass induces crystallinity which leads to early crack-initiation. The grip insets were chosen to be copper because of copper's malleable and soft nature. Future testing could be conducted with nickel or another material used for the grip insets. This trend could possibly elucidate the effect of copper. However, less malleable materials may negatively impact the performance of samples tested in vacuum as observed in early studies where point contact of tool steels led to premature fracture.

4.4.3 Scanning Electron Microscopy of Button-Head Uniaxial Specimens

The fracture surface images observed via SEM of the fatigue specimens were similar to the morphologies reported by Ritchie et al. [1]. Three distinct regions could be observed on the fracture surface: a fatigue area, an overload, or fast crack growth area, and shear lip regions near the surface surrounding the overload area. Figure A-68 is a

secondary electron image containing all three regions. Beyond the typical morphologies found in these areas, there are some unique features that will be discussed.

The fatigue area is dominated by striations or bands of three distinct sizes. One set of striations is on the order of 5 to 10 micrometers, and is only visible near the overload fracture area. The mid-size striations are 1 to 2 micrometers in size. They are the most prominent feature on the fatigue surface. Figure A-69 depicts these two sets of striations. The author believes both of these striations are associated with corrections to the crack propagation direction. Shear deformation in BMGs prefers to occur at a 56 degree angle to the loading direction rather than a 45 degree angle as observed in monotonic tensile loading of bar specimens. The increase in the fracture angle has been associated with part of the normal stress component acting in shear [16]. A similar phenomenon could act in fatigue. In order for the shear deformation to occur, the crack would have to slant slightly away from the plane perpendicular to loading. Micro-cracks and shear bands at approximately 20 to 30 degree angles from the crack propagation plane can be seen on the outside surface of a BMG beam specimen in figure A-70. The round-bar and rectangular beam specimens used for these experiments are thick compared to the size of the plastic zone. Therefore, a plane-strain condition is prevalent. A crack propagating in a BMG would correct for itself during the unloading process. The largest striations, seen only near failure, may be more drastic corrections to the crack propagation direction.

The finest striations are on the order of 100 to 500 nanometers. Figure A-71 is a secondary electron image showing these striations on a medium size striation as discussed above. Notice these striations do not have the resolution of the other two sets.

The author believes that these finest striations are associated with individual cycles. Fatigue striations can be associated with either one of two mechanisms [54]. The first mechanism is associated with crack tip blunting and sharpening. During loading the plastic zone increases, the material in front of the crack softens, and the crack begins to become blunt. As the load is released and the crack displacement begins to lessen, the crack sharpens. A second mechanism that has been associated with fatigue striations is slip mechanisms occurring along preferred orientations. Since BMGs do not contain conventional vacancies and dislocations for slip mechanisms, the first mechanism must be correct. Ritchie et al. [5] has described a similar scenario. A mirror-like surface finish close to the crack initiation site can be found on most fatigue surfaces. This was also reported by Ritchie et al. [5]. Figure A-72 is a secondary electron image of a mirror-like surface finish close to crack initiation.

The overload surface as well as shear lips were typical of what is usually found in fatigue specimens of BMG. The overload fracture surface was rough and chaotic, as would be associated with “bulk” plastic deformation. However, a vein morphology was present as is shown in Figures A-73, A-74, and A-75 upon closer examination. Liquid droplets were visible intermediately along the veins. This type of behavior is associated with Taylor instability, and is found in adhesives and grease film separation [1,2,3,4,5]. The author believes this mechanism may be due to highly localized, perfectly plastic behavior due to the amorphous material exceeding the glass transition temperature from adiabatic heating. The adiabatic heating would be associated with the quick energy released upon fracture, and the conversion of elastic energy into plastic energy. If the material reaches the super-cooled liquid region above the glass transition temperature, the

viscosity of the local material would decrease and softening would occur. The material would become liquid (the only kinetically distinguishing characterization from a glass and a liquid is the level of viscosity). In many of these bulk metallic glasses, the glass transition temperature could be a few hundred degrees below the liquidus temperature. The shear lip is void of the rough surface feature, but still contains the “vein” like structure. Figures A-76, and A-77 are examples of observed shear lips. The smooth surface of the shear lip may have to do with the crack changing from plane strain to plane stress.

Unlike Ritchie et al.’s reported results, some outstanding characterizations were also observed. Two samples are used as examples for some of the more unusual surface morphologies found. A sample tested at 698 MPa that failed at a lower than anticipated number of cycles, referred to as Sample 1, had a large flat planar area at crack initiation that was surrounded by a rough surface area. The 977 MPa sample that failed within the data trend, referred to as Sample 2, contained a large protrusion/depression close to the crack initiation site. Lastly, the localized crystallinity has an effect on the fracture morphology, and can be observed in almost every fatigue specimen. Depending on the quality of the specimen, there may be more or less. Each of the outstanding characteristics is described below.

Though Sample 1 showed some typical characteristics of a fracture surface of a Zr-based BAA fatigue specimen, the area around the crack initiation site was not typical (Figure A-78). A flat planar region that slanted into a depression on one side (and slanted into a protrusion on the other side) was located at the crack initiation site. Figure A-79 is a SE image of the crack initiation. At higher magnification, striations were not visible in

this area. A back-scattered electron (BSE) image, Figure A-80, was also taken of this area to see if there were any major chemical composition differences between this area and the surrounding area. No major chemical difference between the two areas was observed. A secondary crack or crack branching was located at the low point of this depression, Figure A-81. The surrounding area was rough and striations were not visible at higher magnification (Figure A-82). Further crack branching, and radial marks were visible through this area. Though these morphologies were present in other samples, they were much more numerous in Sample 1. A vein morphology was not present in this area. The sample was tilted ten degrees away from the Everhart-Thornley detector in order to observe the outer surface of the fatigue specimen. Figure A-83 is a SE image of the outer surface. Grinding tracks were present including one near the crack initiation site. The grinding tracks may have lowered the lifetime of the specimen before crack initiation because of the high notch sensitivity of the material. The rough area around the crack initiation site was an indicator for higher than normal crack growth rates. However, the mechanism causing the formation of this area around the crack initiation site is not clear. They may have to do with localized crystallinity or the sides of the crack growing quickly to keep up with the crack front.

Prior to viewing the Sample 2 in the SEM, it was thought to be a good control sample to show the normal morphology. Sample 2, just like Sample 1, did share many similarities with previous fatigue surface descriptions, but there were some outstanding characteristics as well. Figure A-84 is a SE image of the fracture surface at low magnification. As can be seen in Figures A-85, a large protrusion/depression was found in the fatigue region close to the crack initiation site. This was uncharacteristic for most

amorphous materials. Unlike Sample 1, the crack initiation site did not seem unusual (Figure A-86) even though the protrusion/depression was within proximity of it. Fatigue striations were visible on the surface of the initiation site. Shortly after the initiation site, the fracture surface sloped upward/downward at a moderate rate. At the summit of the protrusion, there is a plateau as shown in Figures A-86 and A-87. Dimpling was found in this area. This trend was not seen in any other samples viewed in the SEM or in any of the literature. The origin of this dimpling is not known. BSE images were taken of this region (Figures A-87 and A-88). Because of the change in the elevation, it was hard to be certain if there were chemical composition differences. However, major differences did not appear to be present. The fracture surface around the protrusion appeared to agree with the common fatigue morphology for BMGs with striations (Figures A-89 and A-90). Dimpling could not be found on the depression fracture surface half. Upon investigating the fracture surface of the depression side (Figure A-91), no dimpling was observed (Figure A-92). At the deepest section of the depression, crack branching was observed as shown in SE Images (Figures A-93 and A-94). The location of the plateau was estimated and both BSE and SE images were taken of this region to identify any possible differences (Figure A-95 and Figure A-96, respectively). No differences were observed between these two modes of operation.

Small local crystals were observed using the SEM. These crystals were the same 1 to 6 μm diameter crystals that are visible in etched specimens of as-cast BMG-11 using optical microscopy. Figure A-97 is a low magnification of the fatigue region of a fracture surface. The crystals are indicated by arrows. Figure A-98 is an image of both the optical microscope image of polished and etched as-cast samples on the left, and a fatigue

striation region containing the crystals. The observation of many of these crystals is correlative to a lower fatigue life. This is especially true for bend specimens, and will be discussed further in section 4.9. However, most of the vacuum samples tested at or below the air fatigue-endurance limit that resulted in lower lifetimes contained very few crystalline regions. In fact, the samples tested in air that failed near the same number of cycles contained many more crystals than the vacuum samples. Figure A-99 compares the morphologies of two samples with low lifetimes near the air fatigue-endurance limit; the one on the left is a sample tested in air and the one on the right is a sample tested in vacuum. Observation of these crystals did not necessarily affect the stress intensity range at failure. This indicates that the detrimental effect of these impurities is to lower the crack initiation time period. Once again this is indicative of sensitivity to crack initiation.

4.4.4 Observed Striation Spacings Compared to Stress Intensity Ranges

All three sets of striations have been measured intermittently along the fracture surfaces where possible. Striation spacings versus stress intensity range divided by Young's Modulus for two samples tested at 907 MPa in air are compared with the Bates and Clark formula [96] for conventional crystalline alloys in figure A-100. The crack growth exponents are much lower for the metallic glass striations. The finest striations are small compared to the conventional crystalline alloy relationship, and the medium and large striations are above this correlation. The average fine striation size for sample one, which is the sample that went 282,785 cycles, is 0.197 μm . The crack length at fracture was 1.649 mm. Therefore, the estimated total number of cycles to failure is 8,371. This is only a small portion of the observed number of cycles to failure, but is in good agreement with the theory of crack initiation sensitivity in these materials. In

comparison, the medium size striations would only total 534 cycles. This sample had a fracture stress intensity range of $48.3 \text{ MPa}\sqrt{\text{m}}$. This is close to the reported fracture toughness of similar Zr-based BMGs tested by Ritchie et al. [5]. The other sample measured failed at 20,993 cycles. The average fine striation size for sample two is $0.238 \mu\text{m}$. The crack length at fracture was 1.309 mm , slightly shorter than sample one. The estimated total number of cycles to failure is 5,500 cycles. The medium striations would have estimated 439 cycles. This sample failed at a stress intensity range of $36.2 \text{ MPa}\sqrt{\text{m}}$. Ritchie et al.'s/Gilbert et al.'s [2,3,5] fatigue specimens failed at a stress intensity range of 10 to $12 \text{ MPa}\sqrt{\text{m}}$, depending on the article. Paris law or a modified Paris law is often used to fit region 2, or the stable crack growth region, for data comparing crack growth rates versus stress intensity ranges. The Paris law equation was discussed in section 2.5.7 as equation 2.1. Between various papers [2,3,5], Ritchie et al.'s/Gilbert et al.'s crack growth constant, C , and crack growth exponent, m , range from values of $2 \times 10^{-2} \mu\text{m}/\text{cycle}$ to $2 \times 10^{-5} \mu\text{m}/\text{cycle}$, and $1.2 \text{ MPa}\sqrt{\text{m}}$ to $2.7 \text{ MPa}\sqrt{\text{m}}$, respectively. Figure A-101 exhibits the various Paris law relationships with the BMG-11 small striation data. The average Paris law relationship for this set of data uses a C value of 0.0167, and an m value of 0.8. The BMG-11 striations are much larger than those reported by Ritchie et al./Gilbert et al. [2,3,5], and the relationship does not fall close to any of their curves. The poor agreement in the crack growth exponent could be an error in measuring the striations at low stress intensity ranges. Topological contrasting definition is weak at these low values, and measuring fatigue striations is difficult even with good resolution. However, their results [2,3,5] were at low stress intensity ranges, and the stress intensity range at

failure was at or below $12 \text{ MPa}\sqrt{\text{m}}$. In later work performed by this same group, Gilbert et al. [2] fit their data with a modified Paris power-law relationship [2,97]:

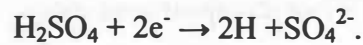
$$\frac{da}{dN} = C'(K_{\max})^n (\Delta K)^p \quad [4-1]$$

where C' is the scaling constant and is equal to $C(1-R)^n$, n and p are crack-growth exponents and their summation should be equal to m , R is the load ratio, da/dN is the crack growth rate and is discussed here in terms of $\mu\text{m}/\text{cycle}$, ΔK is the stress intensity range, and K_{\max} is the stress intensity at failure. This is a much more useful expression in comparing results between different compositions since the fracture strength of these materials vary. Figure A-101 contains this equation for BMG-11 results. The same p value as used in Gilbert's results [2] was used here. C' and n were determined from the Paris law relationship used earlier, and K_{\max} was an averaged value of the stress intensity range at failure for the two samples. The resulting modified Paris law does not fit the relationship of the data as well as the original Paris law, but does fit into the data itself. This is an implication into the fracture toughness of the material used. The low stress intensity ranges at failure for Ritchie et al.'s/Gilbert et al.'s results [2,3,5] may be an indication of the quality of the metallic glass used. Figure A-102 is an secondary electron image of both (a) the BMG-11 striations, and (b) Ritchie et al.'s Viterloy 1 [5] striations at ΔK values of $16 \text{ MPa}\sqrt{\text{m}}$ and $10 \text{ MPa}\sqrt{\text{m}}$, respectively. The fine striations are indicated on the figure along with the direction of crack propagation. These sets of fatigue striations seem to be similar in size. Ritchie et al. [5] reported striations larger than the crack growth rate measurements perceived. The BMG-11 surface seems to be

smooth, where as the Viterloy 1 surface seems to have a grain-like rough surface. This may also be indicative of crystallization.

4.5 Fatigue Results of Hydrogen-Charged Samples

In order to understand the possible effects of hydrogen on the fatigue lifetime of bulk metallic glasses, introducing the surface of fatigue samples with hydrogen would provide a worse-case scenario for environmental effects. Cathodically-charging a sample in a low pH acid is a convenient method to induce atomic hydrogen at the surface. By introducing electrons to a sulfuric acid solution, the following half cell reaction occurs:



In effect, the solution becomes more basic, higher pH, as the reaction continues. However, the acid solution used in this experiment is extremely acidic, and less than a 0.1 change in the pH was observed from the beginning to the end of the test. Atomic hydrogen will then go on to form H_2 molecules that will then aggregate to form a vapor. This can be seen during the experiment as bubbles continue to be produced on the cathode, in this case the BMG sample. However, it is the atomic hydrogen first produced on the surface of the sample that is usually accepted and diffused into the sample allowing for absorption. Gebert et al. has shown in a similar Zr-based BMG composition that hydrogen absorption ratios can be as high as $\text{H}/\text{M} = 1.65$, and remain amorphous [98]. The author suggests two possible scenarios based on two existing atomic models. An existing theory based on the free volume model is that hydrogen diffuses into areas of excess free volume sites (e.g., near large atom locations, such as Zr and Ti) [81]. The hydrogen would then retard viscous flow by occupying these sites of free volume (see section 2.5.1 for atomic mobility mechanisms). The second possibility is that atomic

hydrogen diffuses to locations where atoms are under a state of tensile strain with the nearest neighbors. The hydrogen atom relieves the tensile strain, but locally replaces it with compressive strain. The increased compressive strain causes the material to become embrittled by limiting atomic mobility in the local area.

All samples cathodically-charged with hydrogen were shiny, had no oxidation products visible, and were clear of pits in the notched region. One charged sample underwent pitting during the charging process in the shaft of the sample above the submersion line (this part of the sample was not in the acid). This must have been caused by acidic vapors. The area that pitted had not been sufficiently covered with non-conductive tape. Even in this sample, the notched region was free of any localized corrosion. This sample was not used for the study.

The majority of hydrogen-charged samples of BMG-11 had very low lifetimes compared to the uncharged samples. The lifetimes of the material were decreased by as much as three orders of magnitude. The stress range versus the number of cycles to failure data is available in figure A-103. The introduction of hydrogen below the fatigue-endurance limit is extremely detrimental to the life span of a Zr-based BMG. However, there are a few interesting complications regarding the test setup and the results. Three of five samples failed outside the charged area in the shaft of the sample. These failures occurred in the half of the sample that was in epoxy and tape and submersed in the acid. A possible complication could have arisen from the method the epoxy was applied. Tape was placed before molding the samples in the epoxy to help keep the epoxy-sample interface minimized to a couple millimeters just under the notched region. Initially, the procedure was to mold the sample in the epoxy without any tape, but removing the epoxy

without hurting the sample proved to be too difficult. Removing the epoxy with the tape was easier because air was trapped near the sample surface. However, charging could have occurred to the shaft of the sample if the epoxy did not have a good interface with the sample near the notched region, and if the tape caused an air pocket. Another possibility of failure outside the notched region is that impurities or crystallinity may be more detrimental to the sample than the effects of hydrogen.

The last sample tested failed around 800,000 cycles. This trend was much longer than the rest of the samples studied. The sample also failed outside the notched region. This data point raises concern that if the sample had not failed in the shaft, an area where the effective stress is much lower than at the notch, the sample could have sustained over ten million cycles. However, this sample may have experienced a much lower current density if the sample-epoxy interface was not good. In this condition, the exposed cathodic area would drastically increase since more surface of the BMG would be in contact with the electrolyte. The galvanostat keeps a constant current. Therefore, the current density could be below 20 mA/cm^2 . The increase in exposed surface would greatly lower the atomic hydrogen produced for a given area. Therefore, the hydrogen absorbed would be reduced as well. Most samples that underwent hydrogen charging to the notched region underwent a small increase in volume, less than or equal to 4 percent. The volume change was observed by measuring the nominal diameter before and after the charging process. The last sample tested, the sample that underwent over a million cycles, did not exhibit a volume increase at the notch.

Hydrogen-charging has shown to increase the hardness of Zr-based BMGs in past studies [44,80,81,84]. Mr. Seth Lawson helped perform micro-hardness testing to

hydrogen-charged samples after failure. The results for the samples are located in table A-7 using a 500 gram load. All samples, except for one of the samples that failed in the fracture surface, were cut into transverse slices for hardness testing. The one sample not tested was lost before this could be done. The samples were tested near the outside edge, unless otherwise noted, on the cross sectional pieces. Hardness testing originally was performed on the outside surface, but the curvature of the button-head sample proved to be too difficult to take measurements. One amorphous sample as-cast was tested without cathodic charging. The average Vicker's Hardness values after five tests for this sample was 456 kg/mm^2 . Since only one specimen that failed in the notched region could be tested, this specimen was carefully tested in the shaft and the notched region of the sample for comparison to the other samples. The hardness for the shaft of this specimen was 504 kg/mm^2 , similar in value to the hardness of the as-cast specimen. The hardness of the notched region of this specimen, where failure occurred, was 591 kg/mm^2 . This value was greater than any other notch region tested. The other three samples that failed outside the notched region were tested at the notched region and at the location of failure. Hardness values were similar between the location of failure and the notched region. The average hardness for all charged samples between results for the notch and location of failure was 587 kg/mm^2 . The data suggests all samples cathodically-charged absorbed hydrogen. However, data also suggests that the three samples that had failure outside the notched region were charged along the shaft of the sample as well. Samples were also tested for hardness in the middle of the cross section. The middle should have a lower hardness value than the edge of the cross section due to diffusion. The average Vicker's hardness for the middle of the samples is 576 kg/mm^2 . This is lower than the tests

performed on the edge of the samples, but not by much. A profile from edge to center was taken for one sample. The hardness seems to be greater at the edge, quickly lowers by approximately 20 kg/mm^2 , and remains constant to the middle. This may represent that the samples are relatively well saturated with hydrogen.

The stress intensity range at failure for one of the hydrogen-charged samples that failed in the notched region was $52 \text{ MPa}\sqrt{\text{m}}$. This is larger than those samples measured in air, but only by about 5 to $10 \text{ MPa}\sqrt{\text{m}}$. The examination of the fatigue surface of the hydrogen-charged sample did not prove to show too many unusual characteristics. The crack initiation site was slightly rough, but not out of the ordinary compared to some of the samples observed in vacuum or air. Figure A-104 is a secondary electron image of the area surrounding the crack initiation site. Fatigue striations were similar in width to those samples performed in air, figure A-105. The overload fracture surface did contain an unusual surface feature that looked like a thin layer had been peeled. Figure A-106 is a secondary electron image of this feature. The overload area was slightly more smooth than most of the air samples observed. Lastly, the shear lips were noticeably larger and more defined than usual. Figure A-107 is an example of one of the shear lips. The retention of most of the morphology characteristics may be an indication of the sample continuing to be a glass with low amounts of crystallinity present. The stage of the samples life that would be most affected by the implications of hydrogen adsorption would be the initiation of a crack. This stage is difficult to examine post-fracture.

Overall, this study has shown that hydrogen is detrimental to the total life span of BMG structural components. An earlier study of a similar Zr-based BMG conducted by Suh et al. had shown hydrogen-charged samples to have lower crack growth rates than

samples not charged [44,80,81,84]. Hydrogen was shown to cause crack shielding at particular locations during the propagation of the crack. The results of the present research and the results of Suh et al. [44,80,81,84] seem to contradict one another. However, Zr-based BMGs may be sensitive to hydrogen embrittlement during crack initiation. If the majority of the samples life under the fatigue-endurance limit is spent in crack initiation, then the overall lifetime would be lowered. Hydrogen could still increase the crack propagation life of a sample. As stated in section 2.5.5, BMGs are sensitive to crack initiation. If a sufficient concentration of atomic hydrogen is produced near the surface of a BMG structural component, the absorption of hydrogen would lower the observed number of cycles to failure for BMG samples tested in hydrogen-rich environments.

4.6 Limited Fatigue Results of Varying Testing Gauge Length

The nominal stress range versus the number of cycles plot for specimen geometries A and B are presented with the test results for the radially notched specimens studied in air, figure A-108. Only three samples of each of the two geometries were tested. All samples were tested at a stress range of 977 MPa. The average number of cycles for geometry A was 11,163 cycles, and the average number of cycles to failure for geometry B was 10,447 cycles. However, the data results for both geometries were scattered, and lifetimes were lower than the radially notched specimens. Cracks initiated at the outside surface. The fracture surfaces for each of the six samples were located in the tapered section of the sample or at the transitional plane between the tapered section and the testing gauge section. This observation means failure occurred at a stress range between the nominal stress and the gross stress for the majority of samples.

The original goal of this study was to observe any effect the volume and/or surface area of the testing gauge section had on the fatigue life of Zr-based BMG components. Since BMG components are susceptible to crystallinity, porosity, scratches, and other defects, and BMGs are brittle in tensile loading; it stands to reason that increasing the testing volume/area would decrease the observed lifespan to failure of the material. The proceeding effect may have helped to explain the variation between Gilbert et al./Ritchie et al.'s results, and the results of Peter et al. and Wang et al. In this investigation, the average number-of-cycles-to-failure for both geometries were similar, leading one to believe there is very little to no effect based on testing volume and or surface area. However, failure did not occur at the plane of maximum stress for all geometry A samples and two of geometry B samples. Figure A-109 illustrates the relative position of crack initiation. The observed surface area and testing volume where cracks initiated for both geometries are relatively similar. Since all cracks initiated at the outside surface, it seems from this data that machine marks, external geometric defects, and or crystallinity located near the edge of the sample may be a more prominent issue in BMG-11 samples than the nominal stress.

4.7 Fatigue Results of Varying Surface Finish

4.7.1 Results

The Ra values, average surface deviation or commonly referred to as surface roughness, from laser profilometry and the respective grinding paper and average SiC particle sizes are provided in Table A-5. The coarsest paper resulted in the highest Ra value, and the finest paper resulted in the lowest Ra value as would be expected. Figure A-110 and A-111 are the surface roughness plotted against the SiC particle size (for

academic application) and the designate U.S. grit number (for practical application), respectively. Oddly, the designated grit number compared to the average surface roughness has a good linear relationship, but the particle size compared to the surface roughness does not.

Figure A-112 is the S-N plot for the various surface finishes. Gilbert et al.'s results for Viterloy 1 are shown as well for comparison. Obviously the surface finish or average surface roughness has a profound impact on the observed fatigue-endurance limit of bulk metallic glasses. The fatigue-endurance limit was decreased from around 900 MPa to 400 MPa when the average surface roughness went from 0.163 μm to 0.667 μm . Figure A-113 shows the reduction in the fatigue-endurance limit versus the surface roughness with a linear fit. However, the lifetime for a given surface finish at higher stress ranges was not affected. In fact, the 400 grit-finish experienced longer lifetimes at high stress ranges in general than the 1,200/P4,000 grit-finish did. Comparing the results in this study with existing data for conventional high-strength alloys is not easy since the majority of studies were conducted in the 1930s through the 1950s. One paper by Dr. Love listed reductions in fatigue-endurance limits for comparable finishes of high-strength steels [99]. Table A-6 contains the percent reduction in fatigue-endurance limit for a given steel using a comparable surface treatment, and the ultimate tensile strength. Notice, the reduction is greater for higher tensile strengths. However, the Ni-Cr-Mo steel with a higher tensile strength than BAM-11 was only reduced by 76% where BAM-11 was reduced by 71.7%. BMGs seem to be highly sensitive to surface finish with regards to fatigue-endurance limits.

4.7.2 Crack Initiation from a Critical Geometric Flaw

Round-bar specimens have proven not to be the easiest geometries for studying the evolution of a crack from the tip of a flaw. Multiple samples have been intermittently stopped during cyclic loading in order to examine for small cracks and their locations. The round surface, the small plastic deformation associated with these materials, and the large amount of time the samples are in the crack initiation development phase complicate observation of crack initiation. Post-failure round bar samples seemed to have softened around the crack initiation location. Grind marks may be seen in the area and even some fracture surfaces at the initiation run along the plane of the grind marks as seen in figure A-113. However, this does not relate the crack from starting at the base of the indentation, geometric surface flaw, where the stress concentration is highest.

In order to correct for some of these shortcomings, a three-point square beam specimen, as used in the following section, was polished using the regular P4,000/1,200 grit on each side. The sample was then refinished with the 180 grit finish perpendicular to the bending direction. This provided a polished surface to examine the cross section of the grind mark using SEM. The sample was then tested with a stress range of 1,300 MPa, moderately high in order to facilitate early crack initiation. Using three-point bending, the location of the maximum bend stress is known. Therefore, the surface in tension directly opposite of the internal pin can be monitored for any changes or the initiation of cracks. The sample was stopped at 1,000 cycles and 2,500 cycles. At 1,000 cycles, no crack was evident. At 2,500 cycles, a crack was present at nearly 0.425 mm. The secondary electron image of the crack is observed in figure A-114. At this stress range, a sample with a P4,000/1,200 finish parallel to the loading direction only sustained

approximately 4,700 cycles. This crack in less than 1,500 cycles traveled approximately 0.425 mm. If the crack started immediately after the sample was restarted at cycle 1,001, the crack growth rate would be averaged around 280 nanometers. This is only slightly larger than the striations observed on most uniaxial samples at a stress range of 900 MPa. All the above conditions suggest that the crack initiation time period is critical in the observed fatigue lifetime, even at stress ranges near 75% of the ultimate strength.

The crack did initiate from the base of a critical machine mark. In fact, there are two separate cracks initiating from the same geometric flaw. Figure A-115 is a secondary electron image of the initiation site. These two cracks later meet back up to continue as one crack. There is significant crack branching throughout propagation of the crack as can be seen in figure A-116. The branching seems to be consistently at a similar angle, between 20 and 30 degrees. As discussed in section 4.4.3, this may be associated with crack development through shear mechanisms. This study was a rare opportunity to study a crack during the propagation period before final failure. The results seem to show that BMGs are sensitive to surface flaws, cracks do initiate from geometric flaws, or stress concentrators, and the time of crack initiation will determine the overall observed fatigue lifetime.

4.8 Fatigue Results of Three- and Four-Point Bending and Comparing These With Uniaxial Results

4.8.1 General Results and Discussion

Fatigue results of three- and four-point bending are in good agreement with uniaxial radially-notched specimens. Figure A-117 is the S-N results for both the 3-point and 4-point results as compared with earlier uniaxial, button-head results performed by

Peter et al. [100,101,6,7]. All BMG-11 samples represented in this figure were made at ORNL. Morrison et al. [100] performed the majority of four-point bend tests. A few of the four-point bend tests and the three-point bend tests were performed by the author with assistance from Mr. Seth Lawson [101]. It seems the best results for either bending set-up are superior to tensile results. Slightly higher bending results versus uniaxial results are typical in crystalline materials where the maximum normal stress decreases as the crack propagates, and alignment issues with bending experiments are usually not as prevalent [102]. Also, these samples were finished with grinding marks running parallel to the tensile stress direction, unlike the uniaxial specimens where grinding marks were perpendicular to the tensile stress direction. However, the bulk of bending results line up well with the trend observed in air for the uniaxial, button-head specimens. There are samples tested in both three-point and four-point bending that exceeded a million cycles 200 MPa above the observed fatigue-endurance limit for uniaxial, button-head samples. This is a good indication of the possible confidence in the fatigue-endurance limit for BMG-11, regardless of the testing method.

Originally, a hypothesis was made that the three-point bending results would be better than the four-point bending results. The testing surface area/volume would be far less for the three-point bending than the four-point bending. Essentially a line of material is tested in the former method. In the later method, the entire area between the two pins is subjected to the maximum bending stress. Therefore, the probability of a crystal, severe surface flaw, or other impurity is far greater for the four-point bending testing method. However, this does not seem to be the case, as is seen in figure A-118. In fact, there are a greater number of four-point bend tests that achieved one million or more

cycles above 900 MPa than three-point bend tests. Furthermore, an ingot fabricated at ORNL was divided into a specimen for three-point bend testing, and a specimen for four-point bend testing at a stress range of 1,100 MPa. The four-point bend specimen performed 1,133,790 cycles, where the three-point bend specimen only performed 13,153 cycles. A preliminary study was performed to make sure the top or bottom portion of the ingot did not affect the quality of the sample. Figure A-119 shows the results. There seemed to be very little difference between the two sets of data. Inspection of the sample failing at 13,153 cycles exhibited a band of crystals near the crack initiation site. Figure A-120 is a secondary electron image of this sample's fracture surface.

The problem with the original hypothesis may lie with the frequency of distribution and size of the machine marks and crystals. All of the mentioned bend tests were very carefully polished prior to testing. Figure A-121 is a secondary electron image of the surface of a polished specimen before testing. Marks near the corner are present, but they are extremely small and infrequent. In fact, the notches in the corner of this specimen were the worst marks found the entire length of this particular beam specimen. This may indicate that the largest concern for the samples tested in this study is crystallinity. In the next subsection, the crystallinity's effect on fatigue life will further be discussed. The crystallinity distribution, or the swirl pattern seen earlier, must be common enough in most samples that three-point versus four-point plays little difference.

4.8.2 Crystallinity and Its Effect on Bend Testing of BMGs

There is considerable scatter observed in both the 4-point and 3-point bend results as high as 400 MPa above the fatigue-endurance limit [100,101]. This amount of variability was not observed in the uniaxial, button-head testing [6,7]. The variability

became even worse when samples were fabricated using a new arc-melt furnace that was still in the initial stage of being set-up at the University of Tennessee, Knoxville. The bend-test results of these ingots are indicated as UT specimens in figure A-122. The best of these samples line up with the relationship established for the button-head samples. However, a 3-point and 4-point bend specimen coming from the same ingot failed at or below a hundred cycles at a stress range of 1,100 MPa. Because of the increased variability with the new specimens made using a new furnace, an in-depth investigation of the UT fabricated samples and a good control sample made at ORNL were made. Optical metallography on etched specimens, x-ray diffraction, and the number of cycles to failure were compared. Figure A-123 shows the microstructure of each sample and where they fall on the S-N plot. All samples are shown as-cast. Figure A-124 provides the x-ray diffraction patterns in comparison with the optical resolution of the microstructures. Sample B7 failed at 105 cycles at a stress range of 1,100 MPa tested in four-point bending. B7 seems to be fully crystalline from the x-ray diffraction pattern and the microstructure. Sample B4 failed at 8,552 cycles at a stress range of 1,100 MPa tested in four-point bending. B4 is a composite of a glassy matrix and fine crystalline particles. This trend is observable from the micrograph. Small crystalline peaks are present in the amorphous halo of the x-ray diffraction pattern, but the observer has to look carefully for these peaks. Figure A-125 is a secondary electron image of the fracture surface near crack initiation. The impact of the crystals to the fatigue striations is very clear. It is not a surprise that this sample did not last longer than 8,552 cycles. The last sample, B1, was tested at 900 MPa in three point bending. This sample went ten million cycles without failure. The etching effect on the micrograph makes it difficult to see, but

there are no crystals present on the surface. A clean amorphous halo is observed in the x-ray diffraction pattern. The contrast in these results show the tremendous impact the amount of crystallinity has on the fatigue behavior. Often, x-ray diffraction (XRD) patterns are the only evidence taken as to the quality of the metallic glass sample. Though the diffractometer is a useful tool, XRD should not be the only method of determining the phases present. Figure A-126 is a secondary electron image of the fracture surface of sample T3. Crystal structures are visible through out the fatigue region. Upon closer examination of the crack initiation site, the cause of initiation is a large crystal. The x-ray diffraction pattern and an optical micrograph of this sample are shown in figure A-127. The x-ray diffraction pattern contains a relatively clean amorphous halo. One could argue the development of crystalline peaks, but it is not clear if this is background noise or crystals. The micrograph shows the emergence of small crystals in a glassy matrix. This is in line with the fatigue results. This sample failed at 9,562 cycles at a stress range of 1,100 MPa in three-point bending. Careful examination of multiple techniques is required to fully understand the nature of the material used and the resulting mechanical behaviors.

Lastly, three-point bending was attempted on fully crystalline samples of the BMG-11 composition. These samples were derived from as-cast BMG-11 ingots that were annealed at 600°C for five hours. Two samples that were to be tested failed while setting up the samples in a load frame. Between 0.11 and 0.13 kN was applied to the 3.5 mm x 3.5 mm x 30 mm samples when fracture occurred. This would make the ultimate bending stress of the crystalline material around 100 MPa. The brittle nature of BMG-11 in a crystalline form clearly shows the potential detrimental impact any crystallization

can have on the fatigue life, the fatigue-endurance limit, and the general mechanical properties. Crystallinity is a prime reason for variability in fatigue results of Zr-based BMGs.

CHAPTER 5: CONCLUSIONS

In the past, the mechanism causing the variability in fatigue-endurance limits in air has not been clear. Several key factors that could be affecting the results are the chemical composition, quality of the metallic glass, loading condition, sample preparation, and the environment. The first two factors are well related. The glassy structure of a solid is a metastable phase [103,104]. Atomic radii, heats of mixing, and the number of elements involved drastically affect the glass forming ability of any given composition [12]. Therefore, the quality of the glass formed for every individual composition should be considered. All metallic glasses contain some impurities, local atomic ordering, and localized crystallinity. However, the degree of distortion from a glassy structure is important in understanding the mechanical results. The zirconium-based crystalline structures that precipitate out of the amorphous alloy are usually brittle in nature, have low strengths, and have low fracture toughnesses [3]. With that said, one can understand the variability in fatigue endurance limits between compositions.

Wang et al. has tested Viteroloy 1, the same composition as Gilbert et al./Ritchie et al., in uniaxial tension-tension, and found the fatigue-endurance limit to be ~700 MPa [8]. Compared to Gilberts' results of 150 MPa, the same chemical composition can exhibit a wide range of fatigue-endurance limits [1,2,3,4,5,8]. Figure A-40 illustrates these results. Variation in the same composition seems to indicate that discrepancies should be linked to the loading conditions, quality of the metallic glass, and/or changes in sample preparation.

Recent studies comparing the surface finish with fatigue-endurance limits were discussed in section 4. Samples were finished with different grit papers, and the average surface finish was compared with the respective fatigue-endurance limits. The average surface finish was shown to greatly affect the results. Large machine marks or other external flaws could be a mechanism causing lower lifetimes in Gilbert et al.'s results [1,2,3,4,5]. However, Gilbert was a member of Ritchie's group which is well known for fatigue studies, and Dauskardt's group at Stanford University has recently reproduced Gilbert et al.'s results (these results have not yet been published) [1,2,3,4,5]. Also, the S-N trend for stress ranges above the fatigue endurance limit for the highest polish did not change much between finishes. Wang et al.'s lifetimes and Gilbert et al.'s lifetimes were substantially different. Therefore, external flaws may be a concern, but it is probably not the main mechanism causing the lower lifetimes and low fatigue-endurance limit of Gilbert et al.'s results [1,2,3,4,5].

Recently, Morrison and Peter have shown similar fatigue-endurance limit results for four-point bending, three-point bending, and uniaxial fatigue testing, indicating that the loading condition does not seem to be the major reason for the fatigue variability. However, these results may vary between compositions depending on the distribution of impurities and the condition of the sample surface. The change in mechanical properties, the change in precipitates, and the ease of forming a glass may be all characteristics that affect the fatigue results from one glass to another. Fabrication and testing of Viterloy 1, the same composition as used by Gilbert et al./Ritchie et al. [1,2,3,4,5], may have expedited the process of understanding low fatigue results, but this glass contains beryllium, known to have detrimental health effects, and could not have been fabricated

at ORNL or at UT. However, significant studies were conducted with BMG-11. The absence of beryllium also makes this material more enticing for commercial applications. Studying BMG-11 indicated possible discrepancies in results based on the studies recently or currently being performed.

Though the fatigue-endurance limit seems to be similar for bending and uniaxial testing, Morrison and Peter observed the increased variability in four- and three-point bending fatigue results of BMG-11 compared to the uniaxial studies performed in air for stress ranges near and slightly above the fatigue-endurance limit. However, as stated earlier, the fatigue-endurance limit seems to be equal or better in bending. The variability seems to be directly related to the quality of the glass or the amount of crystallinity per individual sample. Careful consideration should be made in testing procedures as to controlling this aspect of the material.

Much more has been understood about the effect of the testing environment. The ionization gauge was determined not to be the problem. It seems that wear from the copper pieces in the gripping system, and copper from the grips themselves are causing the low lifetimes in vacuum. This trend shows the important aspects of a stable oxide film in wear and protecting the material from environmental effects. However, other grips made from another material may correct the low vacuum results.

Hydrogen has been found to be detrimental to the overall fatigue properties. The absorption of hydrogen led to increases in the hardness of the bulk metallic glass. Little change was observed on fracture morphologies. It seems that hydrogen lowers the initiation time for a crack to form, but does not affect the crack propagation behavior.

The end result of this research was a comprehensive understanding of the fatigue properties of a Zr-Based BMG. Samples tested in air are sensitive to crystalline inclusions and the surface treatment. Stress intensity ranges were in-line with fracture toughness values. Striation spacings were slightly smaller than conventional crystalline materials, but were larger than spacings recorded by Gilbert et al. [1234] and Ritchie et al. [5]. However, these previous tests failed at low stress intensity ranges. Crystallinity may be causing the low fatigue-endurance limits and low stress intensity ranges at failure.

The research conducted in this thesis directly confronted several aspects regarding the lifetime science of BMG-11, $Zr_{52.5}Al_{10}Ti_5Cu_{17.9}Ni_{14.6}$ (at. %). Based on the experiments conducted and discussed on BMG-11, the following specific, conclusive statements can be made:

1. Amorphous BMG-11 samples were fabricated by arc melting and drop casting. The amorphous state was verified by metallography and x-ray diffraction.
2. In the 0.05 M Na_2SO_4 solution (essentially water), the amorphous BMG-11 exhibited the passive behavior at the natural corrosion potential, with a low corrosion penetration rate of approximately $1 \mu\text{m}/\text{year}$, and no susceptibility to localized corrosion [6].
3. The passive film established on amorphous BMG-11 in water is resistant to mechanical damage, immediately repassivating after removal by scratching with a diamond stylus [6].
4. Water vapor in air is not detrimental to the fatigue lifetime performance of BMG-11 at the tested relative humidity and at a cyclic frequency of 10 Hz [6,7].

5. The high fatigue-endurance limit of BMG-11 in air, 907 MPa, is approximately 50% of the ultimate tensile strength. This is comparable to conventional high-strength alloys [6,7].
6. The stress intensity range at failure and the striation spacings for a given stress intensity seem to be relatively consistent between BMG-11 samples, regardless of the total number of cycles to failure.
7. Wear from the copper grips and the copper grips themselves seem to cause lifetimes observed in vacuum to be lower than those in air. Hydrogen embrittlement via the ionization gauge is not the reason for variability in vacuum results.
8. Hydrogen is detrimental to the fatigue lifetime of Zr-Based BMGs.
9. The present bulk metallic glass studied seems to be more sensitive to surface effects than to changes in the nominal stress level as indicated in the preliminary results found in studying the effect of the gauge length of uniaxial testing on the fatigue lifetime.
10. BMGs are highly sensitive to changes in the surface roughness. The fatigue-endurance limit was reduced by 28% with a finish of 400 grit paper, and reduced by 56% with a finish of 180 grit paper.
11. BMGs seem to be more sensitive to surface finish than most conventional high-strength crystalline alloys.
12. Four- and three-point bending results of BMG-11 are equal or better than results found for the uniaxial testing of radially notched specimens. The loading condition does not seem to be the main culprit behind variability in fatigue data.

13. Crystalline impurities in BMG-11 can greatly affect the fatigue behavior with extremely low lifetimes, and changes in the observed fatigue-endurance limit.

The crystalline phases of BMG-11 have very low strengths.

14. BMG-11 could have a fatigue-endurance limit higher than realized in the present study if the testing specimens were free of defects, such as crystallinity and surface flaws.

CHAPTER 6: FUTURE RESEARCH & INTEREST

The present is an exciting time to conduct research on amorphous alloys. With larger samples, so many more experiments can be performed. Currently, research is being conducted on the atomic structure, magnetic and electrical properties, electrochemical properties, and mechanical properties throughout the world. Popular topics are nanocomposites, atomic modeling, new chemical compositions with different base elements, and increasing the plastic deformation.

As indicated in this dissertation, the quality of the glass or the amount of crystallinity in the material can significantly change the behavior and properties of the material. More work needs to be performed in the area of fabrication, and understanding the source for impurities. Varying the composition, providing more controlled processing methods, and developing models to study the heat evolution of the cooling glass are some of the possible areas of study that would aid in reproducibility of behavior in these materials. Developing procedures and compositions with greater possible thickness will increase the range of possible applications. This area of research is crucial for bulk metallic glasses to be used commercially.

The strength, hardness and other unique properties of these materials are a strong driving force for structural applications. However, most mechanical and/or structural projects require a material that has a good amount of ductility. Already a fair number of papers have been geared towards metallic glass composites. Most compositions yield brittle precipitates in good glass formers. The development of inexpensive and tough alloys is required to continue funding and interest of this area of research. Further

progress in titanium-, copper-, and iron-based bulk metallic glasses is on going. These systems show promise in providing unique properties.

Specifically related to this dissertation there are a number of future projects. Recently, small additions of elements with large atoms have led to increases in the stability of metallic glasses [105]. Fatigue behavior of these materials may prove useful. More control and consistency in the glass may result in a less variability of mechanical properties, and improved fatigue-endurance limits. Fatigue testing of other base systems may change the effect of crystalline impurities on the fatigue behavior. Some of these systems may be found to be less sensitive in regards to crack initiation.

Metallic glasses have been around for sixty years. In this time period, our knowledge of the atomic structure, the possible means of fabrication, development of corrosion resistant compositions, and the potential application of metallic glasses in structural applications has greatly improved. Plausible diameters and thicknesses of glassy materials have gone from around fifty micrometers to a few centimeters. The need for low to no finish products and the use of high pressure injection molding into net shapes could possibly drive the science behind metallic glasses. The next sixty years should be equally as exciting.

REFERENCES

-
1. CJ Gilbert, V Schroeder, and RO Ritchie. Fracture and Fatigue in a Zr-Based Bulk Metallic Glass. Bulk Metallic Glasses; WL Johnson, A Inoue, and CT Liu, Ed. Materials Research Society Proceedings. Vol 554, 1999, pp. 343-354.
 2. CJ Gilbert, V Schroeder, and RO Ritchie. Mechanisms for Fracture and Fatigue-Crack Propagation in a Bulk Metallic Glass. Metallurgical and Materials Transactions,A. Vol 30A, 1999, pp. 1739-1753.
 3. CJ Gilbert, RO Ritchie, WL Johnson. Fracture Toughness and Fatigue –Crack Propagation in a Zr-Ti-Ni-Cu-Be Bulk Metallic Glass. Applied Physical.Letters. Vol 71 (No. 4), 1997, pp. 476-478.
 4. CJ Gilbert, JM Lippmann, RO Ritchie. Fatigue of a Zr-Ti-Cu-Ni-Be Bulk Amorphous Metal: Stress/Life and Crack-Growth Behavior. Scripta Materialia. Vol 38, 1998, pp. 537-542.
 5. RO Ritchie, V Schroeder, CJ Gilbert. Fracture, Fatigue and Environmentally-Assisted Failure of a Zr-Based Bulk Amorphous Metal. Intermetallics. Vol 8, 2000, pp. 469-475.
 6. WH Peter, RA Buchanan, CT Liu, PK Liaw. The Fatigue Behavior of a Zirconium-Based Bulk Metallic Glass in Vacuum and Air. Journal of Non-Crystalline Solids. Vol 317, 2003, pp. 187-192.
 7. WH Peter, PK Liaw, RA Buchanan, CT Liu, CR Brooks, JA Horton, Jr, CA Carmichael, Jr, and JL Wright. Fatigue Behavior of Zr_{52.5}Al₁₀Ti₅Cu_{17.9}Ni_{14.6} Bulk Metallic Glass. Intermetallics. Vol 10, 2002, pp. 1125-1130.

-
8. GY Wang, PK Liaw, A Peker, B Yang, ML Benson, W Yuan, WH Peter, L Huang, M Freels, RA Buchanan, CT Liu, CR Brooks. Fatigue Behavior of Zr-Ti-Ni-Cu-Be Bulk Metallic Glasses. Intermetallics. Vol 13, 2005, pp. 429-435.
 9. GY Wang, PK Liaw, WH Peter, B Yang, M Freels, Y Yokoyama, ML Benson, BA Green, TA Saleh, RL McDaniels, RV Steward, RA Buchanan,, CT Liu, CR Brooks. Fatigue Behavior and Fracture Morphology of Zr50Al10Cu40 and Zr50Al10Cu30Ni10 Bulk-Metallic Glasses. Intermetallics. Vol 12, 2004, pp. 1219-1227.
 10. GY Wang, PK Liaw, WH Peter, B Yang, Y Yokoyama, ML Benson, BA Green, MJ Kirkham, SA White, TA Saleh, RL McDaniels, RV Steward, RA Buchanan, CT Liu, CR Brooks. Fatigue Behavior of Bulk-Metallic Glasses. Intermetallics. Vol 12, 2004, pp. 1219-1227.
 11. A Inoue. Mechanical Properties of Zr-based Glassy Alloys Containing Nanoscale Compound Particles. Intermetallics. Vol 8, 2000, pp. 469-475.
 12. A Inoue. Bulk Amorphous Alloys. Amorphous and Nano-Crystalline Materials: Preparation, Properties, and Applications; A Inoue, K Hashimoto, Eds. Springer; Heidelberg, Germany; 2001, pp. 1-51.
 13. FE Luborsky. Amorphous Metallic Alloys. Amorphous Metallic Alloys; FE Luborsky, Ed. Butterworth & Co. Ltd; London; 1983, pp. 1-7.
 14. R Boil, HR Hilzinger, and H Warlimont. Magnetic Material Properties and Applications of Metallic Glasses in Electronic Devices. Glassy Metals: Magnetic, Chemical, and Structural Properties; R Hasegawa, Ed. CRC Press, Inc.; Boca Raton, Florida; 1983, pp. 183-202.

-
15. P Duwez. Foreword. Metallic Glasses: Papers Presented at a Seminar of the Materials Science Division of the American Society for Metals September 18 and 19, 1976. American Society for Metals; Metals Park, Ohio; 1978, pp. iii-v.
16. CT Liu, L Heatherly, DS Easton, CA Carmichael, JH Schneibel, CH Chen, JL Wright, MH Yoo, JA Horton, and A Inoue. Test Environments and Mechanical Properties of Zr-Base Bulk Amorphous Alloys. Metallurgical and Materials Transactions A. Vol 29A, 1998, pp. 1811-1820.
17. R.D. Conner, R.B. Dandliker, W.L. Johnson, Acta Materialia. Vol 46, 1998, pp. 6089–6102.
18. K Amiya, A Urata, N Nishiyama, A Inoue. Fe-B-Si-Nb Bulk Metallic Glasses with High Strength Above 4000 MPa and Distinct Plastic Elongation. Materials Transactions. Vol 45 (No. 4), 2004, pp. 1214-1218.
19. K Hashimoto and T Masumoto. Corrosion Properties of Amorphous Alloys. Glassy Metals: Magnetic, Chemical, and Structural Properties; R Hasegawa, Ed. CRC Press, Inc.; Boca Raton, Florida; 1983, pp. 235-262.
20. K Hashimoto. Chemical Properties. Amorphous Metallic Alloys; FE Luborsky, Ed. Butterworth & Co. Ltd; London; 1983, pp. 471-486.
21. A Inoue. Amorphous and Nano-crystalline Materials: Preparation, Properties, and Applications. A Inoue and K. Hashimoto, Eds. Springer, Tokyo, 2001. p.20
22. RD Conner, AJ Rosakis, WL Johnson, DM Owen. Fracture Toughness Determination for a Beryllium-Bearing Bulk Metallic Glass, Scripta Materialia. Vol 37, 1997, pp.1373-1378.

-
23. E Fleury, SM Lee, HS Ahn, WT Kim, DH Kim. Tribological Properties of Bulk Metallic Glasses. Materials Science and Engineering A. Vol 375–377, 2004, pp. 276–279.
24. MZ Ma, RP Liu, Y Xiao, DC Lou, L Liu, Q Wang, WK Wang. Wear Resistance of Zr-Based Bulk Metallic Glass Applied in Bearing Rollers. Materials Science and Engineering A. Vol 386, 2004, pp. 326–330.
25. LA Davis. Strength, Ductility and Toughness. Metallic Glasses: Papers Presented at a Seminar of the Materials Science Division of the American Society for Metals September 18 and 19, 1976. American Society for Metals; Metals Park, Ohio; 1978, pp. 190-223.
26. DE Polk and BC Giessen. Overview of Principles and Applications. Metallic Glasses: Papers Presented at a Seminar of the Materials Science Division of the American Society for Metals September 18 and 19, 1976. American Society for Metals; Metals Park, Ohio; 1978, pp. 1-35.
27. HS Chen. Metallic Glasses. Materials Science and Engineering. Vol 25, 1976, pp. 59-69.
28. HS Chen. The Influence of Structural Relaxation on the Density and Young's Modulus of Metallic Glasses. Journal of Applied Physics. Vol 49, 1978, pp. 3289-3291.
29. HH Liebermann. Sample Preparation: Methods and Process Characterization. Amorphous Metallic Alloys; FE Luborsky, Ed. Butterworth & Co. Ltd; London; 1983, pp. 26-41.
30. T Egami. Atomic Short-Range Ordering in Amorphous Metal Alloys. Amorphous Metallic Alloys; FE Luborsky, Ed. Butterworth & Co. Ltd; London; 1983, pp. 100-112.

-
31. DB Miracle. On the Universal Model for Medium-Range Order in Amorphous Metal Structures. Journal of Non-Crystalline Solids. Vol 317, 2003, pp 40-44.
32. N Mattern, U Kuhn, H Hermann, H Ehrenberg, J Neuefeind, J Eckert. Short-Range Order of $Zr_{62-x}Ti_xAl_{10}Cu_{20}Ni_8$ Bulk Metallic Glasses. Acta Materialia. Vol 50, 2002, pp.305-314.
33. DB Miracle. A Structural Model for Metallic Glasses. Nature Materials. Vol 3, 2004, pp. 697-702.
34. DB Miracle, ON Senkov. Atomic Size Distribution Plots for the Structure of Amorphous Metals. Proceedings of the 4th Pacific Rim International Conference on Advanced Materials and Processing. Materials Transactions. Vol 2, 2001, pp. 2893-2896.
35. WL Johnson. Metallic Glasses. ASM Handbook. ASM; Metal Park, OH; Vol. 2: Properties and Selections: Nonferrous Alloys and Special Purpose Materials, 1990, pp. 804-821.
36. PJ Steinhardt, DR Nelson, and M Ronchetti. Physical Review Letters. Vol 47, 1981, p. 1297.
37. S Sachdev and DR Nelson. Physical Review Letters. Vol 53, 1984, p. 1947.
38. J Dixmier, JF Sadoc. Structural Models. Metallic Glasses: Papers Presented at a Seminar of the Materials Science Division of the American Society for Metals September 18 and 19, 1976. American Society for Metals; Metals Park, Ohio; 1978, pp. 97-113.
39. JL Finney. Modelling the Atomic Structure. Amorphous Metallic Alloys; FE Luborsky, Ed. Butterworth & Co. Ltd; London; 1983, pp. 42-57.
40. TC Hufnagel. Finding Order in Disorder. Nature Materials. Vol 3, 2004, pp. 666-667.

-
41. KM Flores, D Suh, RH Dauskardt, P Asoka-Kumar, PA Sterne, RH Howell. Characterization of Free Volume in a Bulk Metallic Glass Using Positron Annihilation Spectroscopy. Journal of Materials Research. Vol 17 (No. 5), 2002, pp. 1153-1161.
42. LC Damonte. Nuclear Techniques Characterization of Short-Range Order in Zr-TM-Cu-Al-Ni (TM=Hf, Ti, Fe) Bulk Metallic Glasses. Annales de Chimie Science des Materiaux. Vol 27 (No. 5), 2002, pp. 61-67.
43. P. Asoka-Kumar, J Hartley, R Howell, PA Sterne, TG Nieh. Chemical Ordering Around Open-Volume Regions in Bulk Metallic Glass Zr_{52.5}Ti₅Al₁₀Cu_{17.9}Ni_{14.6}. Applied Physics Letters. Vol 77 (No. 13), 2000, pp. 1973-1975.
- 44 D Suh and RH Dauskardt. Effects of Open-Volume Regions on Relaxation Time Scales and Fracture Behavior of a Zr-Ti-Ni-Cu-Be Bulk Metallic Glass. Journal of Non-Crystalline Solids. Vol 317, 2003, pp 181-186.
45. MK Miller, TD Shen, RB Schwarz. Atom Probe Studies of Metallic Glasses. Journal of Non-Crystalline Solids. Vol 317, 2003, pp 10-16.
46. HA Davies. Metallic Glass Formation. Amorphous Metallic Alloys; FE Luborsky, Ed. Butterworth & Co. Ltd; London; 1983, pp. 8-25.
47. W Smith. Principles of Materials Science and Engineering, 2nd Edition. McGraw-Hill Publishing Company; New York; 1990, pp. 19-67.
48. A Bienenstock. Structural Studies of Amorphous Materials. Physical Properties of Amorphous Materials. D Adler, BB Schwartz, and MC Steele, Ed. Plenum Press; New York; 1985, pp. 177-178.

-
49. MG Scott. Crystallization. Amorphous Metallic Alloys; FE Luborsky, Ed. Butterworth & Co. Ltd; London; 1983, pp. 142-168.
50. JR Fried. Polymer Science and Technology. 2nd Edition, Prentice Hall Professional Technical Reference, Upper Saddle River, NJ, 2003. pp. 156-157
51. ZP Lu, CT Liu. A New Glass-Forming Ability Criterion for Bulk Metallic Glasses. Acta Materialia. Vol 50, 2002, pp. 3501-3512.
52. CT Liu, MF Chishom, MK Miller. Oxygen Impurity and Microalloying Effect in a Zr-Based Bulk Metallic Glass Alloy. Intermetallics. Vol 10, 2002, pp. 1105-1112.
53. J Mencik. Strength and Fracture of Glass and Ceramics. Elsevier Science Ltd; Oxford, UK; 1992.
54. R Hertzberg. Deformation and Fracture Mechanics of Engineering Materials, 3rd ed. John Wiley & Sons; New York; 1989.
55. WH Peter, RA Buchanan, CT Liu, PK Liaw, ML Morrison, JA Horton, CA Carmichael, Jr., and JL Wright. Localized Corrosion Behavior of a Zirconium-Based Bulk Metallic Glass Relative to Its Crystalline State. Intermetallics. Vol 10, 2002, pp. 1125-1130.
56. M Naka, K Hashimoto, and T Masumoto. Corrosion Behavior of Amorphous and Crystalline Cu₅₀Ti₅₀ and Cu₅₀Zr₅₀ Alloys. Journal of Non-Crystalline Solids. Vol 30, 1978, p. 29.
57. Metals Handbook, 9th Edition. ASM International; Metals Park, Ohio; Volume 13: Corrosion, 1987, pp. 669-721.

-
58. V Schroeder, CJ Gilbert, and RO Ritchie. Comparison of the Corrosion Behavior of a Bulk Amorphous Metal, $Zr_{41.2}Ti_{13.8}Cu_{12.5}Ni_{10}Be_{22.5}$, with its Crystallized Form. Scripta Materialia. Vol38 (No.10), 1998, pp.1481-1485.
59. A Pecker and WL Johnson. A Highly Processable Metallic Glass. Applied Physics Letter. Vol 63, 1993, pp. 2342-2344.
60. XH Lin and WL Johnson. Formation of Ti-Zr-Cu-Ni Bulk Metallic Glasses. Journal of Applied Physics. Vol 78, 1995, pp. 6514-6519.
61. WH Peter, RA Buchanan, CT Liu, PK Liaw, ML Morrison, JA Horton, CA Carmichael, Jr., and JL Wright. Localized Corrosion Behavior of a Zirconium-Based Bulk Metallic Glass Relative to Its Crystalline State. Intermetallics. Vol 10, 2002, pp. 1125-1130.
62. NE Dowling. Mechanical Behavior of Materials: Engineering Methods of Deformation, Fracture, and Fatigue, 2nd Edition; Prentice Hall; Upper Saddle River, New Jersey; 1999, p. 655.
63. F. Spaepen. A Microscopic Mechanism for Steady State Inhomogeneous Flow in Metallic Glass. Acta Metallurgica. Vol 25, 1977, pp. 407-415.
64. TG Nieh, C Schuh, J Wadsworth, Y Li. Strain Rate-Dependent Deformation in Bulk Metallic Glasses. Intermetallics. Vol 10, 2002, pp. 1177-1182.
65. TG Nieh, T Mukai, CT Liu, J Wadsworth. Superplastic Behavior of a Zr-10Al-5Ti-17.9Cu-14.6Ni Metallic Glass in the Supercooled Liquid Region. Scripta Materialia. Vol 40, 1999, pp. 1021-1027.

-
66. TG Nieh, J Wadsworth, CT Liu, T Ohkubo, Y Hirotsu. Plasticity and Structural Instability in a Bulk Metallic Glass Deformed in the Supercooled Liquid Region. Acta Materialia. Vol 49, 2001, pp.2887-2896.
67. Y Kawamura, T Shibata, A Inoue, T Masumoto. Superplastic Deformation of $Zr_{65}Al_{10}Ni_{10}Cu_{15}$ Metallic Glass. Scripta Materialia. Vol 37 (No. 4), 1997, pp. 431-436.
68. AS Argon. Plastic Deformation in Metallic Glasses. Acta Metallurgica. Vol 27, 1979, pp. 47-58.
69. CA Pampillo. Localized Shear Deformation in a Glassy Metal. Scripta Metallurgica. Vol 6, 1972, pp.915-918.
70. T Masumoto, R Maddin. The Mechanical Properties of Palladium 20 at/o Silicon Alloy Quenched from the Liquid State. Acta Metallurgica. Vol 19, 1971, pp. 725-741.
71. E Ustundag, B Clausen, JC Hanan, MAM Bourke, A Winholtz, and A Peker. Residual Stresses in Bulk Metallic Glasses Due to Differential Cooling or Thermal Tempering. Bulk Metallic Glasses; WL Johnson, A Inoue, and CT Liu, Ed. Materials Research Society Proceedings. Vol 554, 1999, pp. 343-354.
- 72 WJ Wright, R Saha, and WD Nix. Deformation Mechanisms of the $Zr_{40}Ti_{14}Ni_{10}Cu_{12}Be_{24}$ Bulk Metallic Glass. Japan Institute of Metals. Vol 42 (No. 4), 2001, pp. 642-649.
- 73 R. Huang, Z Suo, JH Prevost, and WD Nix. Inhomogeneous Deformation in Metallic Glasses. Journal of the Mechanics and Physics of Solids. Vol 50, 2002, pp 1011-1027.

-
74. HA Bruck, T Christman, AF Rosakis, WL Johnson. Quasi-static Constitutive Behavior of $Zr_{41.25}Ti_{13.75}Ni_{10}Cu_{12.5}Be_{22.5}$ Bulk Amorphous Alloys. Scripta Metallurgica. Materialia. Vol 30, 1994, pp.429-434.
75. KM Flores, RH Dauskardt. Crack-Tip Plasticity in Bulk Metallic Glasses. Materials Science and Engineering A. Vol 319-321, 2001, pp. 511-515.
76. J Li, ZL Wang, and TC Hufnagel. Characterization of Nanometer-Scale Defects in Metallic Glasses By Quantitative High-Resolution Transmission Electron Microscopy. Physical Review B. Vol 65, 2002, pp 144201-1–144201-6.
77. J Li, F Spaepen, and TC Hufnagel. Nanometre-Scale Defects in Shear Bands in a Metallic Glass. Philosophical Magazine A. Vol 82 (No. 13), 2002, pp 26623-2630.
78. JJ Kim, Y Choi, S Suresh, AS Argon. Nanocrystallization During Nanoindentation of a Bulk Amorphous Metal Alloy at Room Temperature. Science. Vol 295, 2002, pp. 654-657.
79. CJ Gilbert, JW Ager III, V Schroeder, RO Ritchie, JP Lloyd, and JR Graham. Light Emission During Fracture of a Zr–Ti–Ni–Cu–Be Bulk Metallic Glass. Applied Physics Letters. Vol 74 (No. 25), 1999, pp. 3809-3811.
80. D Suh, RH Dauskardt. Hydrogen Effects on the Mechanical and Fracture Behavior of Zr-Ti-Ni-Cu-Be Bulk Metallic Glass. Scripta Materialia. Vol 42, 2000, pp.233-240.
81. D Suh, P Asoka-Kumar, RH Dauskardt. The Effects of Hydrogen on Viscoelastic Relaxation in Zr-Ti-Ni-Cu-Be Bulk Metallic Glasses: Implications for Hydrogen Embrittlement. Acta Materialia. Vol 50, 2002, pp. 537-551.

-
82. LA Davis. Strength, Ductility and Toughness. Metallic Glasses: Papers Presented at a Seminar of the Materials Science Division of the American Society for Metals September 18 and 19, 1976. American Society for Metals; Metals Park, Ohio; 1978, pp. 190-223.
83. Structural Alloys Handbook. Mechanical Properties Data Center; Traverse City, MI; 1977.
84. D Suh, RH Dauskardt. The Effects of Hydrogen on Deformation and Fracture of a Zr-Ti-Ni-Cu-Be Bulk Metallic Glass. Materials Science and Engineering A. Vol 319-321, 2001, pp. 480-483.
85. AK Kuruvilla. Amptiac: Life Prediction and Performance Assurance of Structural Materials in Corrosive Environments. IIT Research Institute, 1999, pp. 3-4.
86. EE Stansbury and RA Buchanan. Fundamentals of Electrochemical Corrosion. ASM International; Materials Park, Ohio; 2000, pp. 87-450.
87. A Pecker and WL Johnson. A Highly Processable Metallic Glass. Applied Physics Letter. Vol 63, 1993, pp. 2342-2344.
88. XH Lin and WL Johnson. Formation of Ti-Zr-Cu-Ni Bulk Metallic Glasses. Journal of Applied Physics. Vol 78, 1995, pp. 6514-6519.
89. AR Yavari, A Inoue, T Zhang, WJ Botta F., A Kvik. Metastable Phases, Quasicrystals, and Solid, Solutions in Zr-Based Bulk Glass-Forming Alloys. Scripta Materialia. Vol 44, 2001, pp. 1239-1244.
90. T Zhai, YG Xu, JW Martin, AJ Wilkinson, GAD Briggs. A Self-Aligning Four-Point Bend Testing Rig and Sample Geometry Effect in Four-Point Bend Fatigue. International Journal of Fatigue. Vol 21, 1999, pp. 889-894.

-
91. C Brooks and BL McGill. The Application of Scanning Electron Microscopy to Fractography. Materials Characterization. Elsevier Science Ltd; New York, NY; 1994, p. 195.
92. ASME Handbook. Metals Engineering – Design. McGraw-Hill; New York; 1953.
93. EP George and CT Liu. Mechanical Properties of Ni₃Al and FeAl: Recent Developments. Structural Intermetallics 1997; MV Nathal, R Darolia, CT Liu, PL Martin, DB Miracle, R Wagner, and M Yamaguchi, Ed. The Minerals, Metals, and Materials Society; Warrendale, Pennsylvania; 1997, pp. 693-702.
94. JW Cohron, EP George, L Heatherly, CT Liu, and RH Zee. Effect of Low-Pressure Hydrogen on the Room-Temperature Tensile Ductility and Fracture Behavior of Ni₃Al Intermetallics. Vol 4, 1996, pp. 497-502.
95. RJ McElroy, TJ Williams, FMD Boydon, B Hemsworth. Low Temperature Embrittlement of LWR RPV Support Structures. International Journal of Pressure Vessels and Piping. Vol 54 (No.1-2), 1993, pp. 171-211.
96. RC Bates, WG Clark. Fractography and Fracture Mechanics. Transactions Quarterly for the American Society of Metals, Vol 62 (No. 2), 1969, p. 380.
97. RH Dauskardt, MR James, JR Porter, RO Ritchie. Cyclic Fatigue-Crack Growth in a SiC-Whisker-Reinforced Alumina Ceramic Composite - Long-Crack and Small-Crack Behavior. Journal of the American Ceramic Society. Vol 75, 1992, pp. 759-771.
98. A Gebert, N Ismail, U Wolff, M Uhlemann, J Eckert, L Schultz. Effects of Electrochemical Hydrogenation of Zr-based alloys with High Glass-Forming Ability. Intermetallics. Vol 10, 2002, pp. 1207–1213.

-
99. RJ Love. "The Influence of Surface Condition on the Fatigue Strength of Steel", Properties of Metallic Surfaces, The Institute of Metals, London, 1953, pp. 161.
100. ML Morrison, WH Peter, GY Wang, PK Liaw, RA Buchanan, CT Liu.
Unpublished Data.
101. WH Peter, S Lawson, ML Morrison, GY Wang, PK Liaw, RA Buchanan, CT Liu.
Unpublished Data.
102. TJ Dolan. Method of Testing. ASME Handbook: Metals Engineering-Design. OJ Horger, Ed. McGraw-Hill Book Company, New York, NY, 1965, pp.199-207.
103. D Turnbull. Undercooled Alloy Phases. EW Collings, CC Koch (Eds.); The Metallurgical Society, Warrendale, PA, 1987, p. 3.
104. Dirk Holland-Moritz, Short-range order and solid-liquid interfaces in undercooled metallic melts, Materials Science and Engineering A. Vol 304-306, 2001, pp. 108-113.
105. CT Liu, ZP Lu. Effect of Minor Alloying Additions on Glass Formation in Bulk Metallic Glasses. Intermetallics. Vol 13 (No.3-4), 2005, pp.415-418.

APPENDIX

Table A-1: Polarization Curve Properties for Amorphous and Crystalline BMG-11 Tested in 0.6 M NaCl.

		Sample	Trial	E_{corr} mV (SCE)	E_{pit} mV (SCE)	E_{pp} mV (SCE)	i_{corr} (A/cm ²)
Amorphous	Polished (0.5 μ m), Etched	1	1	-304	1230	<-388	1.5x10 ⁻⁸
			2	-300	660	-265	1.4x10 ⁻⁸
			3	-252	N/A	N/A	4.6x10 ⁻⁷
			4	-242	N/A	N/A	2.1x10 ⁻⁹
		2	1	-252	950	-252	1.2x10 ⁻⁶
			2	-257	125	-205	4.1x10 ⁻⁹
			3	-182	180	-252	1.8x10 ⁻⁸
		Ave	--	-256	449	-272	2.4x10 ⁻⁷
		Polished (0.5 μ m), No Etch	1	1	-195	-30	-210
	2			-162	-86	-210	7.1x10 ⁻⁸
	2		1	-210	-110	-200	2.3x10 ⁻⁶
	Ave		--	-189	-75	-207	8.0x10 ⁻⁷
	600 SiC Grit (14.5 μ m), No Etch	1	1	-228	175	-215	2.0x10 ⁻⁷
			2	-275	-29	N/A	1.2x10 ⁻⁷
		2	1	-287	-100	-200	5.5x10 ⁻⁸
2			-255	110	-208	9.3x10 ⁻⁸	
Ave		--	-261	39	-208	1.2x10 ⁻⁷	
Crystalline		Polished (0.5 μ m), Etched	1	1	-330	37	-375
	2			<-290	-109	<-290	4.9x10 ⁻⁷
	2		1	-198	-126	-343	4.6x10 ⁻⁷
			2	-198	-126	-343	4.6x10 ⁻⁷
	3		1	-260	N/A	N/A	2.2x10 ⁻⁸
			2	-233	-193	<-300	2.4x10 ⁻⁵
			3	-333	N/A	N/A	3.2x10 ⁻⁷
	Ave	--	-274	-98	-327	4.3x10 ⁻⁶	
	Polished (0.5 μ m), No Etch	2	1	-248	-128	<-320	2.7x10 ⁻⁶
			2	-220	-155	<-320	2.4x10 ⁻⁷
			3	-182	-182	<-320	1.1x10 ⁻⁶
		Ave	--	-217	-155	<-320	1.3x10 ⁻⁶
	600 SiC Grit (14.5 μ m), No Etch	2	1	-310	15	<-380	8.1x10 ⁻⁸
			2	-260	30	<-320	3.3x10 ⁻⁸
		3	1	-225	90	<-320	7.9x10 ⁻⁸
			2	-270	-22	<-320	2.5x10 ⁻⁸
		Ave	--	-266	28	<-320	5.5x10 ⁻⁸

Table A-2: BMG-11 Element Amounts.

Element	Atomic Percent (%)	Weight Percent (%)	Mass (g)
Zirconium (99.5 wt % Zr)	52.5	65.6673	11.82
Copper (99.99 wt % Cu)	17.9	15.5955	2.81
Nickel (99.99 wt % Ni)	14.6	11.7534	2.12
Titanium (<550 ppm oxygen, <110 ppm carbon)	5.0	3.2840	0.59
Aluminum (99.99 wt % Al)	10.0	3.6997	0.67
Total	100.0	100.0000	18.00

Table A-3: Crystallization Temperature for Variations of BMG-11 with Additions of Pd.

Pd Atomic Composition	Crystallization Temperature (Degrees Kelvin)
Pd ₀	742.2
Pd _{2.5}	735.0
Pd ₅	732.4
Pd _{7.5}	745.5
Pd ₁₀	745.9

Table A-4: Polarization Curve Properties for Amorphous BMG-11 Tested in 0.05 M Na₂SO₄.

Sample	Trial	E _{corr} mV (SCE)	E _{pit} mV (SCE)	E _{pp} mV (SCE)	i _{corr} (A/cm ²)
1	1	-110	None	None	6.4 x 10 ⁻⁸
2	1	-110	None	None	2.8 x 10 ⁻⁸
	2	-166	N/A	N/A	2.3 x 10 ⁻⁸

Table A-5: U.S. Grit Number Convention Versus Surface Roughness for BAM-11.

Paper Grit Number, U. S. Convention	SiC Particle Size (μm)	Ra (μm)
1200 (P4000)	5	0.163
400	22	0.552
180	78	0.667

Table A-6: Reduction of Fatigue Endurance Limit for Conventional, High-Strength Steels and BAM-11.

Material	P4000 (1200) Grit or Highly Polished, %*	400 Grit or 00 Emery Cloth, %*	Ultimate Tensile Strength (MPa)
S.A.E. 1045 (0.45% C) Steel [99]	100	100	~600
0.49% C Steel [99]	100	94	~600
B.S. 4S11 Steel [99]	100	100	775
Ni-Cr (0.32% C, 3.5% Ni, 0.75% Cr) [99]	100	94	1,627
Ni-Cr-Mo (0.41% C, 2.53% Ni 0.63% Cr, 0.63% Mo) [99]	100	76	1,903
Zr _{52.5} Al ₁₀ Ti ₅ Cu _{17.9} Ni _{14.6} , BAM-11	100	71.7	1,750
* Percentages are Based on Fatigue-Endurance Limit of Polished Sample.			

Table A-7: Hardness of Hydrogen-Charged BAM-11 Button-Head Samples.

Sample	N _r (Cycles)	Location	Shoulder Hardness, VH (kg/mm ²)		Notch Hardness, VH (kg/mm ²)	
			Edge	Middle	Edge	Middle
As-Cast	N/A	N/A	456	456	456	456
17	30,809	Shoulder	577	592	586	562
2	38,079	Shoulder	598	615	582	549
18	59,641	Notch	504	516	591	578
16	63,153	Notch	N/A	N/A	N/A	N/A
6	822,853	Shoulder	593	575	606	561

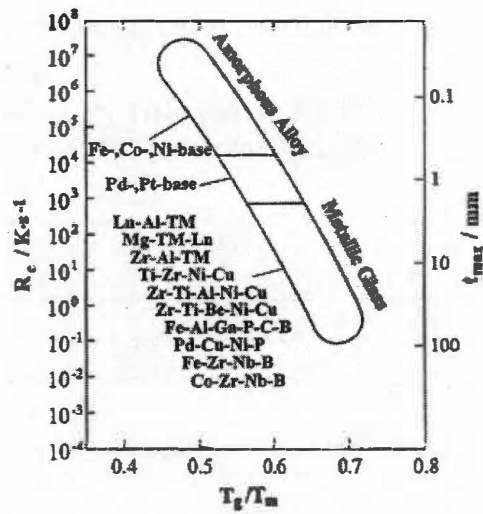


Figure A-1: Relationship of Glass Transition Temperature, with Cooling Rates, and Sample Thickness. Reprinted from *Intermetallics*, Volume 8, A. Inoue, Mechanical Properties of Zr-based Glassy Alloys Containing Nanoscale Compound Particles, pp. 469-475, 2000, with Permission from Elsevier.

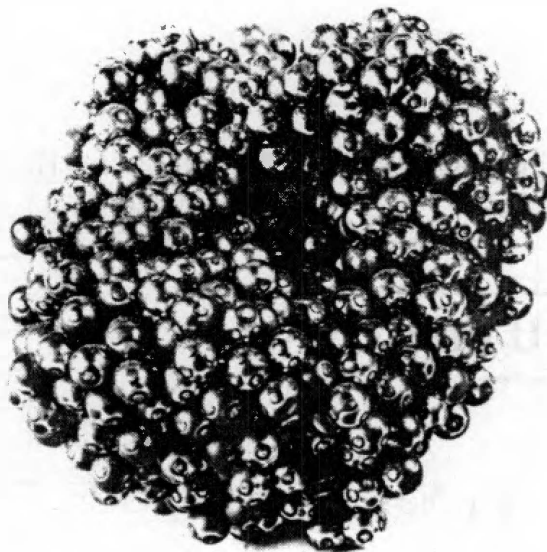


Figure A-2: Bernal's Steel Ball Model. Reprinted from *Amorphous Metallic Alloys*, L. Finney, Modeling the Atomic Structure, pp. 42-57, 1983, with Permission from Elsevier.

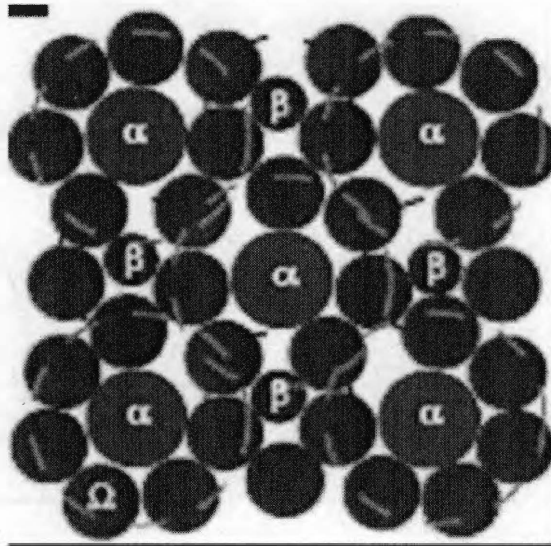


Figure A-3: A Two-Dimensional Representation of a Dense Cluster-Packing Structure. Zr Solvent Spheres Form Relaxed Icosahedra Around Each α Solute. Reprinted from *Nature Materials*, Volume 3, D.B. Miracle, A Structural Model for Metallic Glasses, pp. 677-702, 2004, with Permission from Nature Publishing Group.

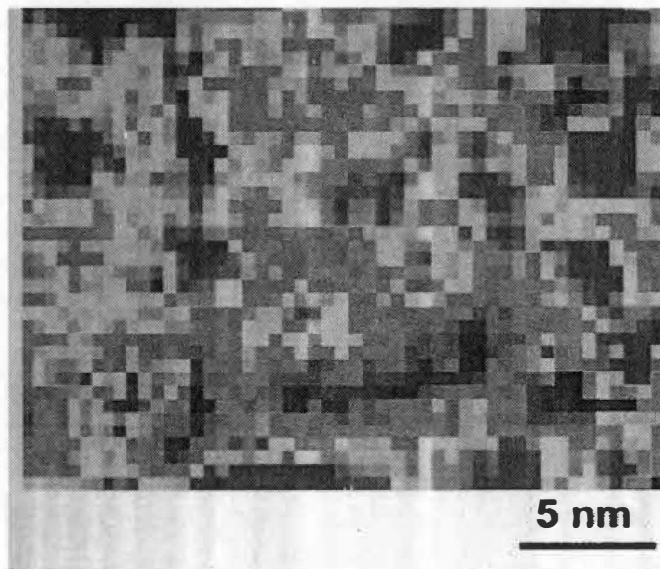


Figure A-4: Two Dimensional Concentration Map of Pd-Based BMG. Reprinted from *Journal of Non-Crystalline Solids*, Volume 317, M.K. Miller et al., Atom Probe Studies of Metallic Glasses, pp. 10-16, 2003, with Permission from Elsevier.

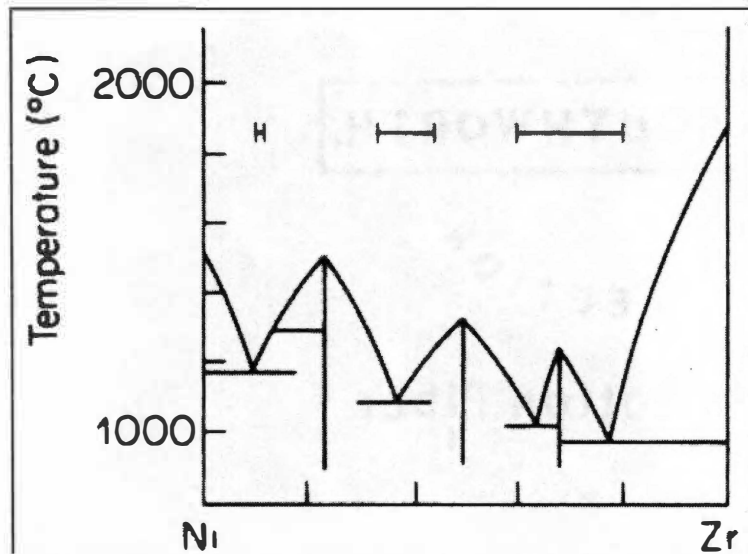


Figure A-5: Phase Diagram of Zirconium-Nickel with Glass Forming Ranges Identified. Reprinted from Amorphous Metallic Alloys, H.A. Davies, Metallic Glass Formation, pp. 8-25, 1983, with Permission from Elsevier.

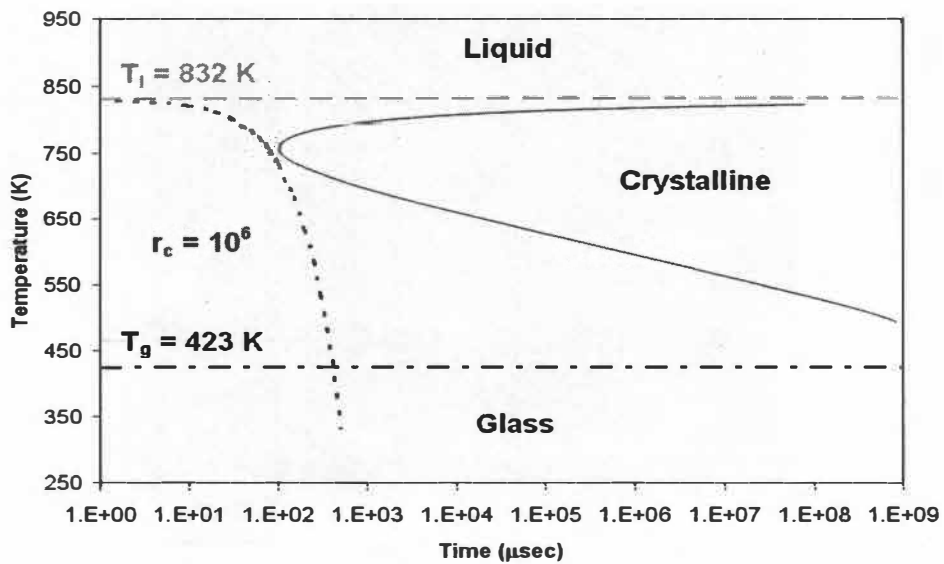


Figure A-6: TTT Diagram Illustrating the Glass Transition Temperature, the Liquidus Temperature, and the Critical Cooling Rate.

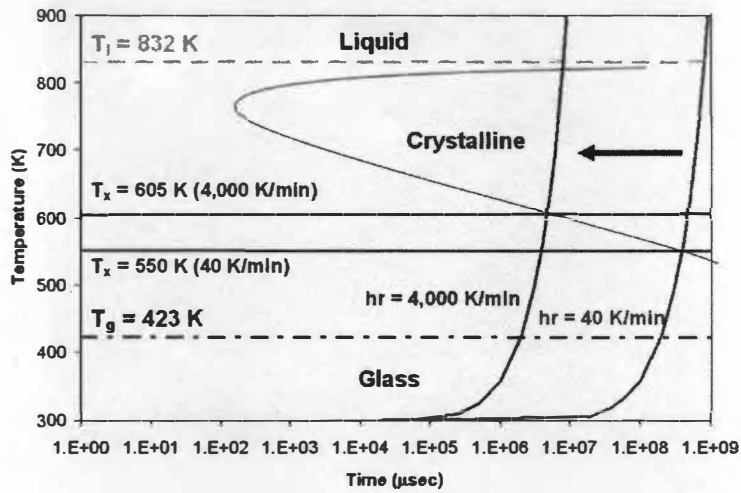


Figure A-7: TTT Diagram Illustrating Various Heating Rates on the Crystallization Temperature of a Metallic Glass.

FABRICATION METHODS OF METALLIC GLASS PRIOR TO 1990	
Deposition Methods	Chemical Electro Spray
Sputtering and Evaporation	
Ion Implantation	
Powder Fabrication	Gas Atomization Gas-Water Atomization Centrifugal Atomization Spark Erosion
Splat Quenching	
Drop Melt Methods	Filaments – short sections, circular orifice Ribbons – continuous, circular orifice Tapes – continuous, slit orifice

Figure A-8: Many of the Possible Fabrication Methods Prior to 1990 [29].

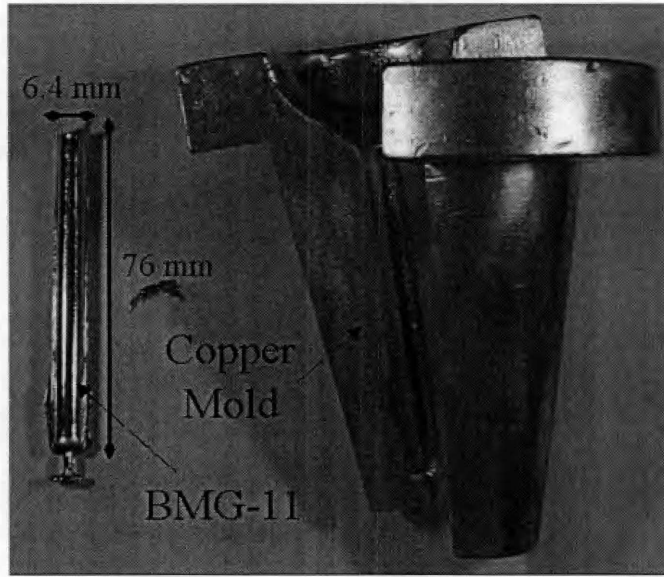


Figure A-9: As-Cast 6.4 mm Diameter Specimen of BMG-11 ($Zr_{52.5}Al_{10}Ti_5Cu_{17.9}Ni_{14.6}$, at. %) and the Mold Used for Casting.

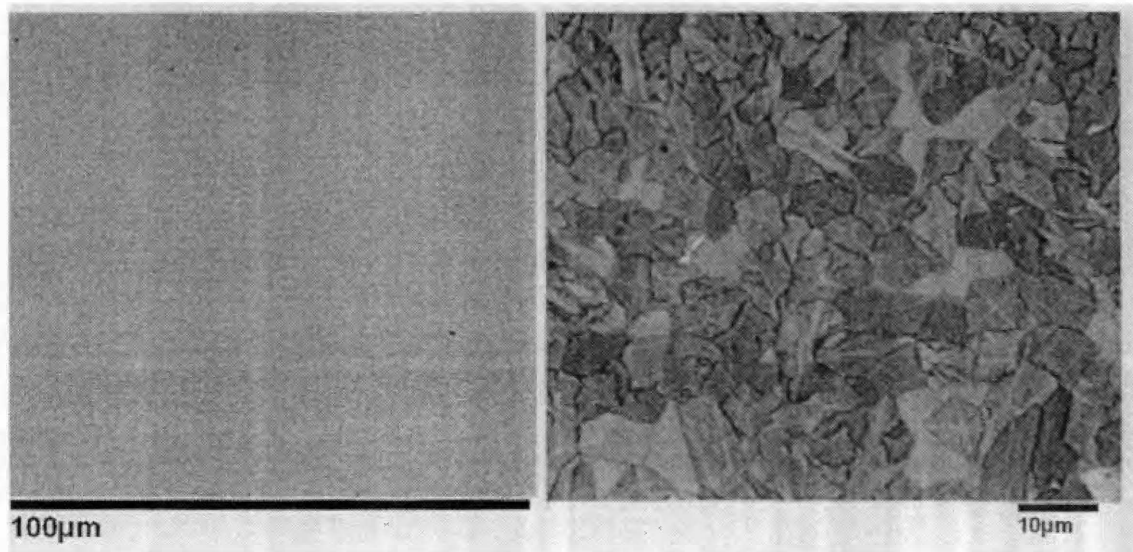


Figure A-10: BSE Images of Pure and Commercial Grade BAM-11 Near Center of Ingot. Pure Alloy (PA, 590 appm O) Is on the Right, and the Commercial Alloy (CA, 3000 appm O) Is on the Right. Reprinted from *Intermetallics*, Volume 10, CT Liu et al., Oxygen Impurity and Microalloying Effect in a Zr-Based Bulk Metallic Glass Alloy, pp. 1105-1112, 2002, with Permission from Elsevier.

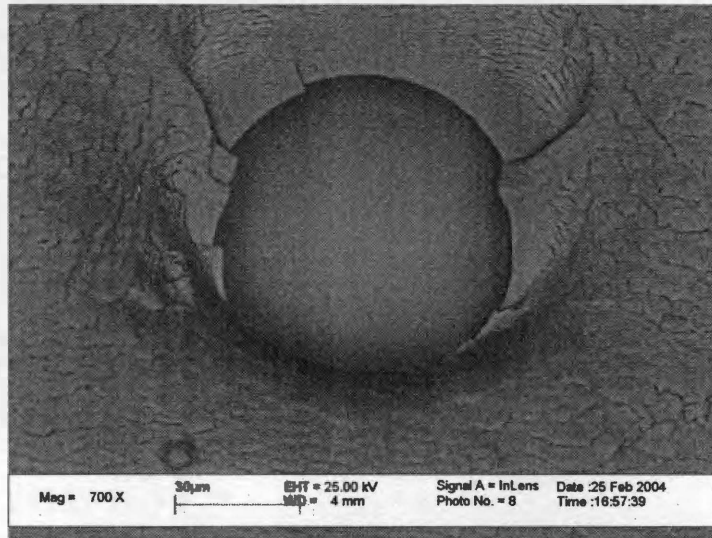


Figure A-11: SEM Image of Porosity on the Fracture Surface of a Fatigue Specimen Caused by Trapped Inert Gas During the Drop-Casting of a Zr-Based BMG.

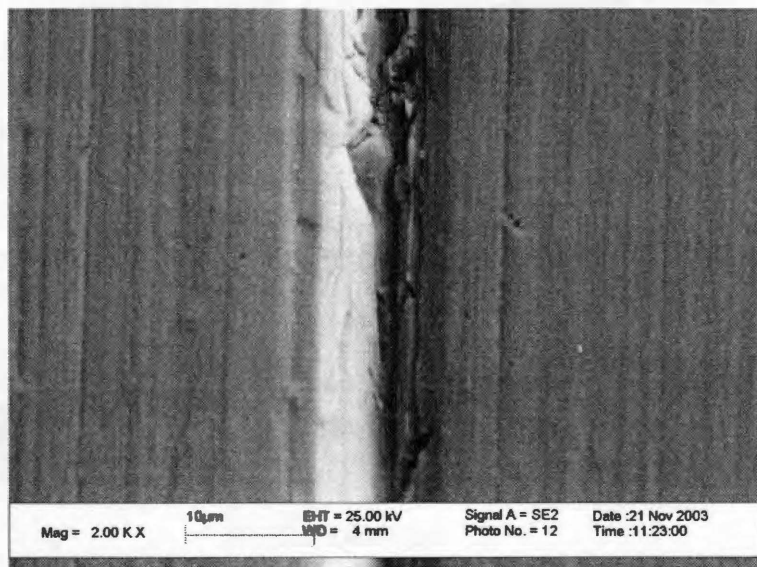


Figure A-12: SE Image of Radial Machine Marks And a Large Geometric Defect on the Outside Surface of a Round Bar Fatigue Specimen.

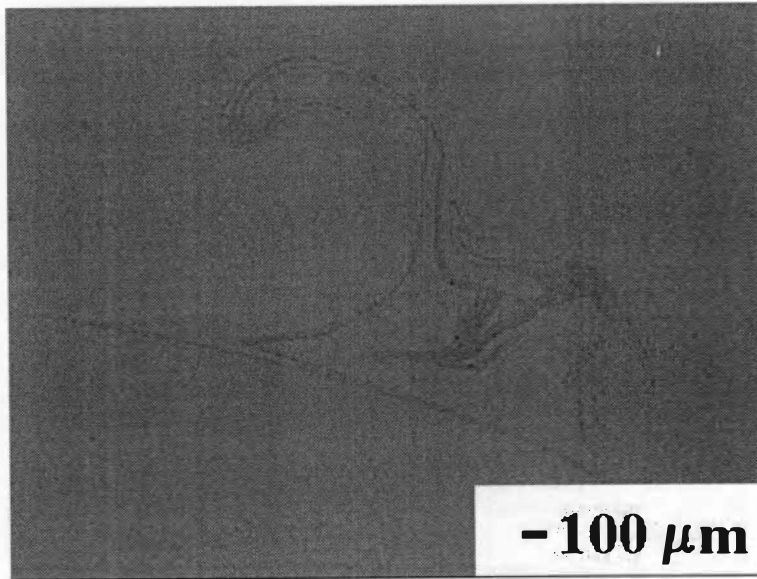


Figure A-13: Optical Micrograph Image of Etched BMG-11 As-Cast 6.4 mm Diameter Specimen Illustrating Small Bands of Crystallinity.

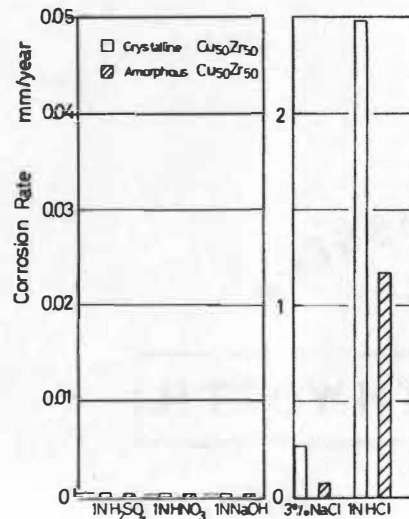


Figure A-14: Corrosion Rates of Amorphous and Crystalline Cu-50Zr Alloy in Various Environments. Reprinted from Journal of Non-Crystalline Solids, Volume 30, M. Naka, K. Hashimoto, and T. Masumoto, Corrosion Behavior of Amorphous and Crystalline $\text{Cu}_{50}\text{Ti}_{50}$ and $\text{Cu}_{50}\text{Zr}_{50}$ Alloys, p. 29, 1978, with Permission from Elsevier.

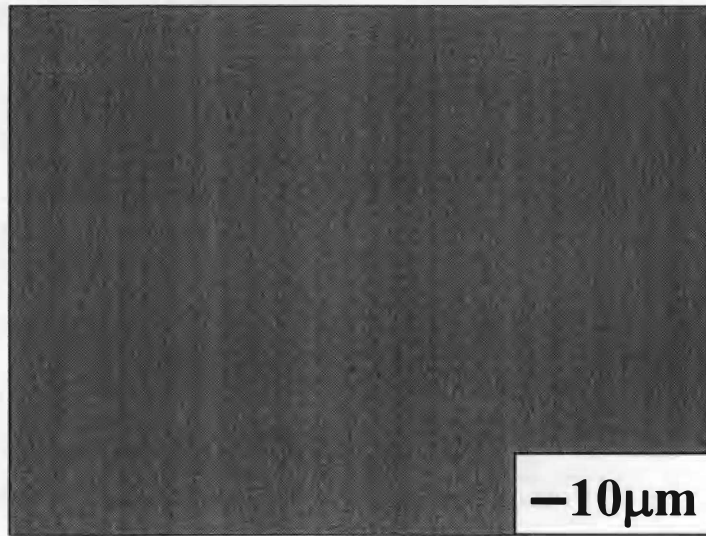


Figure A-15: Optical Photomicrograph of An As-Cast BMG-11 Sample.

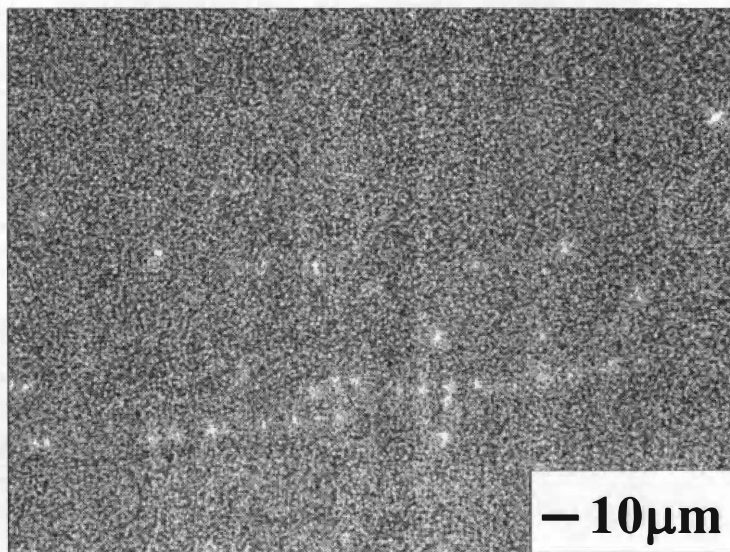


Figure A-16: Optical Photomicrograph of Crystalline BMG-11 After Annealing Treatment at 600°C for Five Hours.

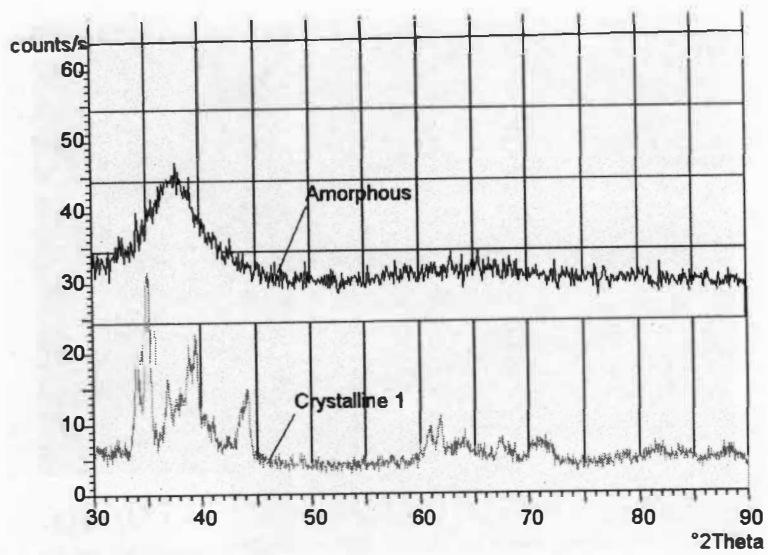


Figure A-17: X-Ray Diffraction Patterns Taken from Amorphous and Crystalline BMG-11 Samples.

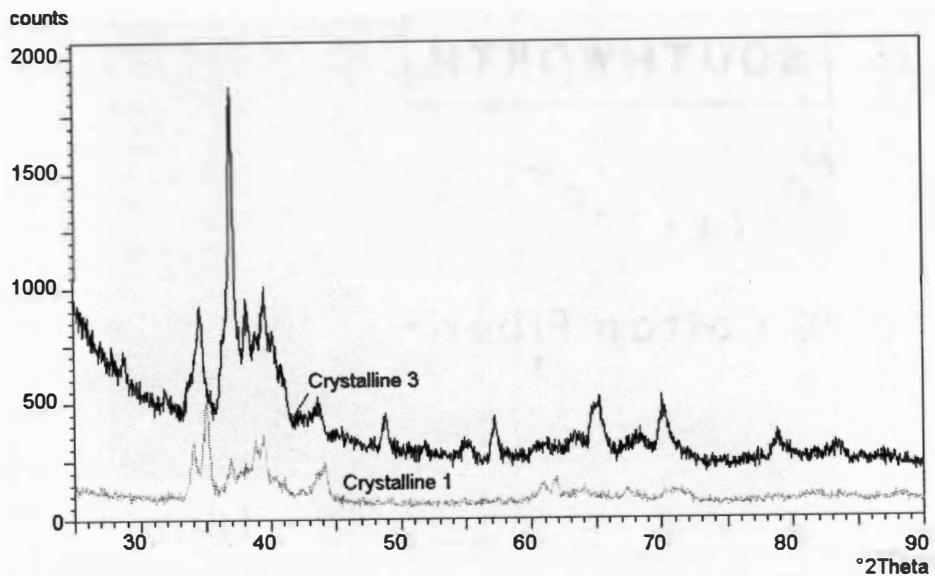


Figure A-18: X-Ray Diffraction Patterns Taken from Two Different Crystalline BMG-11 Samples.

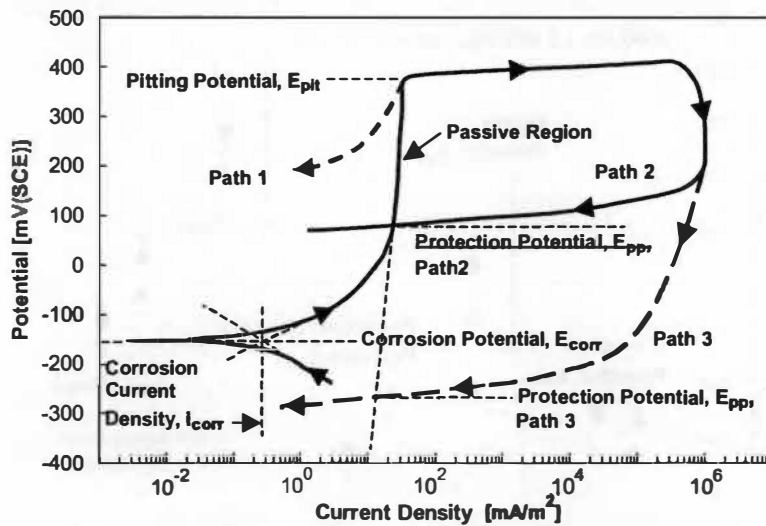


Figure A-19: Schematic Cyclic-Anodic-Polarization Curves. Reprinted from Intermetallics, Volume 10, W.H. Peter et al., Localized Corrosion Behavior of a Zirconium-Based Bulk Metallic Glass Relative to Its Crystalline State, pp. 1125-1130, 2002, with Permission from Elsevier.

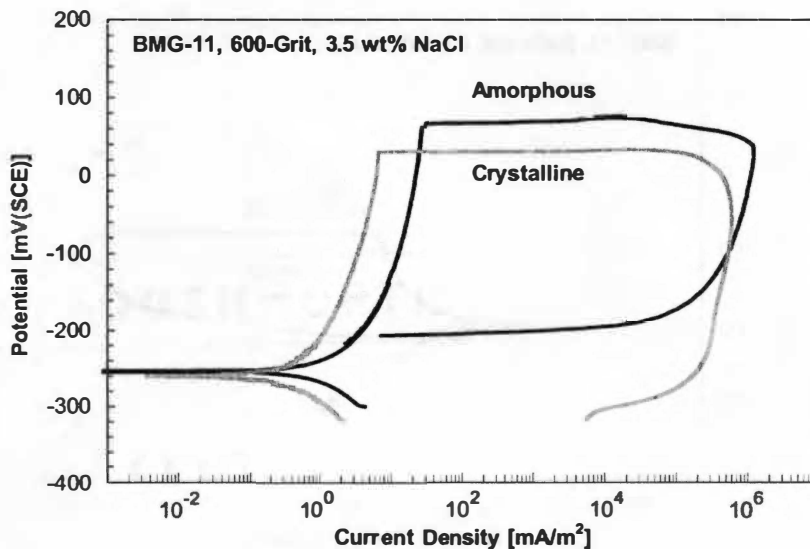


Figure A-20: Average Cyclic-Anodic-Polarization Behaviors of Amorphous and Crystalline BMG-11 with 600-Grit Surface Finish in Aerated 0.6 M NaCl Solution at Room Temperature. Reprinted from Intermetallics, Volume 10, W.H. Peter et al., Localized Corrosion Behavior of a Zirconium-Based Bulk Metallic Glass Relative to Its Crystalline State, pp. 1125-1130, 2002, with Permission from Elsevier.

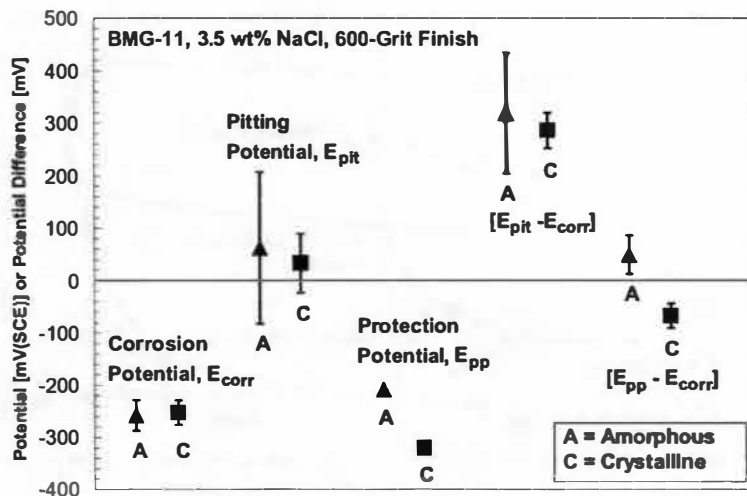


Figure A-21: Results of Electrochemical Parameters for Cyclic-Anodic-Polarization Tests of Amorphous and Crystalline BMG-11 with 600-Grit Surface Finish (Aerated 0.6 M NaCl Solution, Room Temperature). Reprinted from Intermetallics, Volume 10, W.H. Peter et al., Localized Corrosion Behavior of a Zirconium-Based Bulk Metallic Glass Relative to Its Crystalline State, pp. 1125-1130, 2002, with Permission from Elsevier.

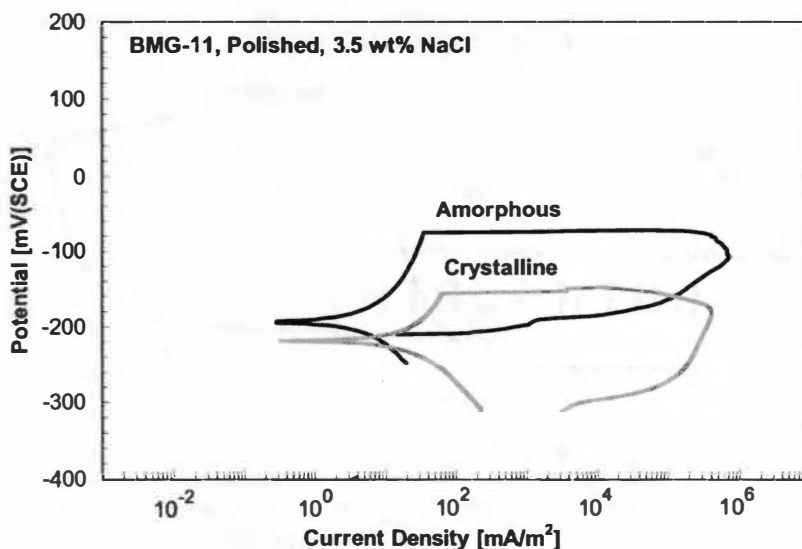


Figure A-22: Average Cyclic-Anodic-Polarization Behaviors of Amorphous and Crystalline BMG-11 with Metallographically-Polished Surface Finish in Aerated 0.6 M NaCl Solution at Room Temperature. Reprinted from Intermetallics, Volume 10, W.H. Peter et al., Localized Corrosion Behavior of a Zirconium-Based Bulk Metallic Glass Relative to Its Crystalline State, pp. 1125-1130, 2002, with Permission from Elsevier.

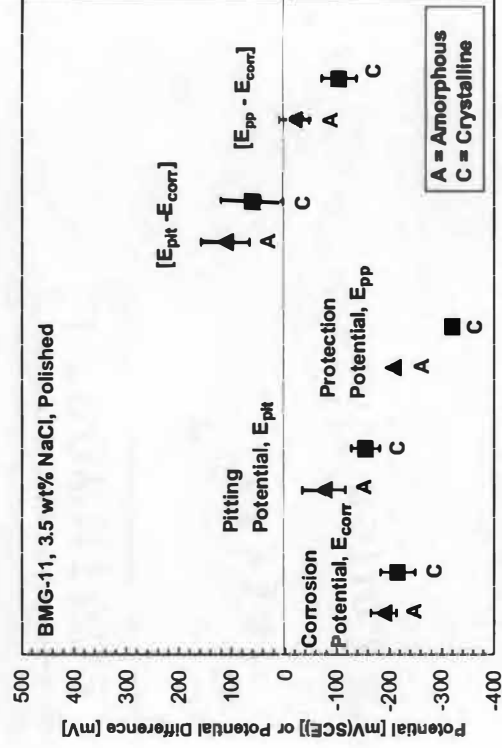


Figure A-23: Results of Electrochemical Parameters for Cyclic-Anodic-Polarization Tests of Amorphous and Crystalline BMG-11 with Polished Surface Finish (Aerated 0.6 M NaCl Solution, Room Temperature). Reprinted from Intermetallics, Volume 10, W.H. Peter et al., Localized Corrosion Behavior of a Zirconium-Based Bulk Metallic Glass Relative to Its Crystalline State, pp. 1125-1130, 2002, with Permission from Elsevier.

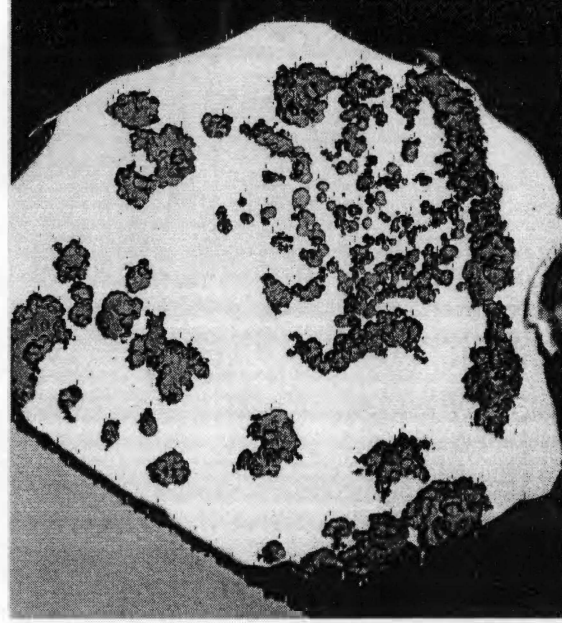


Figure A-24: Secondary Electron Image of Amorphous Corrosion Sample After Being Tested in 0.6 M NaCl Solution (Low Magnification). The 6.4 mm Diameter of the Ingot Is Fully Visible.

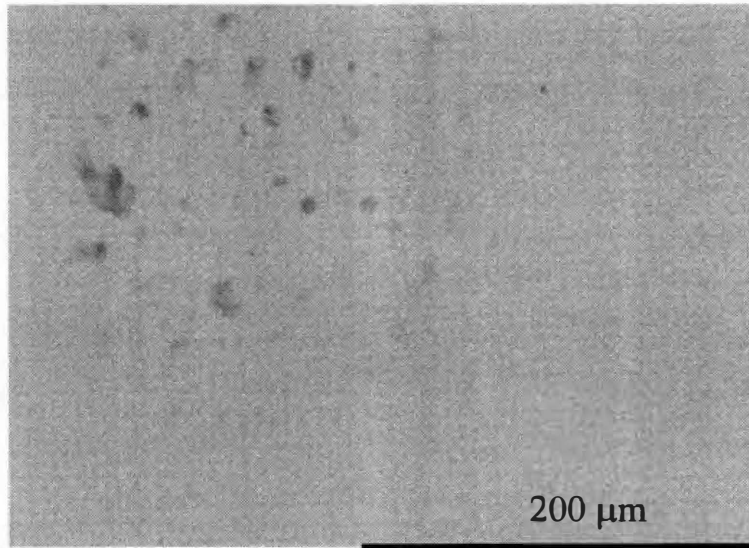


Figure A-25: Secondary Electron Image of the Porosity in the Amorphous Corrosion Sample After Being Tested in 0.6 M NaCl Solution.

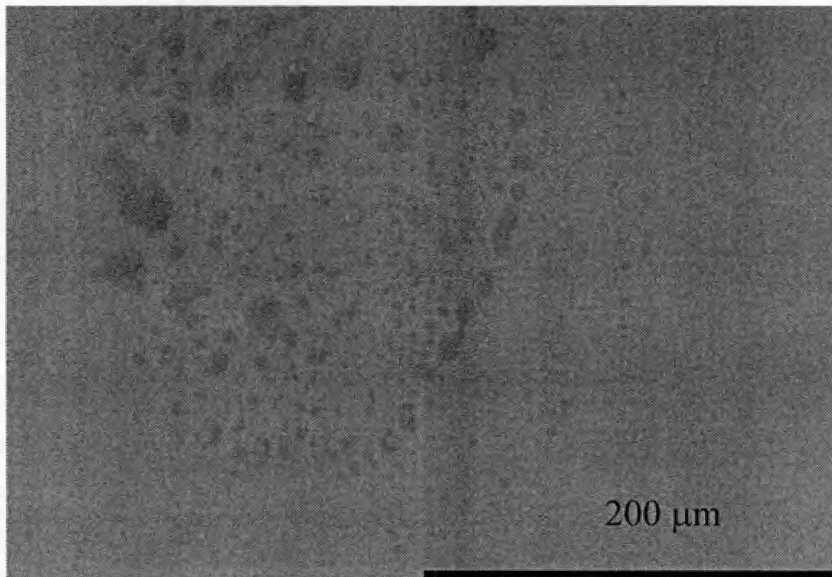


Figure A-26: Back-Scattered Electron Image of Porosity in the Amorphous Corrosion Sample After Being Tested in 0.6 M NaCl Solution.

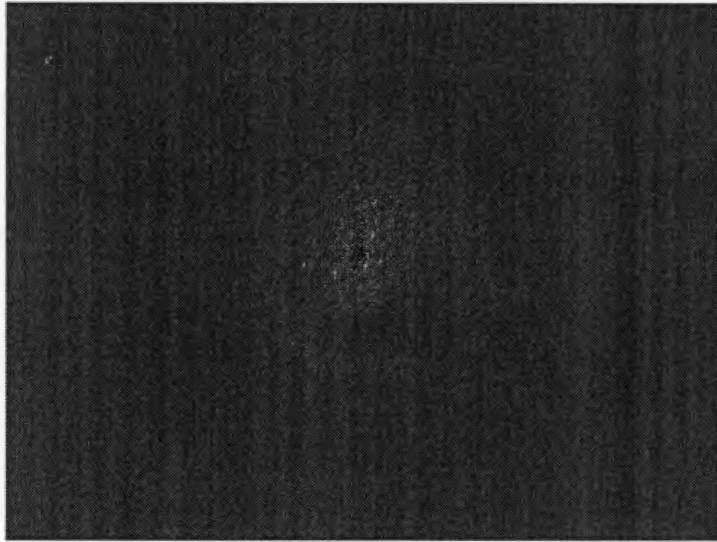


Figure A-27: Secondary Electron Image of a Pit in a Crystalline Corrosion Sample After Being Tested in 0.6 M NaCl Solution (Same Scale as A-28).

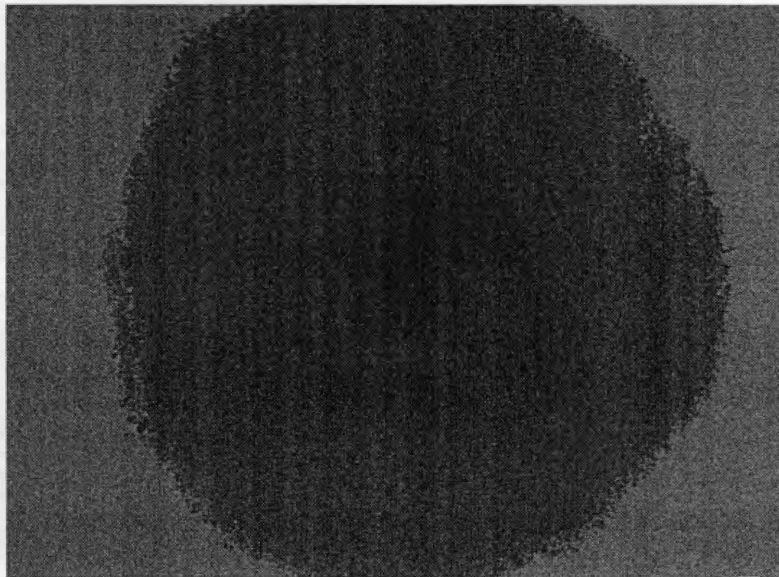


Figure A-28: Back-Scattered Electron Image of a Pit in a Crystalline Corrosion Sample After Being Tested in 0.6 M NaCl Solution (Same Scale as A-27).

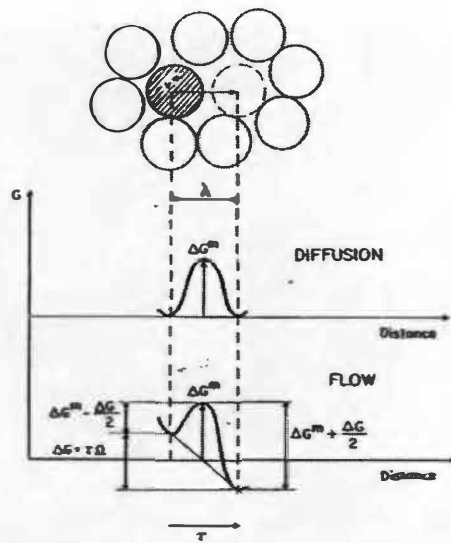


Figure A-29: "Illustration of an individual atomic jump, the basic step for macroscopic diffusion and flow." Reprinted from Acta Metallurgica, Volume 25, F. Spaepen, A Microscopic Mechanism for Steady State Inhomogeneous Flow in Metallic Glass, pp. 407-415, 1977, with Permission from Elsevier.

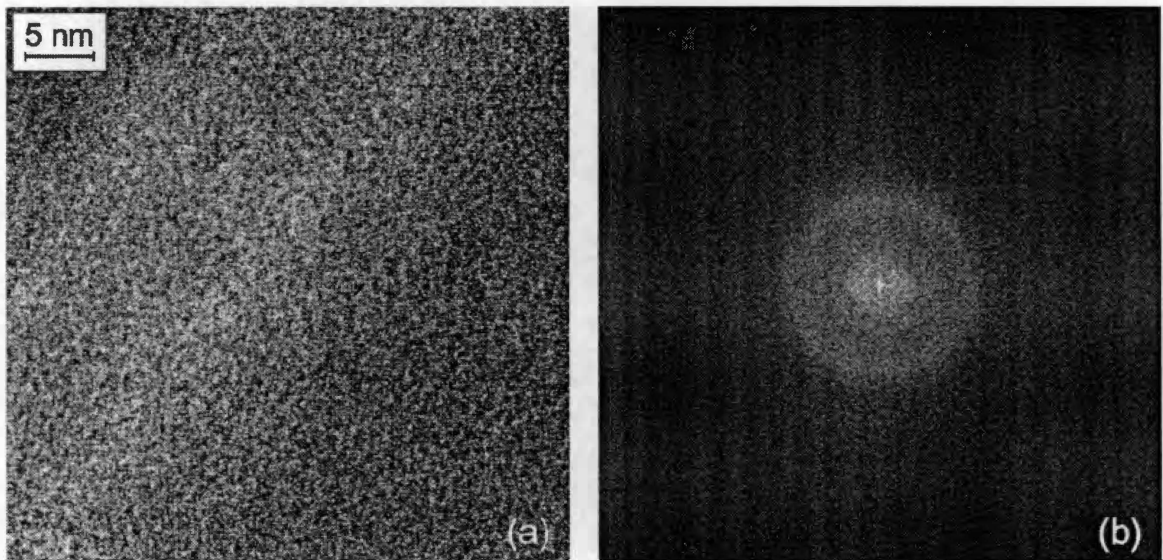


Figure A-30: Shear Band Near Crack Tip. HRTEM Image (a) and Fourier Transform (b) of a Shear Band Near a Crack Tip. Reprinted Figure with Permission from J Li et al., Physical Review B, Volume 65, pp 144201-1-144201-6, 2002. Copyright 2002 by the American Physical Society.

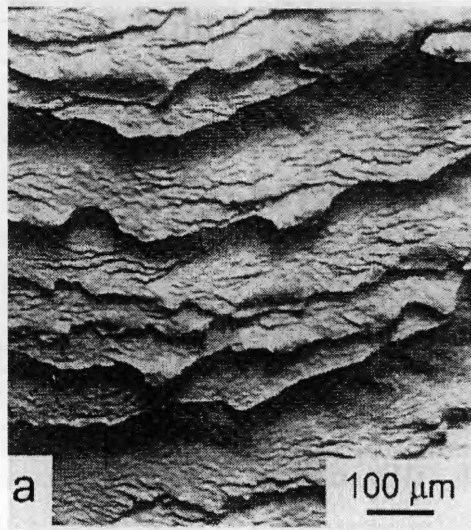


Figure A-31: SEM of an Overload Fracture Surface of a Zirconium-Based BMG. Reprinted from *Intermetallics*, Volume 8, R.O. Ritchie et al., *Fracture, Fatigue and Environmentally-Assisted Failure of a Zr-Based Bulk Amorphous Metal*, pp. 469-475, 2000, with Permission from Elsevier.

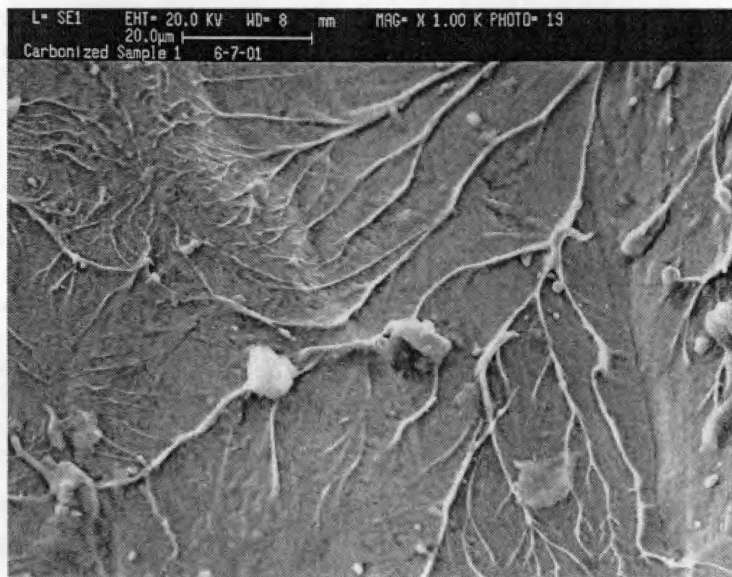


Figure A-32: Secondary Electron Image of the Overload Fracture Surface of a Zr-Based Metallic Glass.

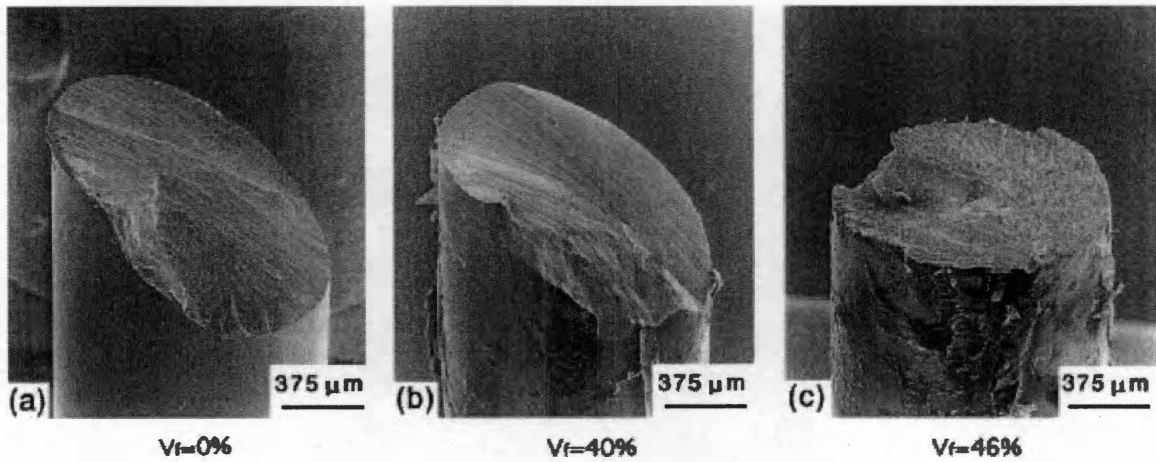


Figure A-33: Tensile Fracture Surface of Amorphous ZrAlCuPd Alloy with Varying Percents of Volume Fraction (V_f) of Nanocrystallization (a=0%, b=40%, c=46%). Reprinted from *Intermetallics*, Volume 8, A. Inoue, *Mechanical Properties of Zr-based Glassy Alloys Containing Nanoscale Compound Particles*, pp. 469-475, 2000, with Permission from Elsevier.

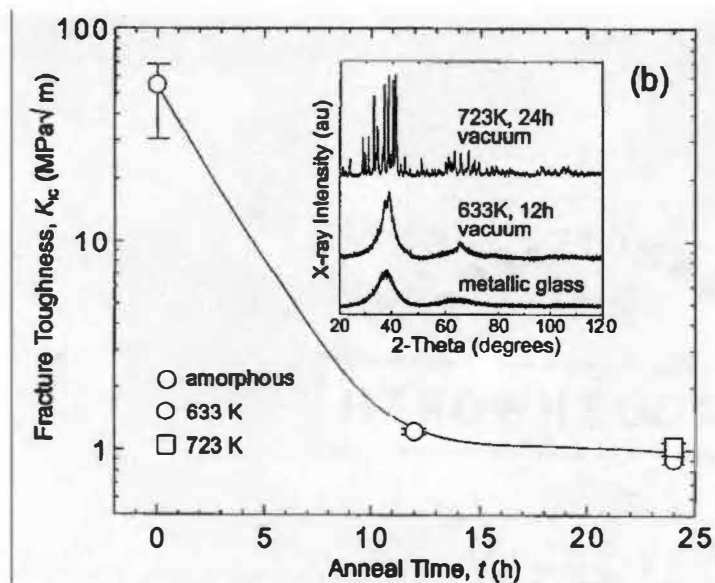


Figure A-34: Fracture Toughness Versus Anneal Time. Reprinted from *Materials Research Society: Bulk Metallic Glasses*, Volume 554, C.J. Gilbert et al., *Fracture and Fatigue in a Zr-Based Bulk Metallic Glass*, pp. 343-354, 1999, with Permission from Materials Research Society.

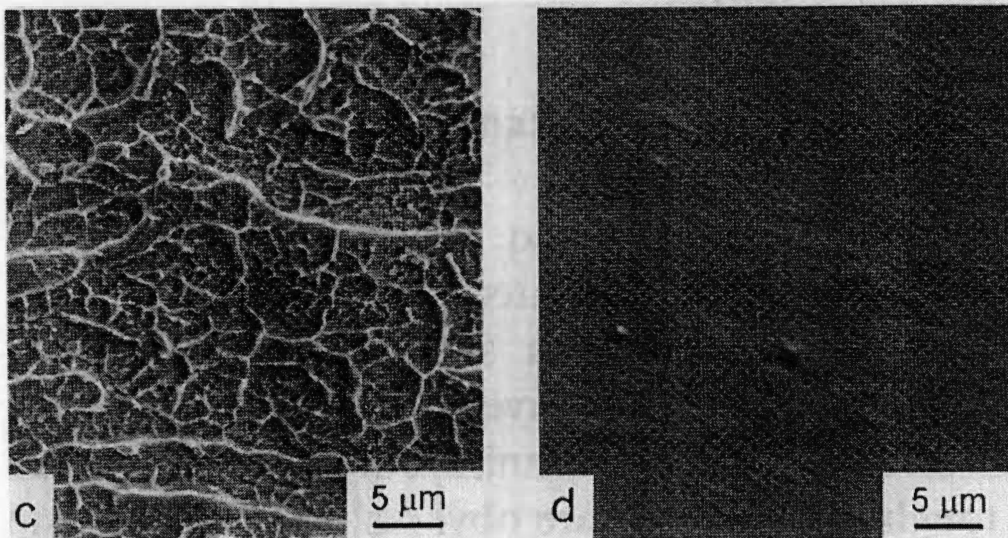


Figure A-35: SEMs of an Overload Fracture Surface for a Metallic Glass (Left) and 5% Crystallized Sample (Right). Reprinted from *Intermetallics*, Volume 8, R.O. Ritchie et al., *Fracture, Fatigue and Environmentally-Assisted Failure of a Zr-Based Bulk Amorphous Metal*, pp. 469-475, 2000 with Permission from Elsevier Science.

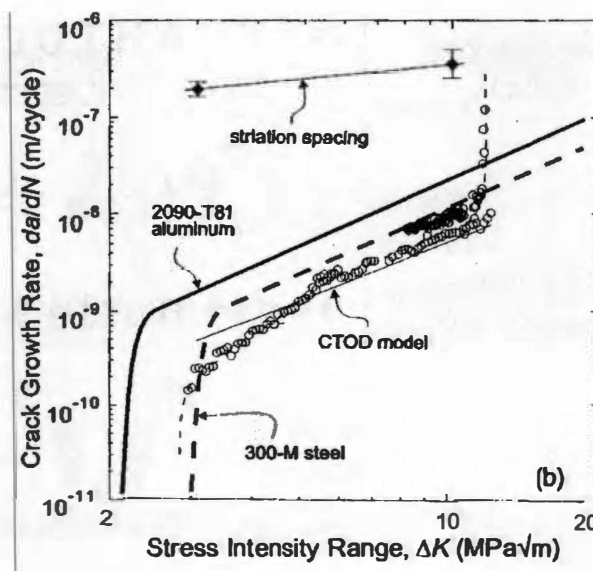


Figure A-36: Fatigue Crack Growth Results for $Zr_{41.2}Ti_{13.8}Cu_{12.5}Ni_{10}Be_{22.5}$ BMG, 300-M Ultrahigh Strength Steel, and 2090-T81 Aluminum Lithium Alloy. Reprinted from *Materials Research Society: Bulk Metallic Glasses*, Volume 554, C.J. Gilbert et al., *Fracture and Fatigue in a Zr-Based Bulk Metallic Glass*, pp. 343-354, 1999, with Permission from Materials Research Society.

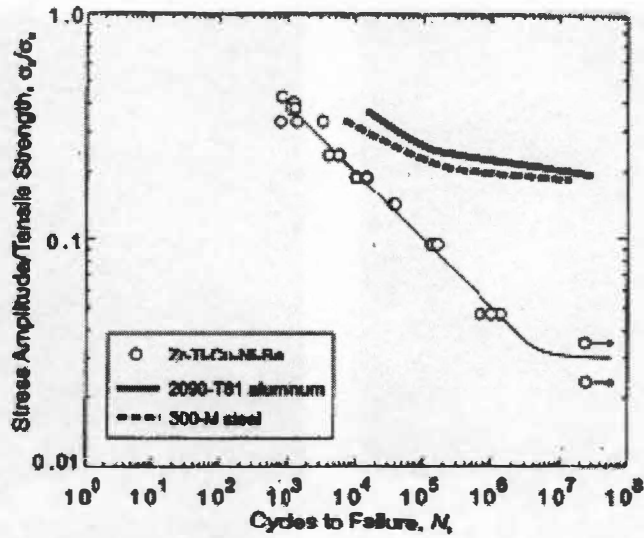


Figure A-37: S-N Testing Results for $Zr_{41.2}Ti_{13.8}Cu_{12.5}Ni_{10}Be_{22.5}$ BMG, 300-M Ultrahigh Strength Steel, and 2090-T81 Aluminum Lithium Alloy. Reprinted from Materials Research Society: Bulk Metallic Glasses, Volume 554, C.J. Gilbert et al., Fracture and Fatigue in a Zr-Based Bulk Metallic Glass, pp. 343-354, 1999, with Permission from Materials Research Society.

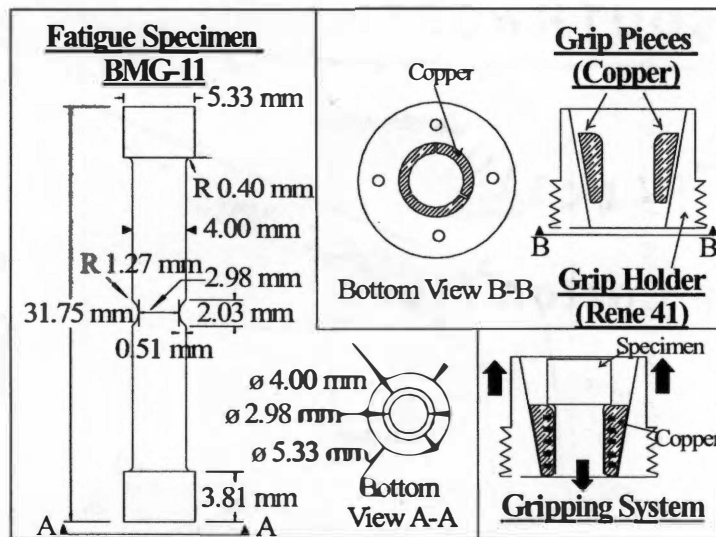


Figure A-38: BMG-11 Specimen Geometry for Fatigue Testing in Air and Vacuum.

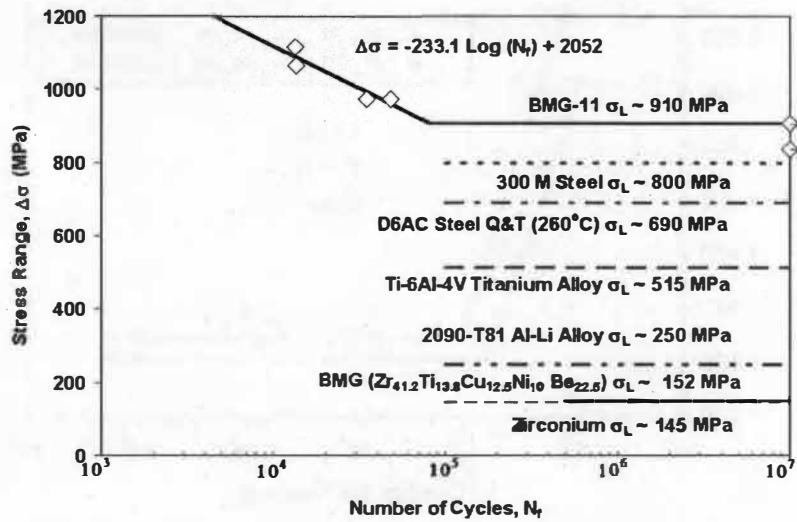


Figure A-39: Stress-Range / Fatigue-Life Data of Notched BMG-11 Specimens Tested in Air and Compared with the Fatigue Endurance Limits (σ_L) of High-Strength Alloys [1-7,54,57,83].

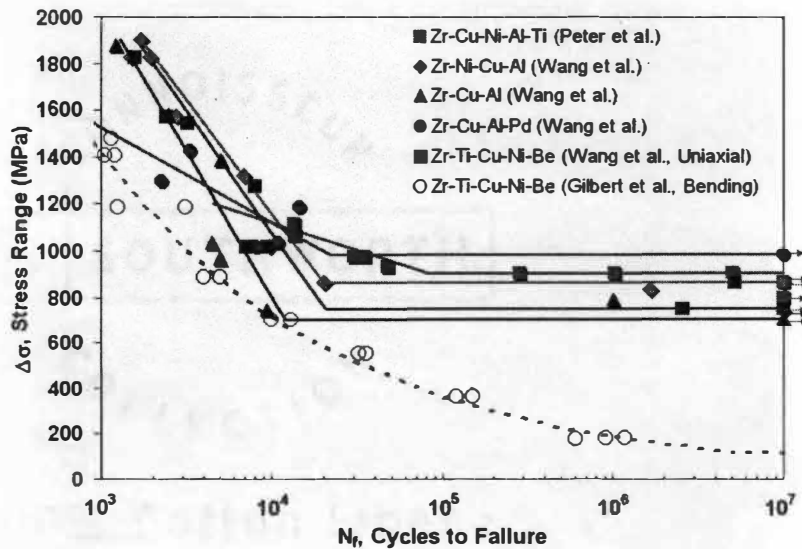


Figure A-40: Stress-Range / Fatigue-Life Data of Various BMGs [1-10]. Results from Gilbert et al. [1-5], Peter et al. [6-7], and Wang et al. [8-10] Are Included.

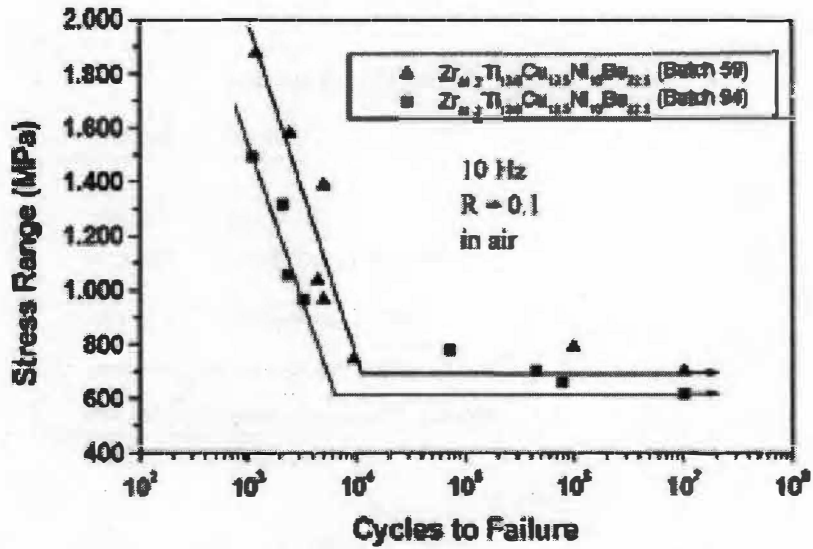


Figure A-41: Stress-Range/Fatigue-Life Data of Notched $Zr_{41}Ti_{14}Cu_{12}Ni_{10}Be_{23}$ Specimens Tested in Air with $R = 0.1$ and a Frequency of 10 Hz. Differences in Batch 59 and 94 Are Related to Amount of Impurities. Reprinted from Intermetallics, Volume 13, G.Y. Wang et al., Fatigue Behavior of Zr-Ti-Ni-Cu-Be Bulk Metallic Glasses, pp. 429-435, 2005, with Permission from Elsevier.

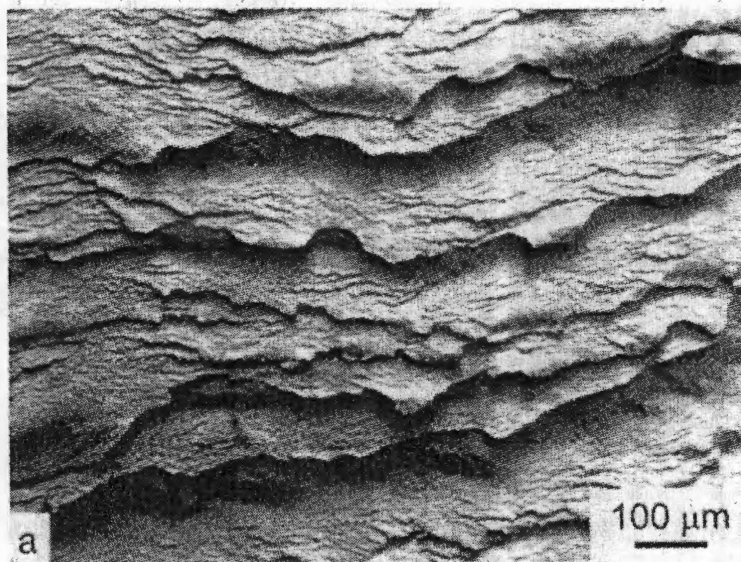


Figure A-42: Secondary Electron Image of Shear Steps in an Overload Fracture Surface. Reprinted from Materials Research Society: Bulk Metallic Glasses, Volume 554, C.J. Gilbert et al., Fracture and Fatigue in a Zr-Based Bulk Metallic Glass, pp. 343-354, 1999, with Permission from Materials Research Society.

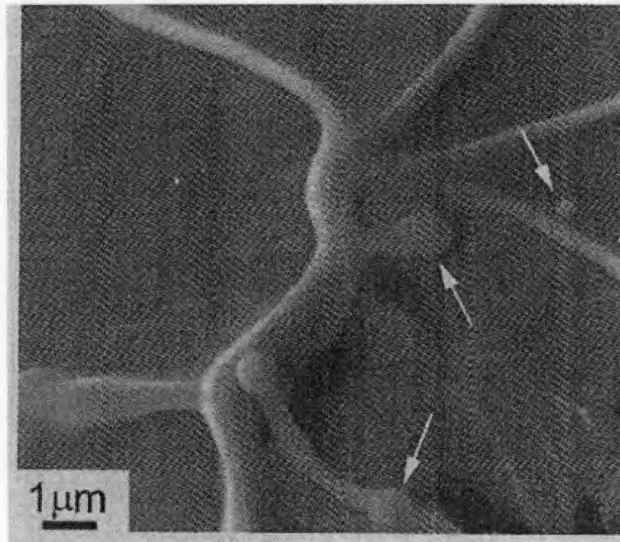


Figure A-43: SE Image of an Overload Fracture Surface for a Metallic Glass Illustrating Vein Morphology. Arrows illustrate droplets that often contain a crystalline phase. Reprinted from Materials Research Society: Bulk Metallic Glasses, Volume 554, C.J. Gilbert et al., Fracture and Fatigue in a Zr-Based Bulk Metallic Glass, pp. 343-354, 1999, with Permission from Materials Research Society.

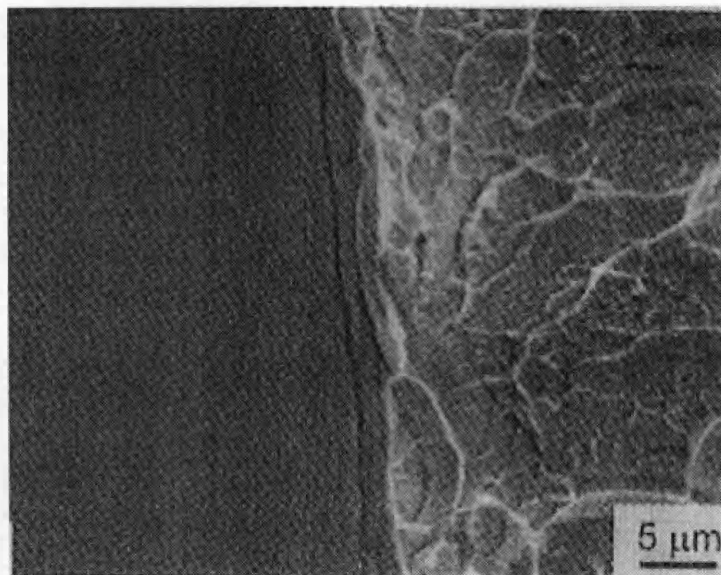


Figure A-44: Secondary Electron Image of the Division Between the Fatigue (Left) and Overload (Right) Fracture Surfaces. Reprinted from Materials Research Society: Bulk Metallic Glasses, Volume 554, C.J. Gilbert et al., Fracture and Fatigue in a Zr-Based Bulk Metallic Glass, pp. 343-354, 1999, with Permission from Materials Research Society.

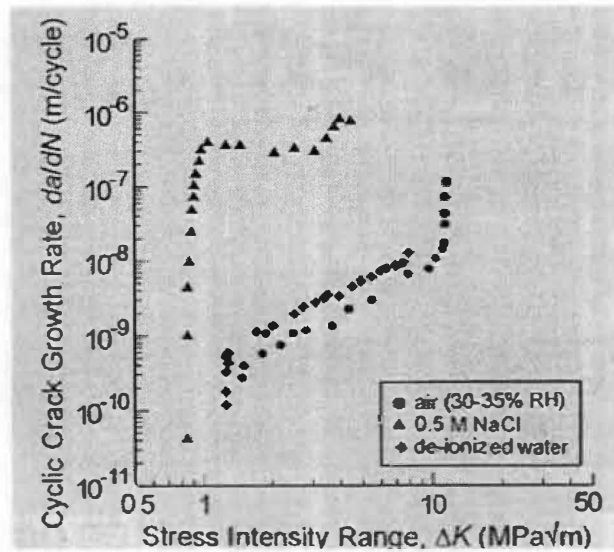


Figure A-45: Fatigue-Crack Growth Rates in Amorphous $Zr_{41.2}Ti_{13.8}Cu_{12.5}Ni_{10}Be_{22.5}$ for Various Stress Intensity Ranges in Three Environments. Reprinted from *Intermetallics*, Volume 8, R.O. Ritchie et al., *Fracture, Fatigue and Environmentally-Assisted Failure of a Zr-Based Bulk Amorphous Metal*, pp. 469-475, 2000, with Permission from Elsevier.

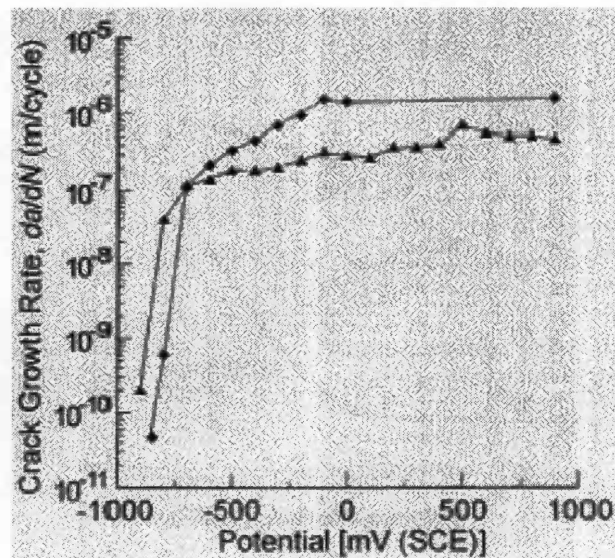


Figure A-46: Fatigue-Crack Growth Rates at Constant $\Delta K = 1.5 \text{ MPa(m)}^{0.5}$ in Amorphous $Zr_{41.2}Ti_{13.8}Cu_{12.5}Ni_{10}Be_{22.5}$ in 0.5 M NaCl. Reprinted from *Intermetallics*, Volume 8, R.O. Ritchie et al., *Fracture, Fatigue and Environmentally-Assisted Failure of a Zr-Based Bulk Amorphous Metal*, pp. 469-475, 2000, with Permission from Elsevier.

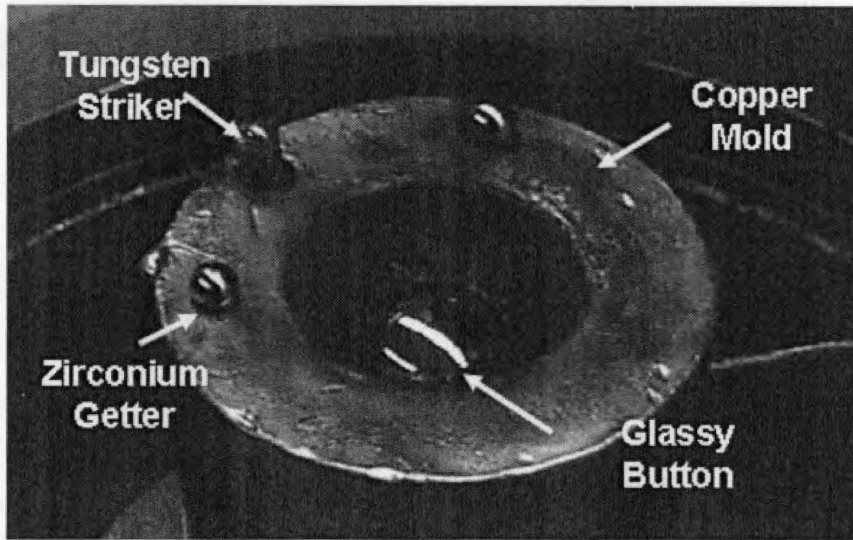


Figure A-47: BMG-11 Sample After Mixing by Arc Melting, but Before Drop Casting.

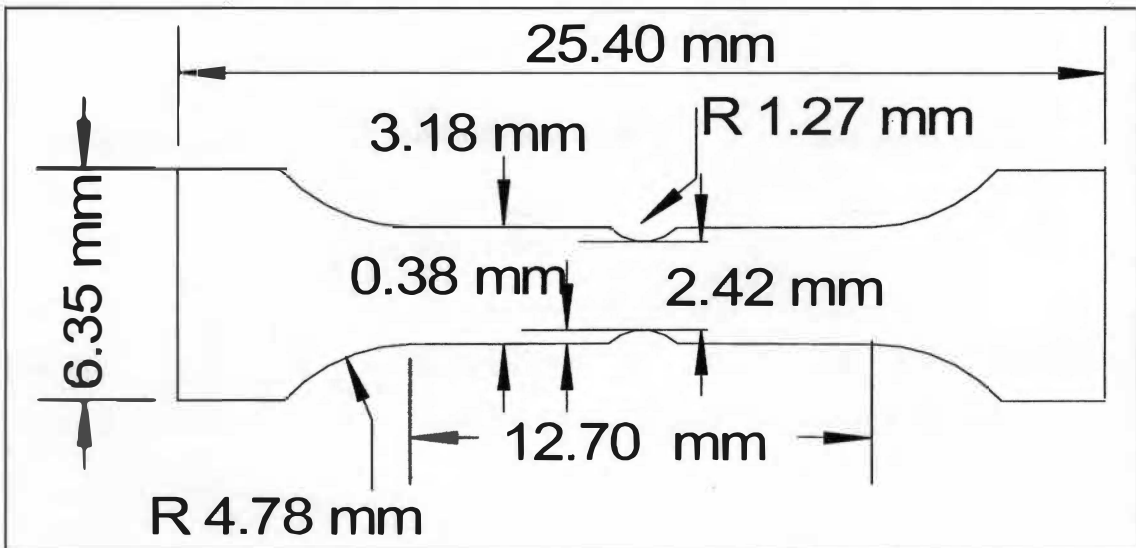


Figure A-48: The Initial BMG-11 Specimen Geometry for Fatigue Testing in Air and Vacuum.

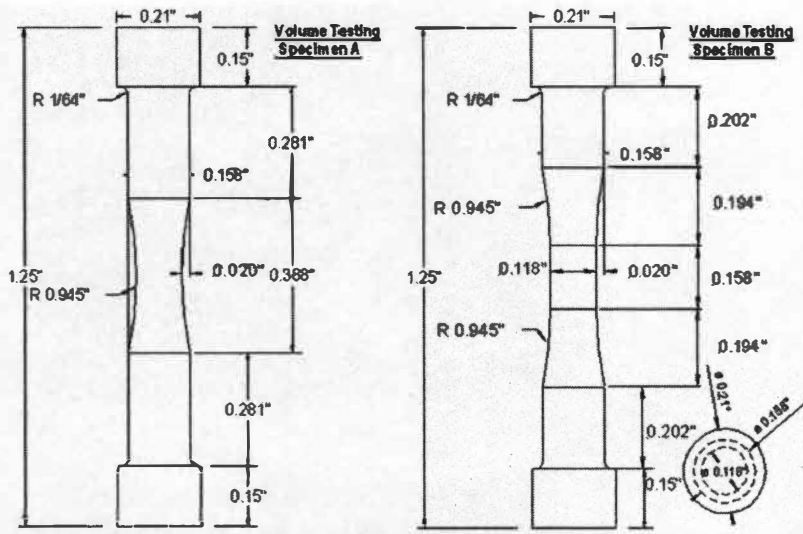


Figure A-49: Volume / Surface Area Specimen Geometries for Uniaxial Fatigue Testing. The Radial Taper in Both Geometries Are the Same. However, Geometry B (on the Right) Has a Cylindrical Testing Section, and Geometry A (on the Left) Has Its Testing Section on a Single Plane.

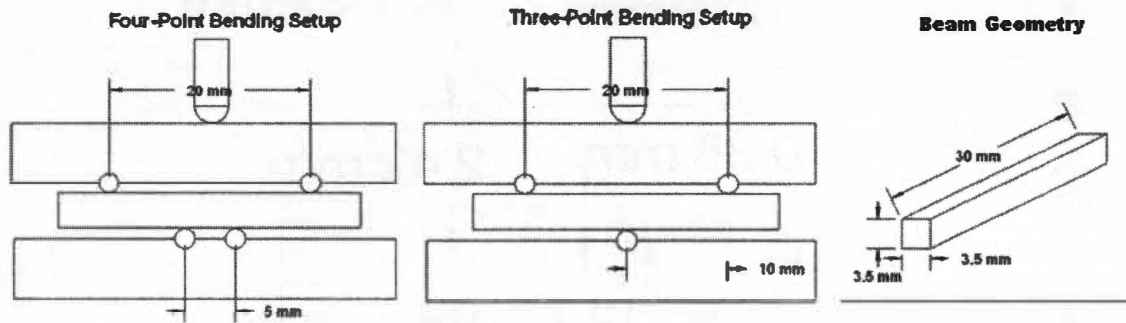


Figure A-50: Four-Point Bending Setup, Three-Point Bending Setup, and Beam Geometry for Fatigue Studies.

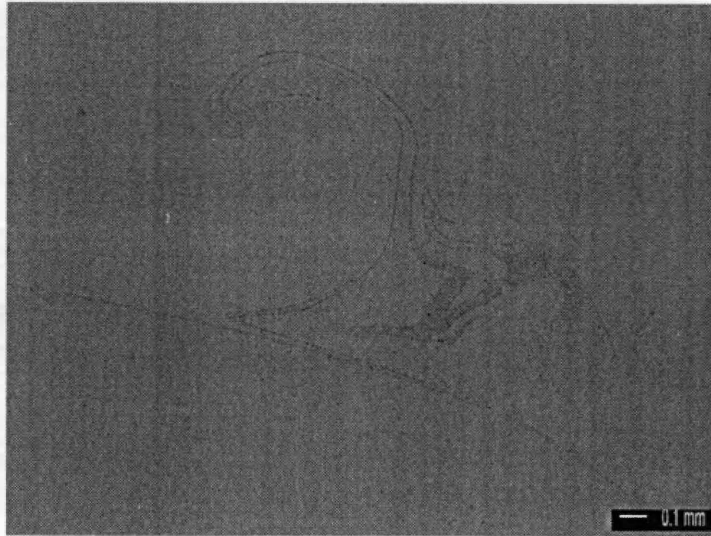


Figure A-51: Amorphous Sample with Crystal Starlet Spiral.

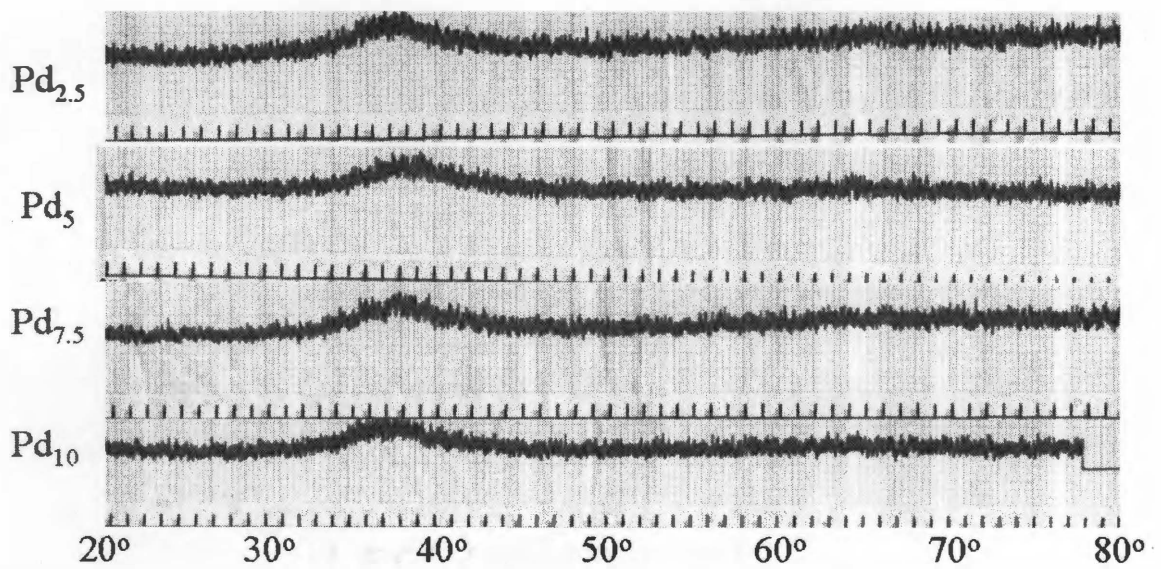


Figure A-52: X-Ray Diffraction Patterns of As-Cast 2 mm Diameter Ingots of a $Zr_{52.5}Ni_{14.6}Al_{10}Ti_5Cu_{(17.4-Y)}Pd_Y$, at. %, BMG where Y is 2.5, 5, 7.5, or 10.

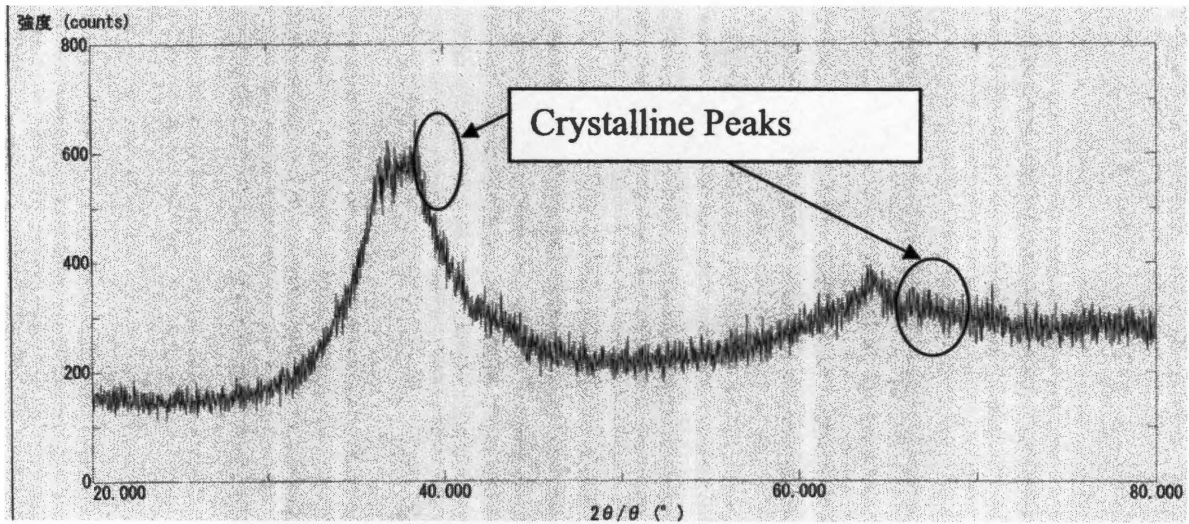


Figure A-53: X-Ray Diffraction Pattern of As-Cast 6 mm Diameter Ingot of a $Zr_{52.5}Ni_{14.6}Al_{10}Ti_5Cu_{10.4}Pd_{7.5}$, at. %, BMG.

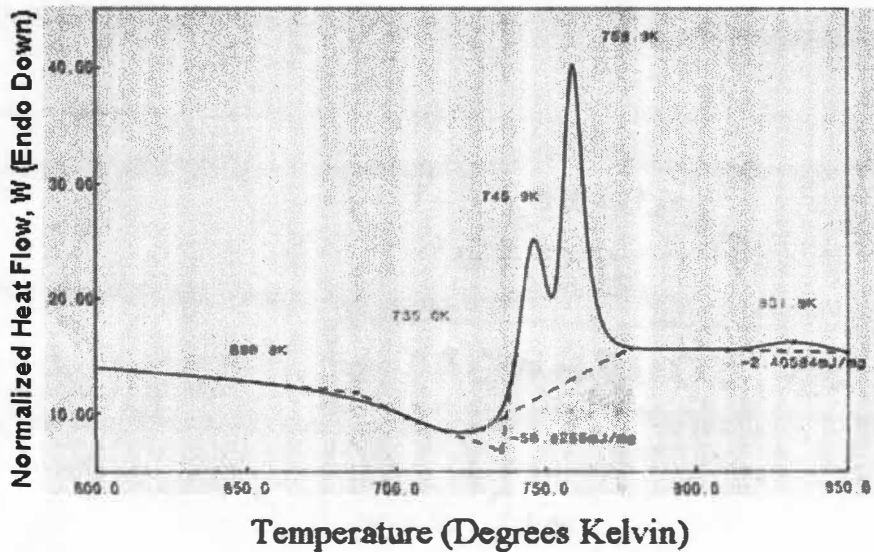


Figure A-54: Differential Scanning Calorimetry of As-Cast 2 mm Diameter Ingot of a $Zr_{52.5}Ni_{14.6}Al_{10}Ti_5Cu_{15.4}Pd_{2.5}$, at. %, BMG.

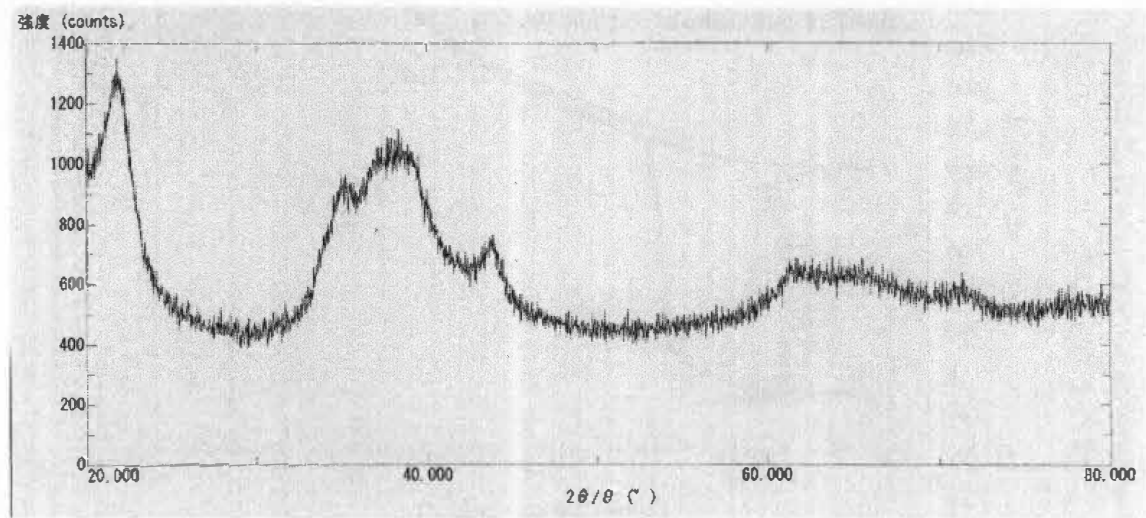


Figure A-55: X-Ray Diffraction Pattern of 2 mm Diameter Ingot of a $Zr_{52.5}Ni_{14.6}Al_{10}Ti_5Cu_{15.4}Pd_{2.5}$, at. %, BMG After Annealing for Ten Minutes at the Crystallization Temperature.

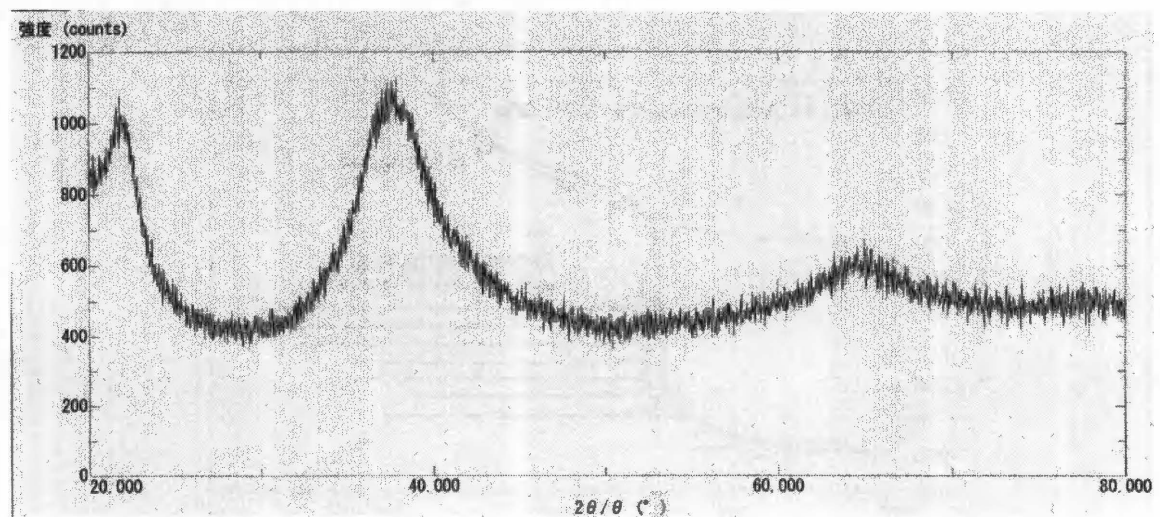


Figure A-56: X-Ray Diffraction Pattern of 2 mm Diameter Ingot of a $Zr_{52.5}Ni_{14.6}Al_{10}Ti_5Cu_{13.9}Pd_5$, at. %, BMG After Annealing for Ten Minutes at 20° K Above the Crystallization Temperature.

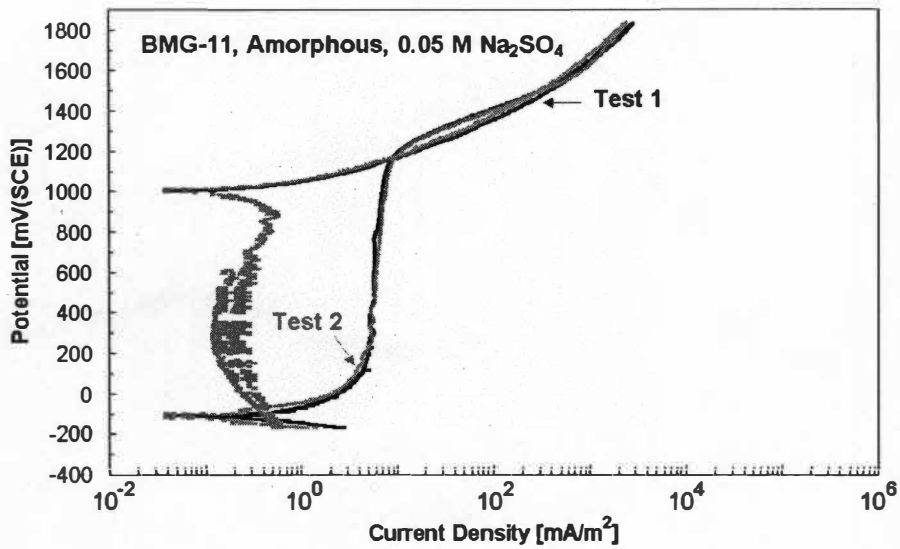


Figure A-57: Anodic-Polarization Behaviors of Amorphous BMG-11 in Aerated 0.05 M Na₂SO₄ Solution at Room Temperature with the Surface Undisturbed.

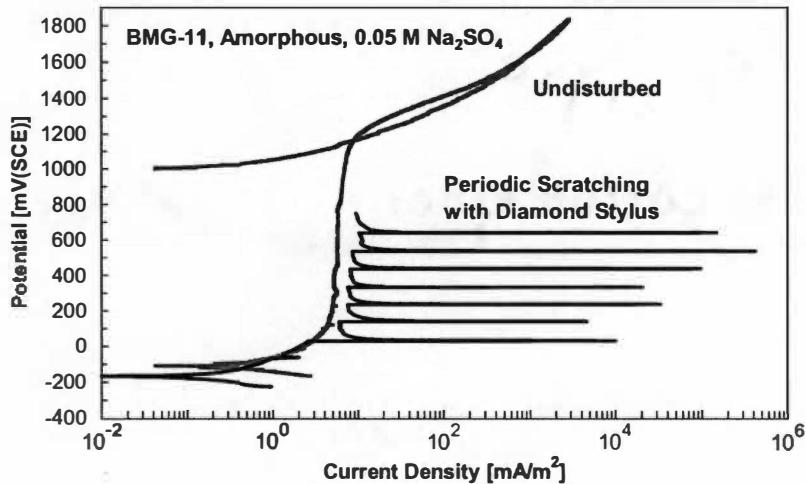


Figure A-58: Anodic-Polarization Behaviors of Amorphous BMG-11 in Aerated 0.05 M Na₂SO₄ Solution at Room Temperature. Both Curves with the Surface Undisturbed and with the Surface Periodically Scratched with a Diamond Stylus Are Displayed.

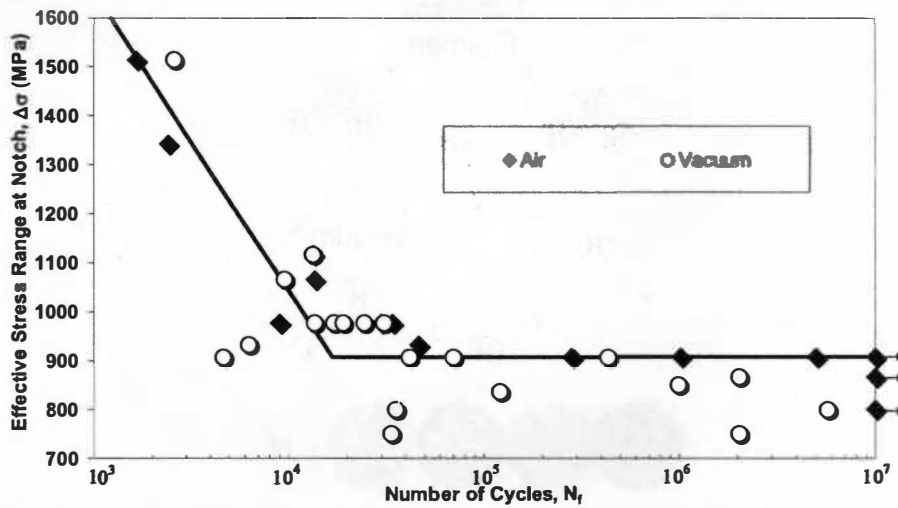


Figure A-59: Stress-Range / Fatigue-Life Data of Notched BMG-11 Specimens Tested in Air and Vacuum with $R = 0.1$ and a Frequency of 10 Hz.

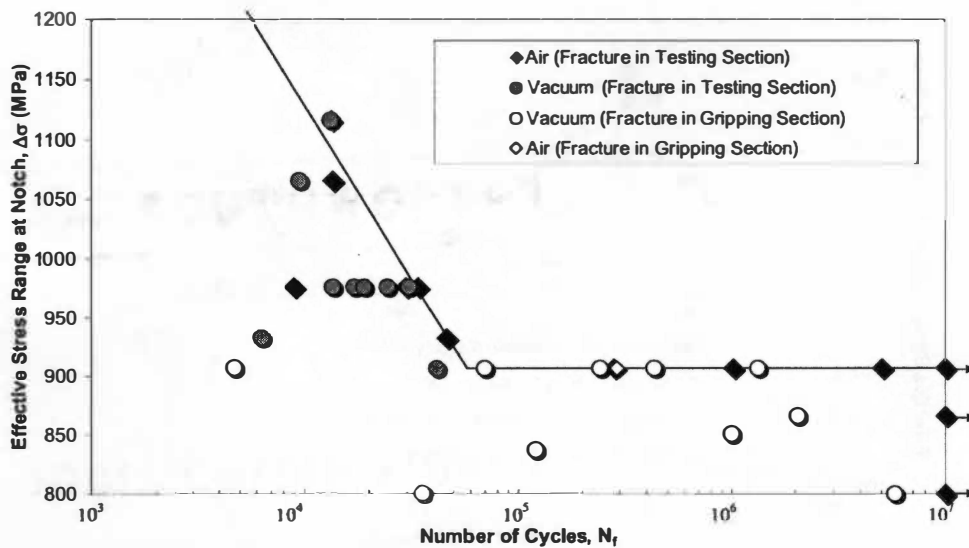


Figure A-60: Stress-Range / Fatigue-Life Data of Notched BMG-11 Specimens Tested in Air and Vacuum With the Results of the Fracture Location (Gripping Section Versus Testing Section). The R Ratio Was 0.1 and the Frequency Was 10 Hz.

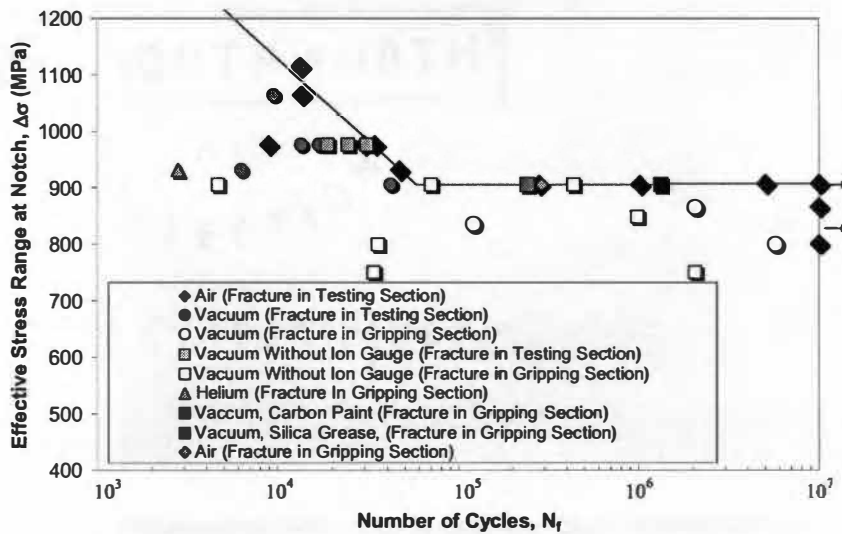


Figure A-63: Stress-Range / Fatigue-Life Data of Notched BMG-11 Specimens Tested in Air and Vacuum with All the Present Diversifications. The R Ratio Was 0.1 and the Frequency Was 10 Hz.

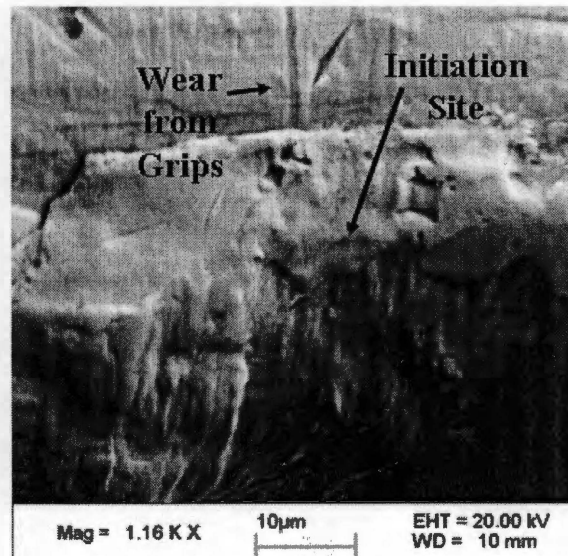


Figure A-64: SE Image of the Side of a Fractured Fatigue Specimen, Tested in Vacuum. The Fracture Surface Would Be Perpendicular and at the Bottom of This Image. The Crack Initiation Site Is Labeled, and Wear from the Gripping Section Is Visible.

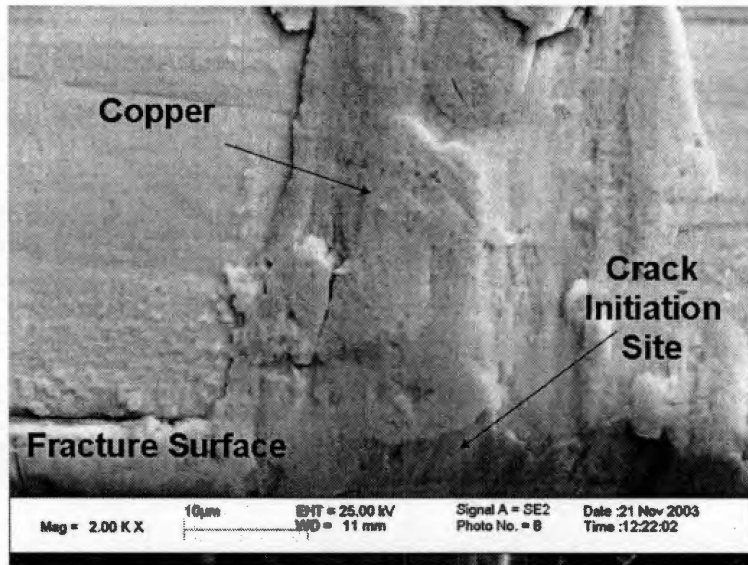


Figure A-65: Secondary Electron Image of Copper Smear Near the Crack Initiation Site.

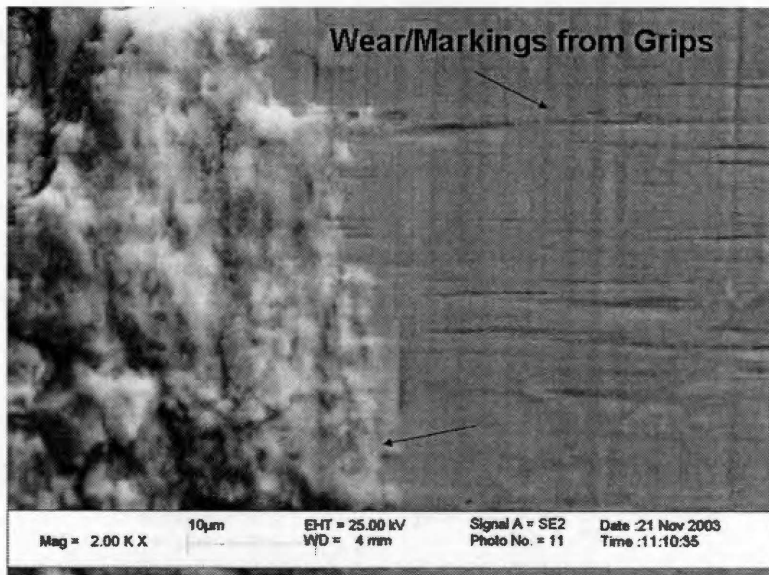


Figure A-66: Secondary Electron Image of Oxide Near Copper Grip Location of Sample Tested in Air.

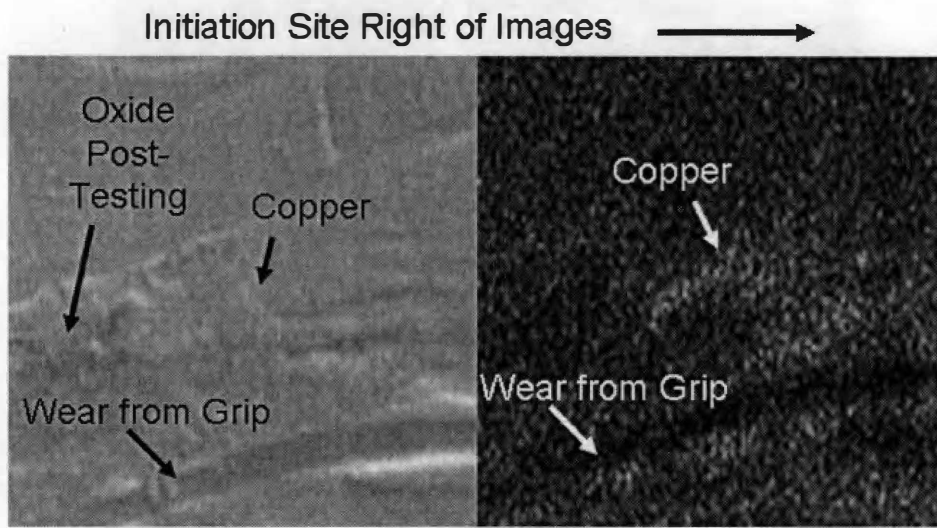


Figure A-67: Energy Dispersive Spectrum Map for K_{α} Copper Energy Level of the Outside Surface of the Round Bar Specimen. This Image Is Located at the Crack Initiation Site.

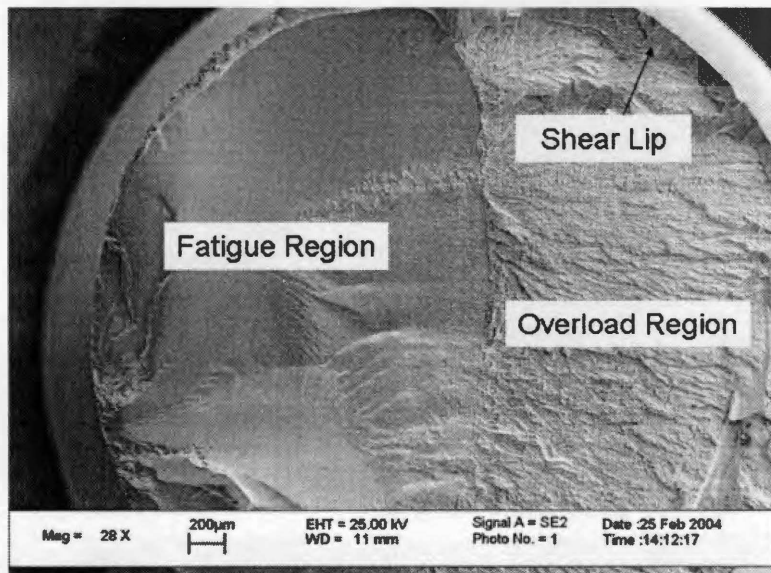


Figure A-68: Secondary Electron Image of All Three of the Distinct Fracture Morphologies.

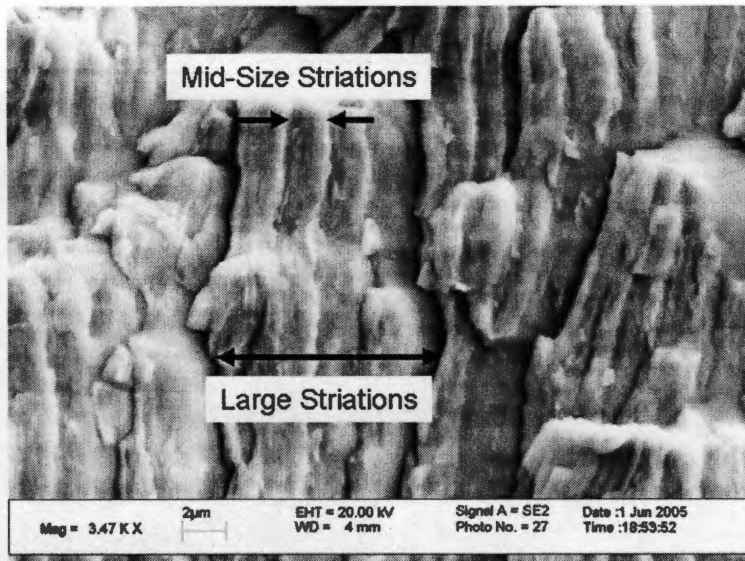


Figure A-69: Secondary Electron Image Illustrating Large and Mid-Size Striations. Small Striations Associated with Individual Cycles Are Not Labeled, But Are Visible as Well.

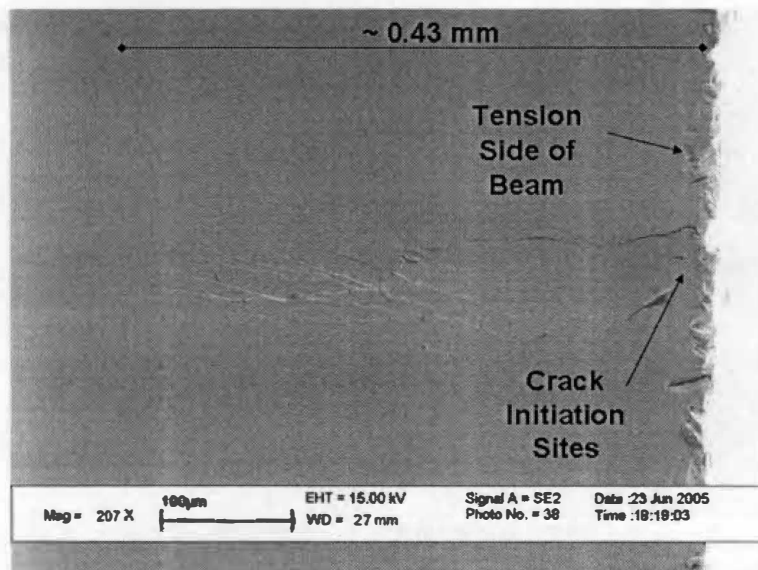


Figure A-70: Secondary Electron Image of Side Profile of Beam Specimen (The Right Side of the Image is the Tension Edge). Note the Angle of Most of the Micro-Cracks and Shear Bands.

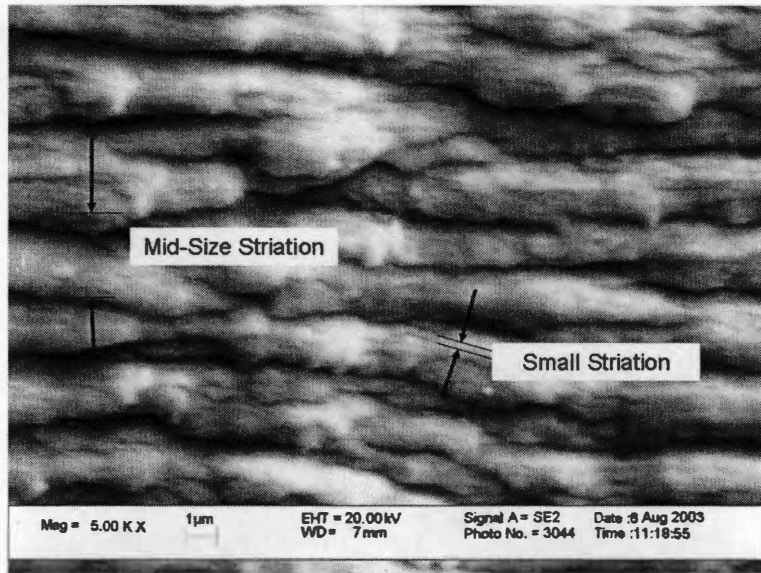


Figure A-71: Secondary Electron Image Illustrating Mid-Size and Small Striations. The Small Striations Are Associated with Individual Cycles.



Figure A-72: Secondary Electron Image of Mirror-Like Surface Near Crack Initiation Location.

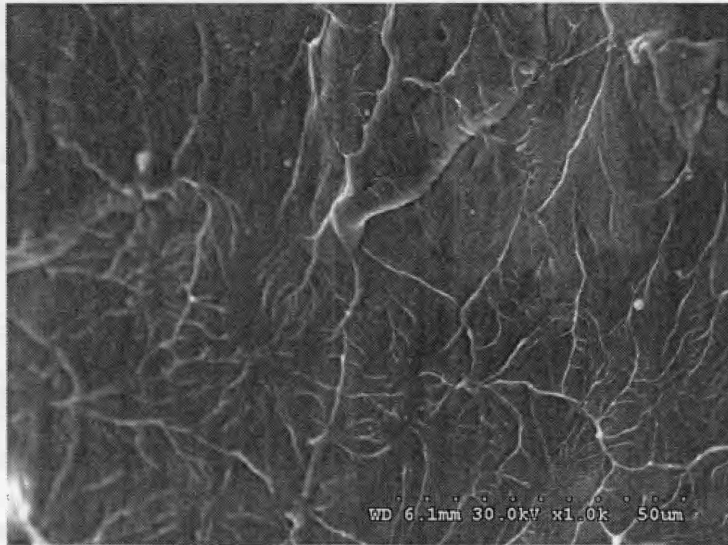


Figure A-73: Secondary Electron Image of the Vein Morphology Present in the Overload Fracture Surface of Sample 1 After Fatigue Test at 698 MPa.



Figure A-74: Secondary Electron Image of the Vein Morphology Present in the Overload Fracture Surface of Sample 1 After Fatigue Test at 698 MPa.

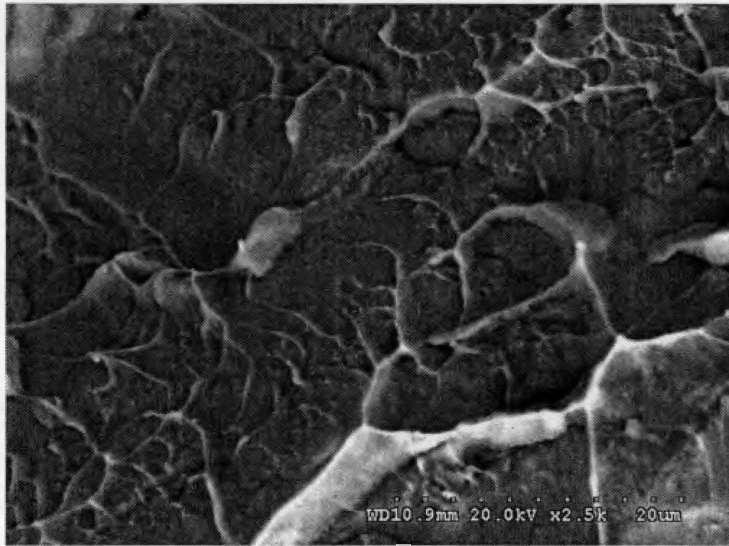


Figure A-75: Backscattered Electron Image of the Overload Fracture Surface of Sample 2 After Fatigue Test at 977 MPa.

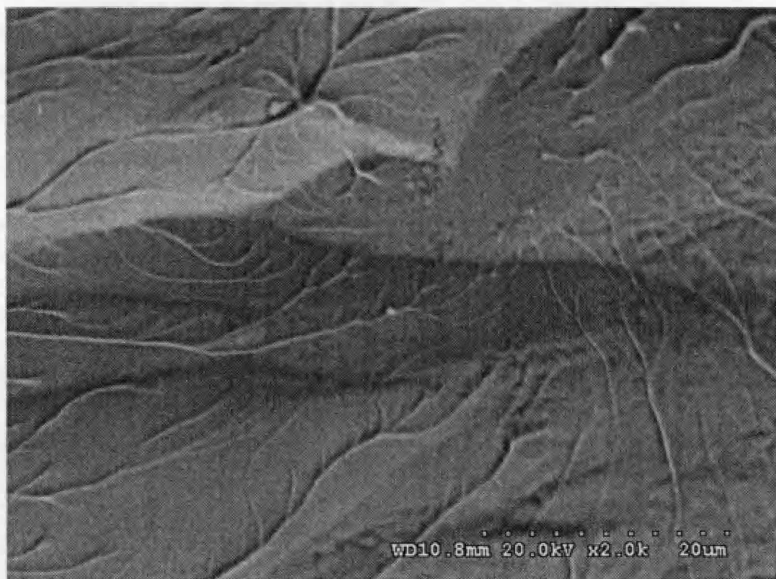


Figure A-76: Backscattered Electron Image of the Vein Morphology on the Shear Lip of Sample 2 After Fatigue Test at 977 MPa.

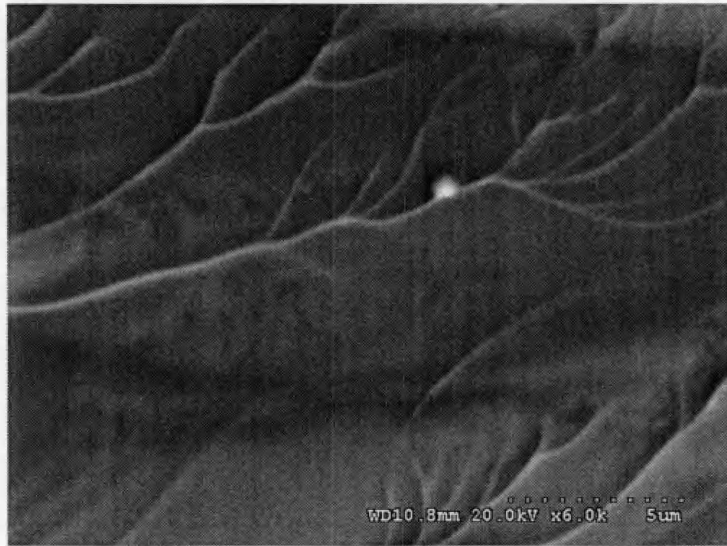


Figure A-77: Backscattered Electron Image of the Vein Morphology and a Liquid Droplet on the Shear Lip of Sample 2 After Fatigue Test at 977 MPa.

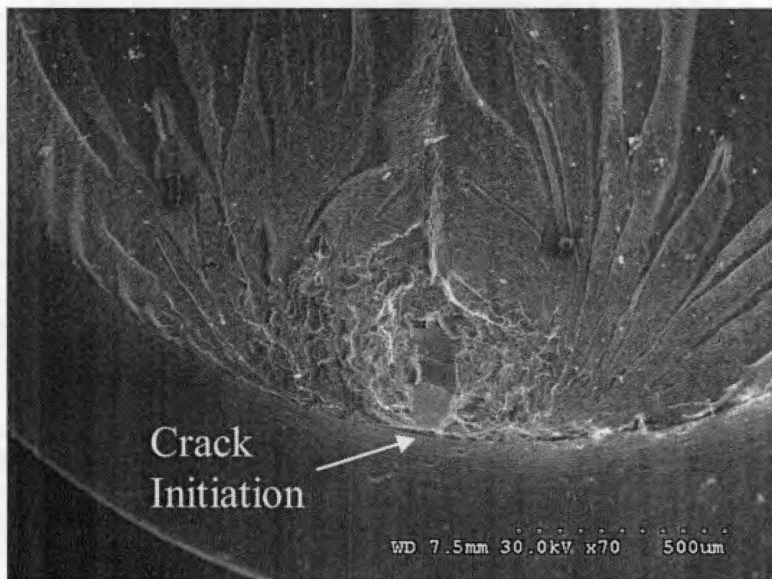


Figure A-78: Secondary Electron Image of the Fatigue Fracture Surface Around the Crack Initiation Site of Sample 1 After Fatigue Test at 698 MPa.

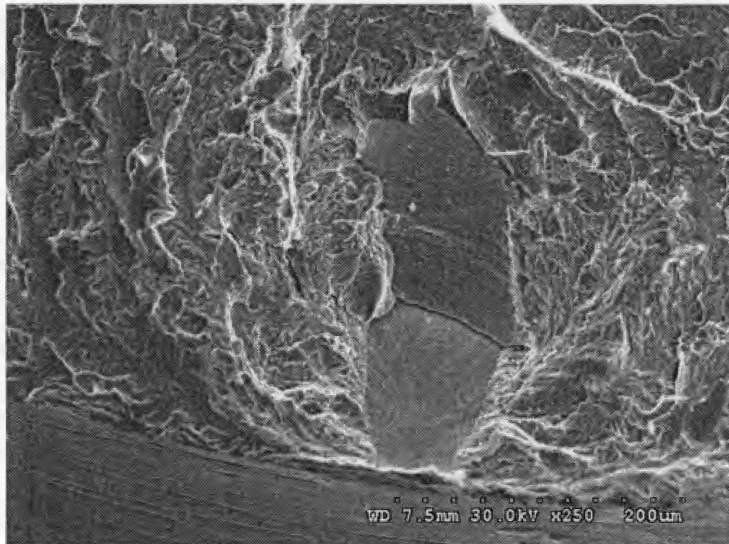


Figure A-79: Secondary Electron Image of the Crack Initiation Site of Sample 1 After Fatigue Test at 698 MPa.



Figure A-80: Backscattered Electron Image of the Crack Initiation Site of Sample 1 After Fatigue Test at 698 MPa.

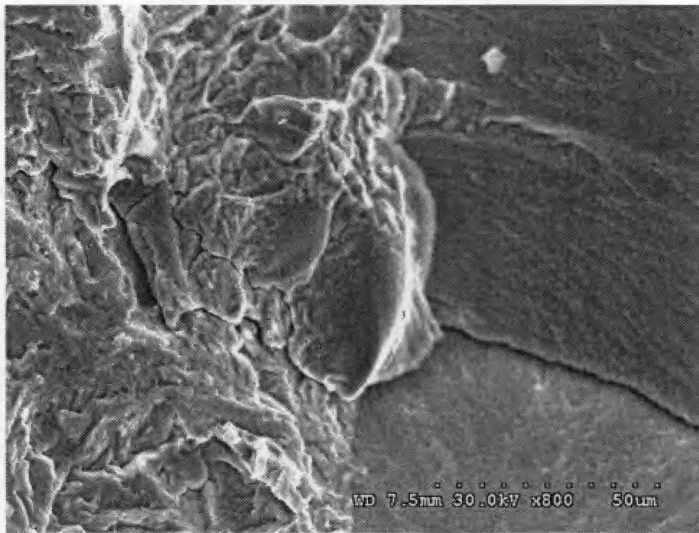


Figure A-81: Secondary Electron Image of a Crack Branching in the Low Area of the Planar Area of Sample 1 After Fatigue Test at 698 MPa.

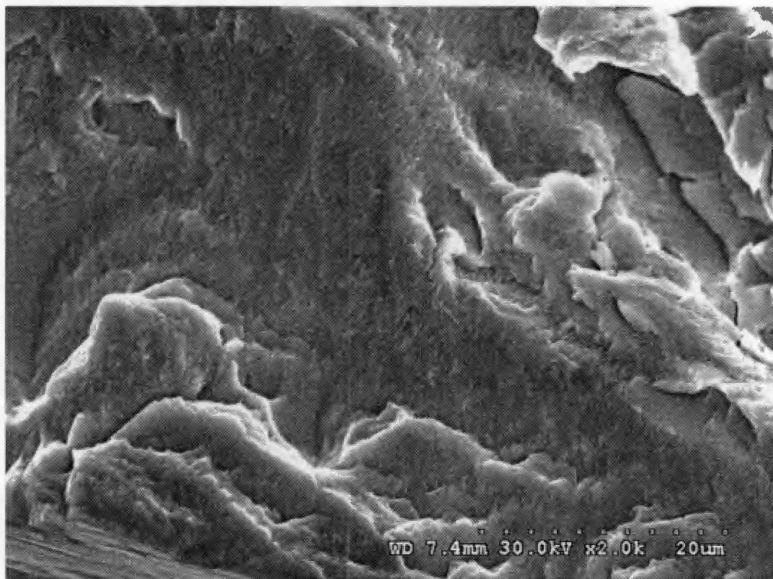


Figure A-82: Secondary Electron Image of the Area Surrounding the Crack Initiation Site (Left of the Site) of Sample 1 After Fatigue Test at 698 MPa.



Figure A-83: Secondary Electron Image of the Outer Surface of the Crack Initiation Site at a 10° Tilt of Sample 1 After Fatigue Test at 698 MPa.

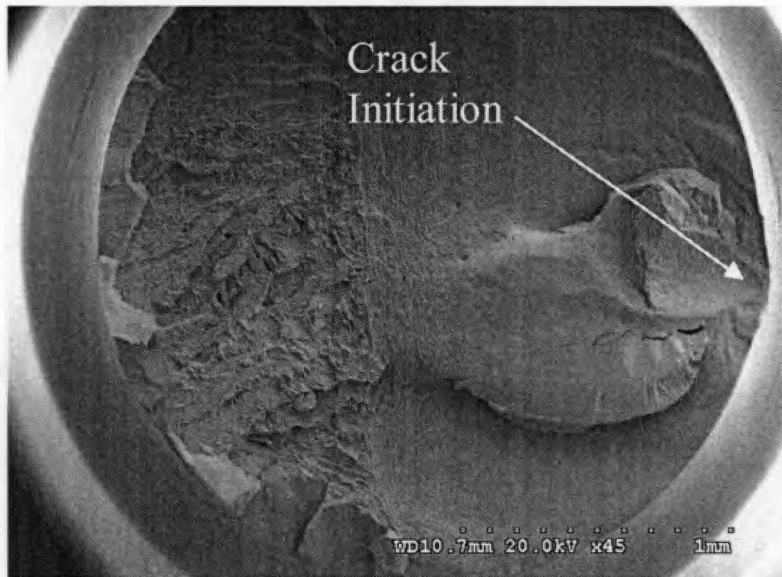


Figure A-84: Secondary Electron Image of the Fracture Surface of Sample 2 at Low Magnification After Fatigue Test at 977 MPa.

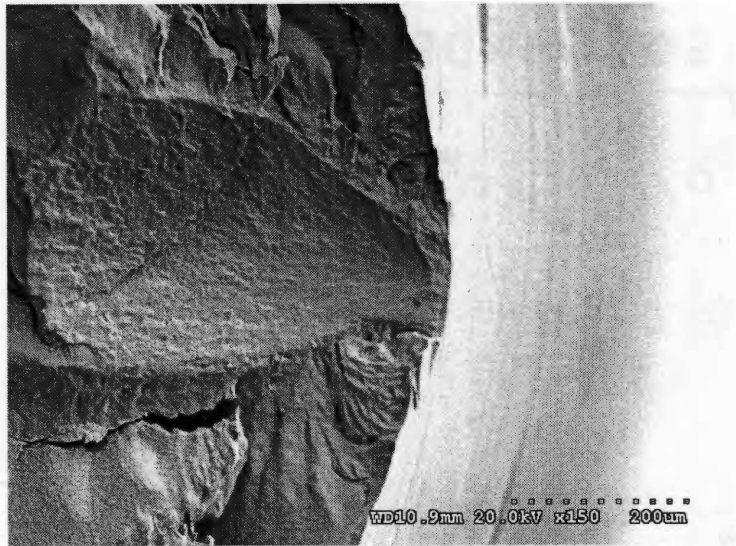


Figure A-85: Secondary Electron Image of the Crack Initiation Site of Sample 2 After Fatigue Test at 977 MPa.

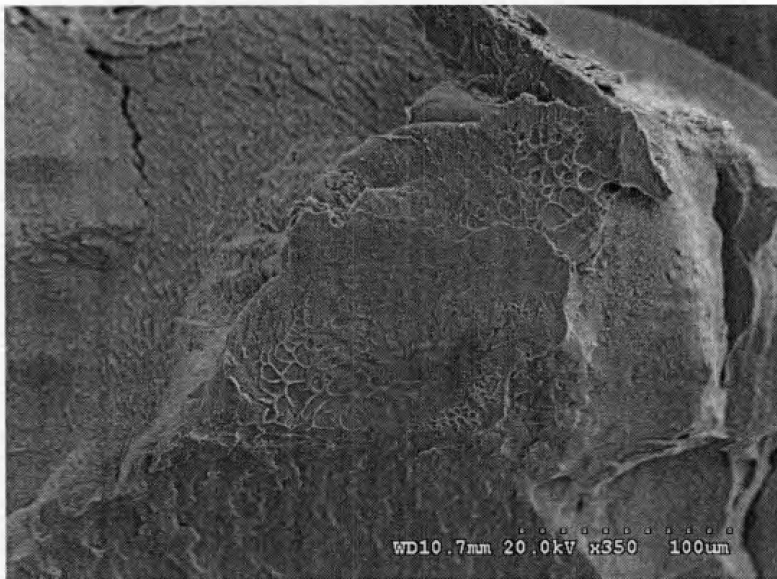


Figure A-86: Secondary Electron Image of the Protrusion in Proximity of the Crack Initiation Site (Right of Protrusion) of Sample 2 After Fatigue Test at 977 MPa.



Figure A-87: Backscattered Electron Image of the Plateau of the Protrusion of Sample 2 After Fatigue Test at 977 MPa.

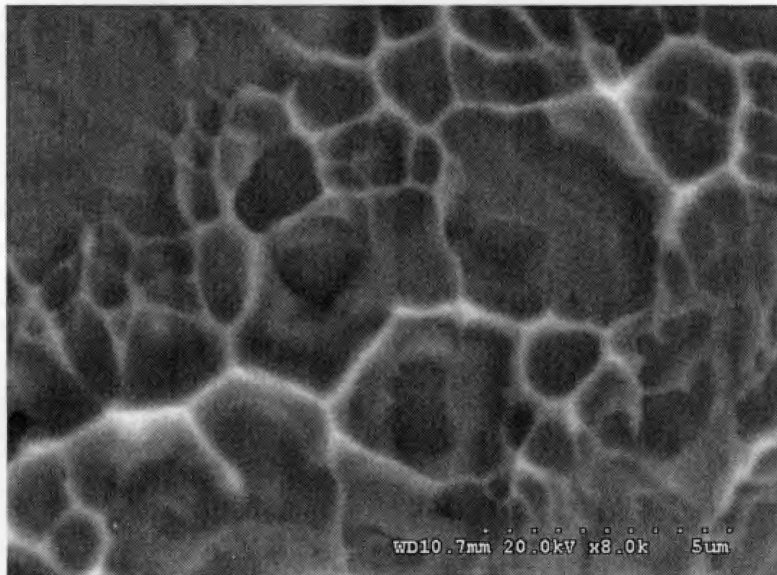


Figure A-88: Backscattered Electron Image of the Dimpling Found on the Top of the Plateau of Sample 2 After Fatigue Test at 977 MPa.

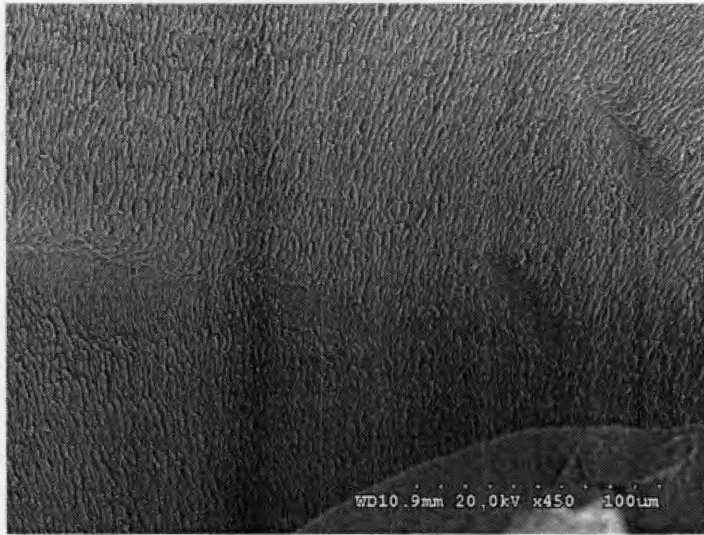


Figure A-89: Backscattered Electron Image of the Area Surrounding the Protrusion (Protrusion to the Bottom- Right) of Sample 2 After Fatigue Test at 977 MPa.

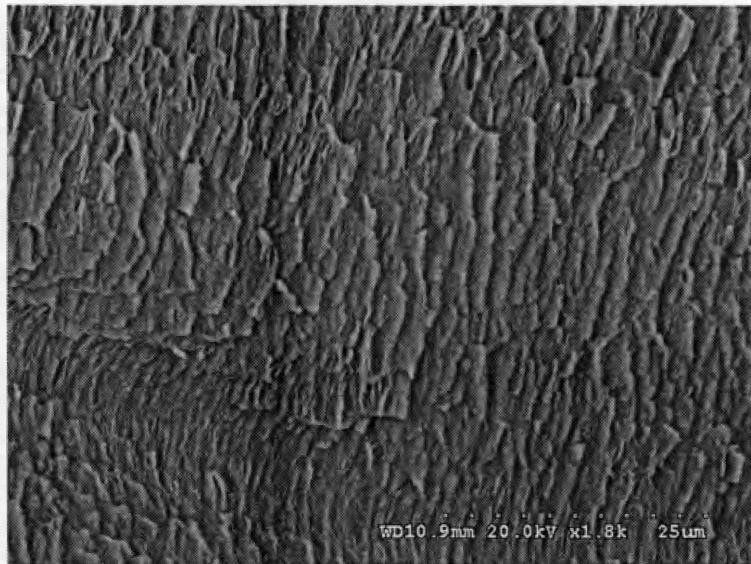


Figure A-90: Backscattered Electron Image of Striations Near the Protrusion of Sample 2 After Fatigue Test at 977 MPa.



Figure A-91: Backscattered Electron Image of the Crack Initiation Site (Opposite Half) of Sample 2 After Fatigue Test at 977 MPa.

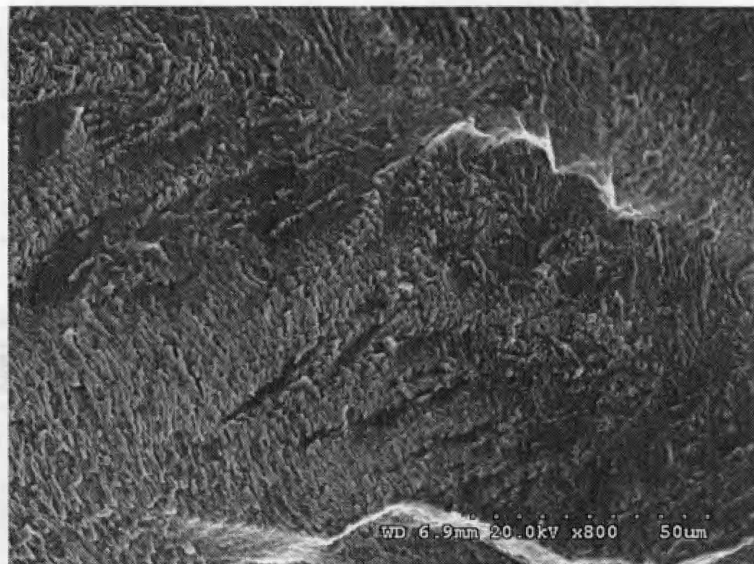


Figure A-92: Secondary Electron Image of the Depression of Sample 2 After Fatigue Test at 977 MPa.

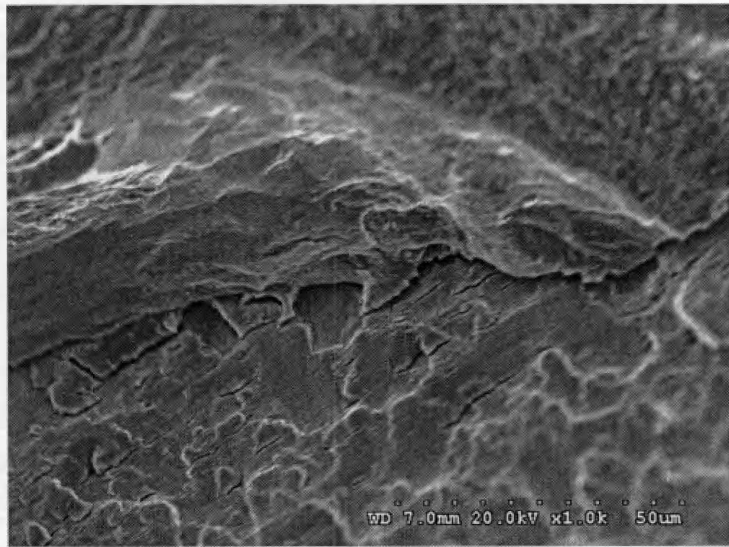


Figure A-93: Secondary Electron Image of Crack Branching at Bottom of Depression (Opposite Half) of Sample 2 After Fatigue Test at 977 MPa.

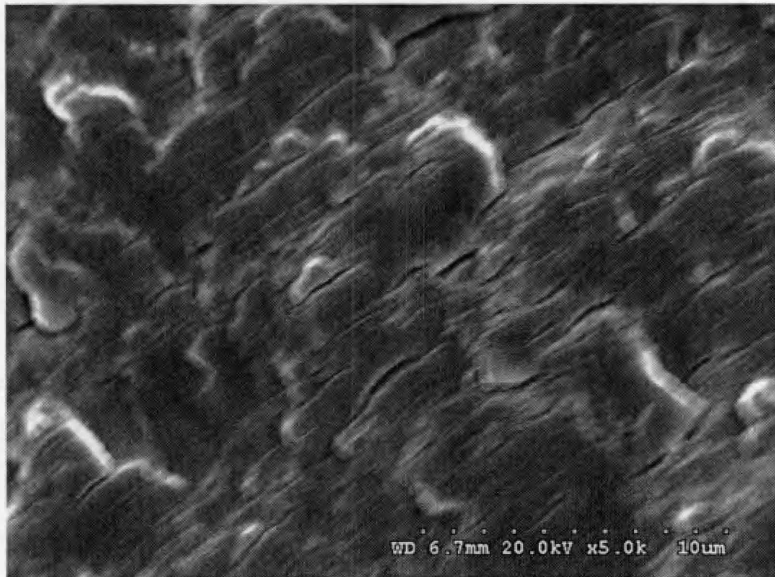


Figure A-94: Secondary Electron Image of Crack Branching of Sample 2 After Fatigue Test at 977 MPa.

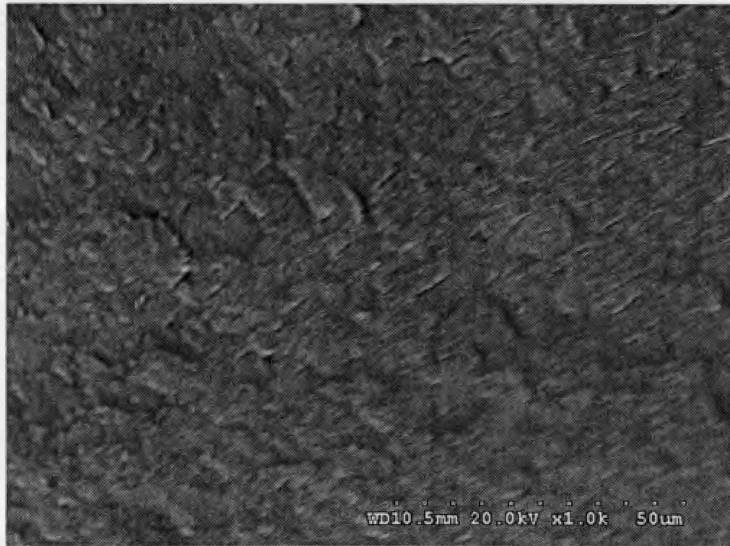


Figure A-95: Backscattered Electron Image of Crack Branching (Estimated Location of Dimpling) of Sample 2 After Fatigue Test at 977 MPa.

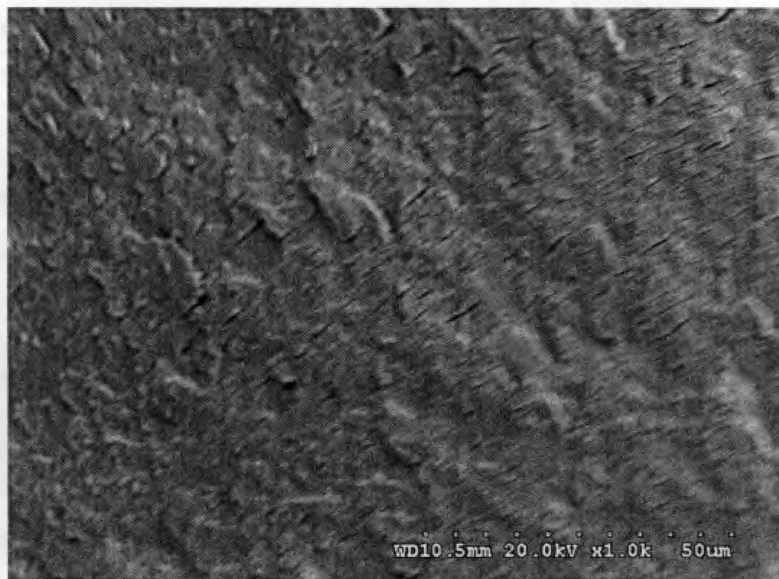


Figure A-96: Secondary Electron Image of Crack Branching (Estimated Location of Dimpling) of Sample 2 After Fatigue Test at 977 MPa.

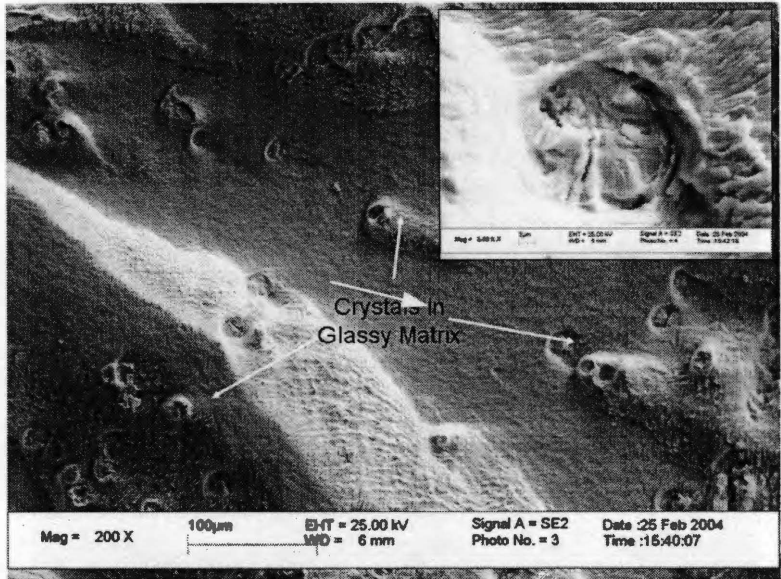


Figure A-97: Secondary Electron Images of Crystals in an As-Cast Amorphous Alloy. Crystals Are Either Protrusions Or Depressions. Higher Magnification of a Depression Is Inset.

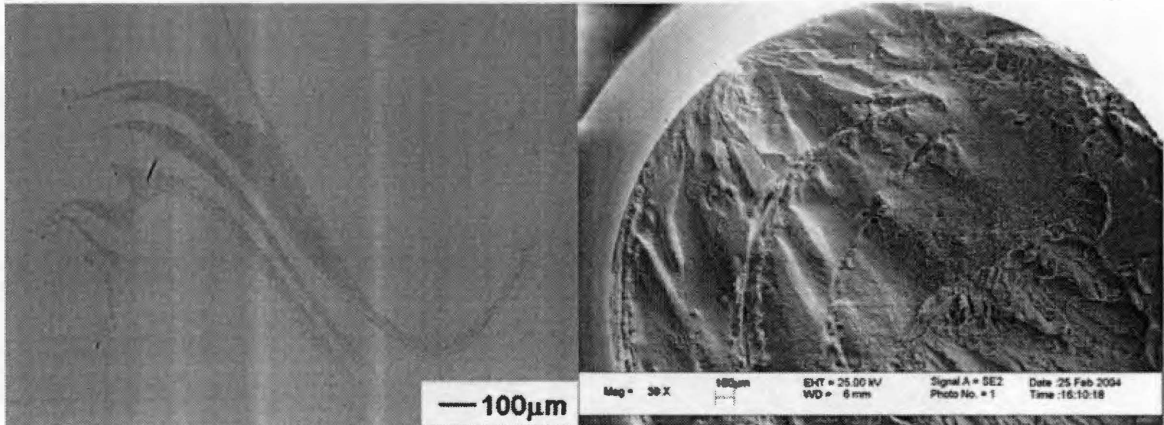


Figure A-98: Optical Microscopy Image of Crystalline Band in Polished and Etched BMG-11 Sample (Left) And Secondary Electron Image of Fracture Surface of Fatigue Sample Tested in Air (Right).

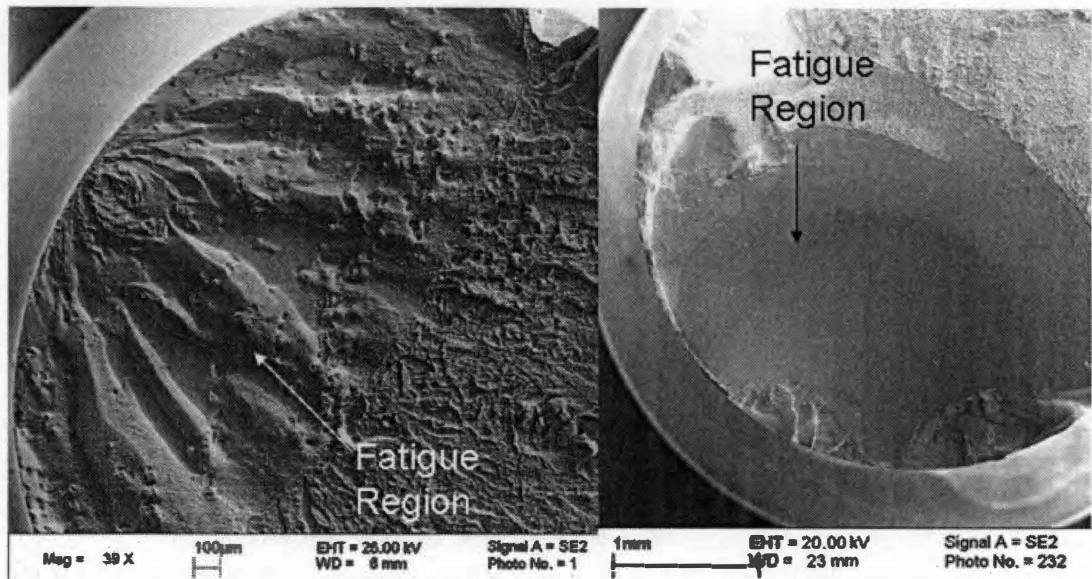


Figure A-99: Secondary Electron Images of Air Sample Tested at 907 MPa for $N_f = 282,785$ Cycles (Left), and Vacuum Sample Tested at 750 MPa for $N_f = 5.8$ Million Cycles (Right).

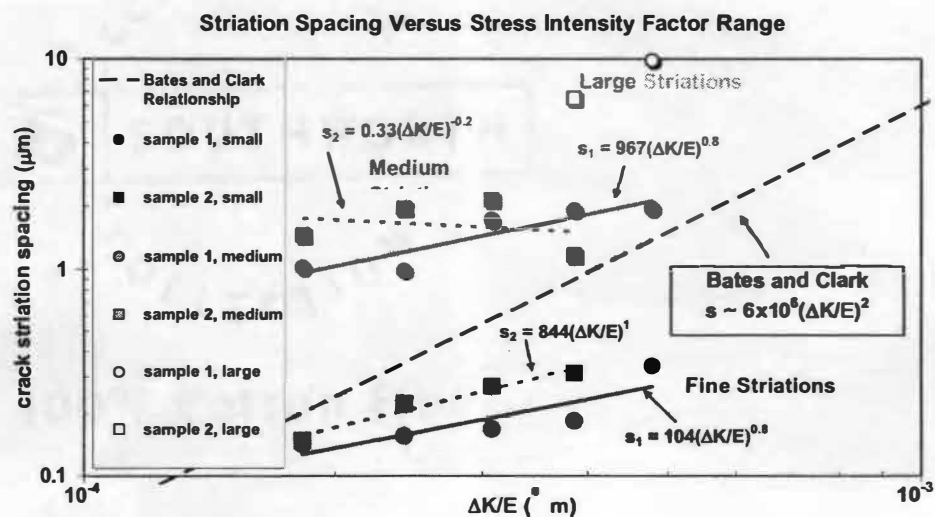


Figure A-100: Crack Striation Spacings for Small, Medium, and Large Striations of Two Samples Tested in Air Versus the Stress Intensity Range Divided by Young's Modulus. Results Are Displayed with the Bates and Clark Relationship [96] for Conventional Crystalline Materials.

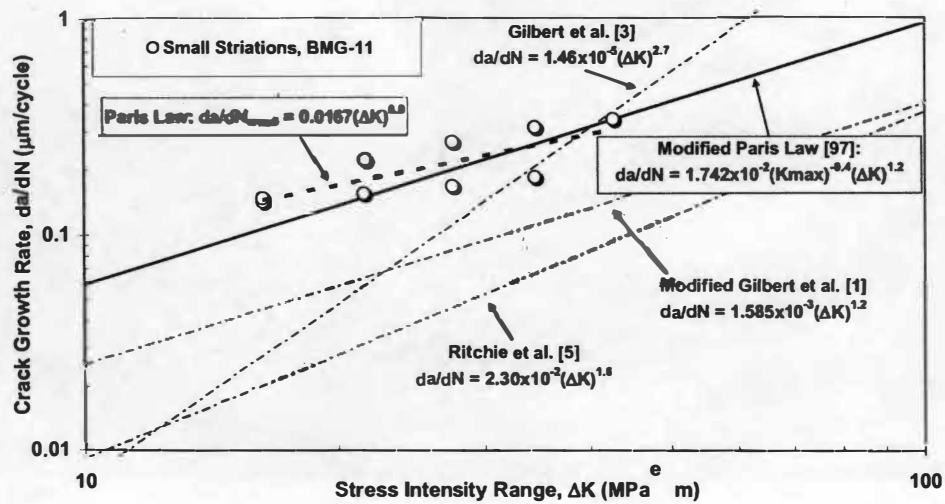


Figure A-101: Crack Growth Rates for Small Striations of Two Samples Tested in Air Versus the Stress Intensity Range. Results Are Compared with Gilbert et al. [1,3] and Ritchie et al. [5].

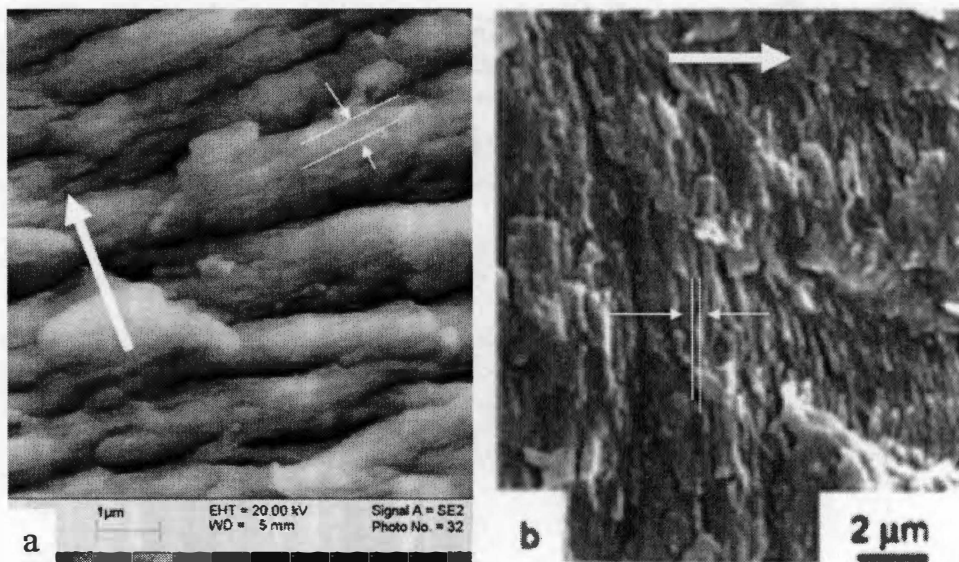


Figure A-102: Secondary Electron Images of Fatigue Striations. Striations Seem to Be Associated with Individual Cycles in BMG-11 on the Left (a), and Viterloy 1 [5] on the Right (b). Modified from Intermetallics, Volume 8, RO Ritchie et al., Fracture, Fatigue and Environmentally-Assisted Failure of a Zr-Based Bulk Amorphous Metal, p. 471, with Permission from Elsevier.

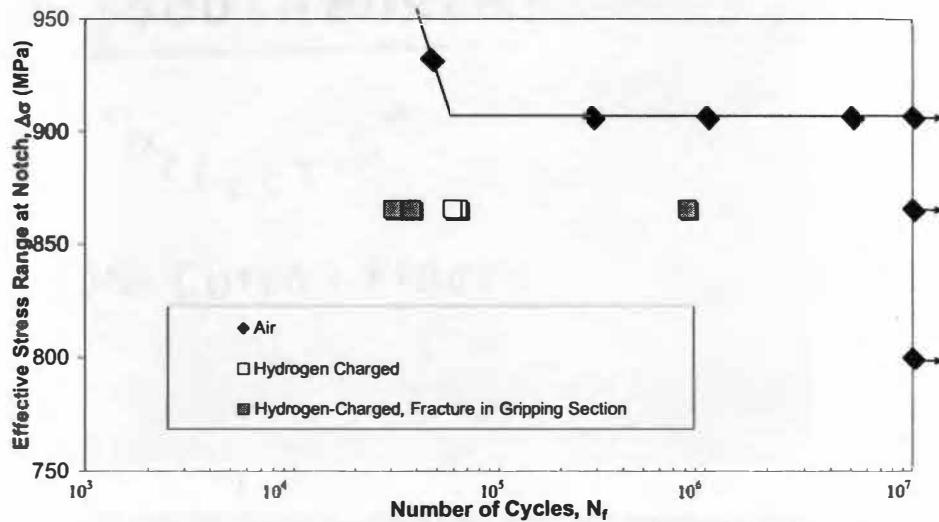


Figure A-103: Stress-Range / Fatigue-Life Data of Notched BMG-11 Specimens Tested in Air, but Cathodically-Charged with Hydrogen. The R Ratio Was 0.1 and the Frequency Was 10 Hz.

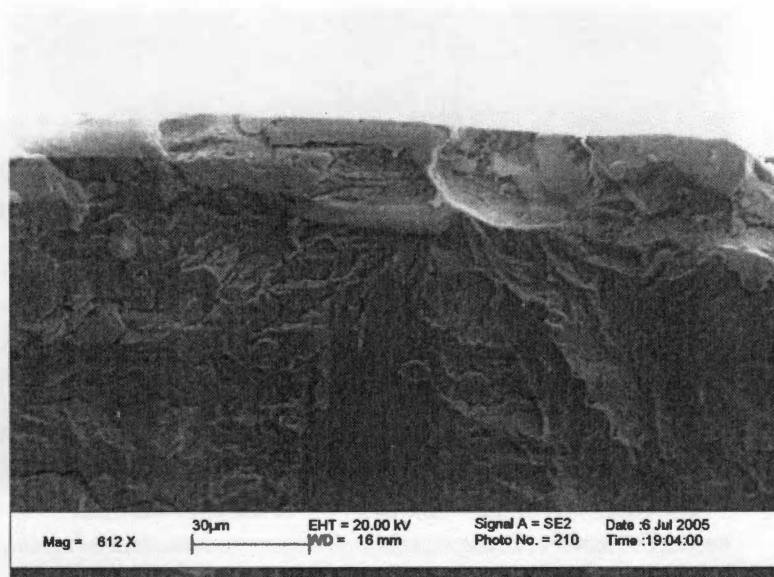


Figure A-104: Secondary Electron Image of Crack Initiation Surface of a Specimen Tested in Air, but Cathodically-Charged with Hydrogen.

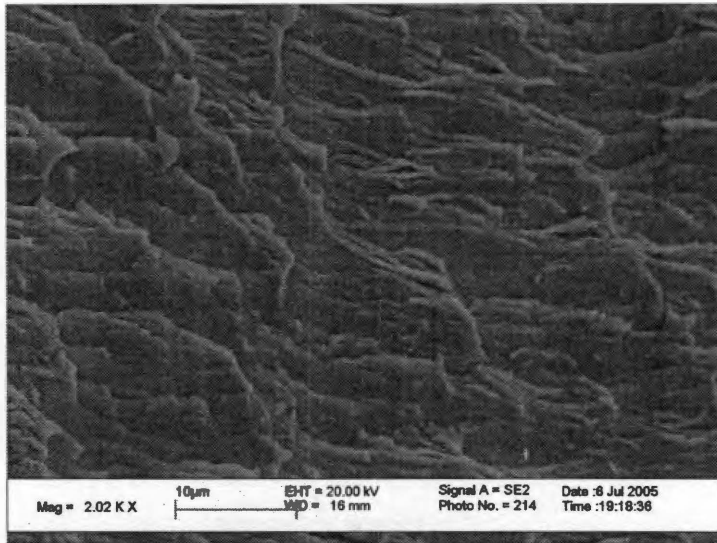


Figure A-105: Secondary Electron Image of the Fatigue Surface of a Specimen Tested in Air, but Cathodically-Charged with Hydrogen.

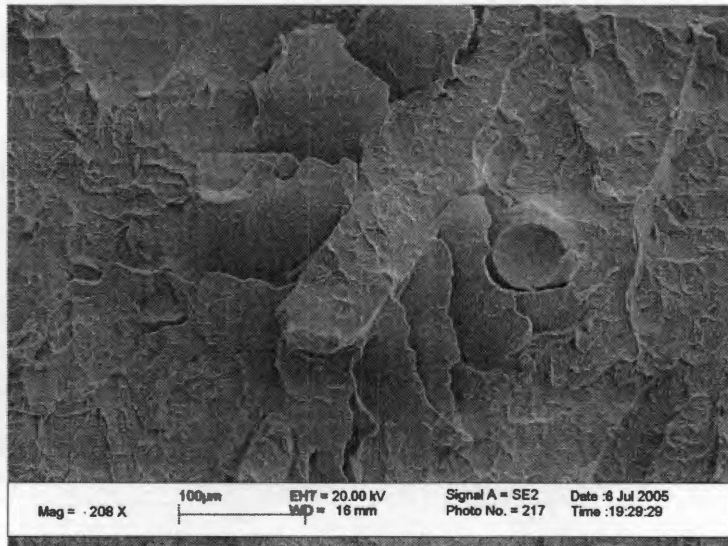


Figure A-106: Secondary Electron Image of Overload Fracture Surface of a Specimen Tested in Air, but Cathodically-Charged with Hydrogen. Note Unusual Peeled-Like Morphology.

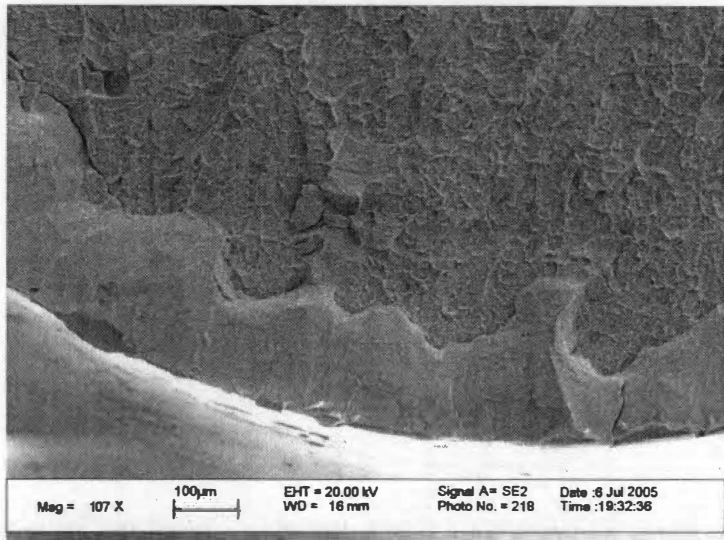


Figure A-107: Secondary Electron Image of a Shear Lip of a Specimen Tested in Air, but Cathodically-Charged with Hydrogen.

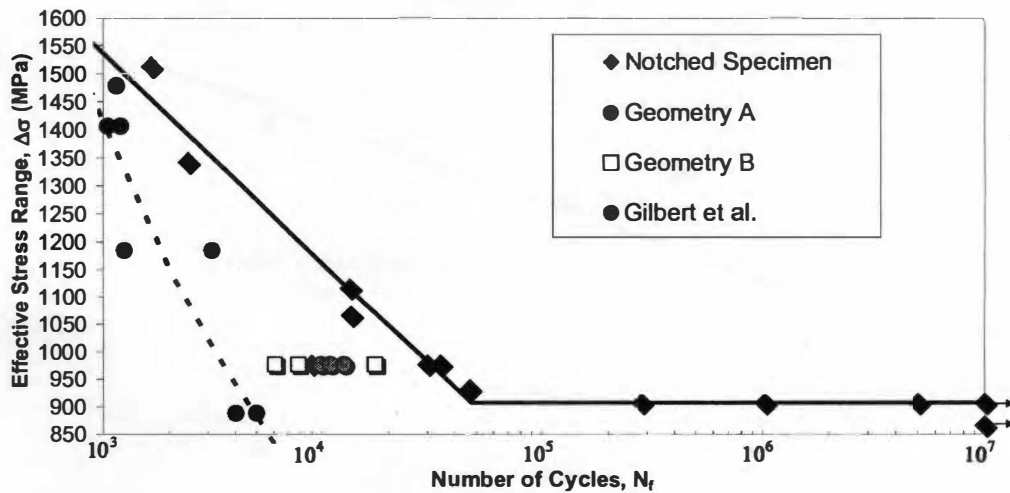


Figure A-108: Stress-Range / Fatigue-Life Data of Notched BMG-11 Specimens Compared with Specimen Geometries A and B, and Gilbert et al.'s Results [1-4]. The R Ratio Was 0.1 and the Frequency Was 10 Hz.

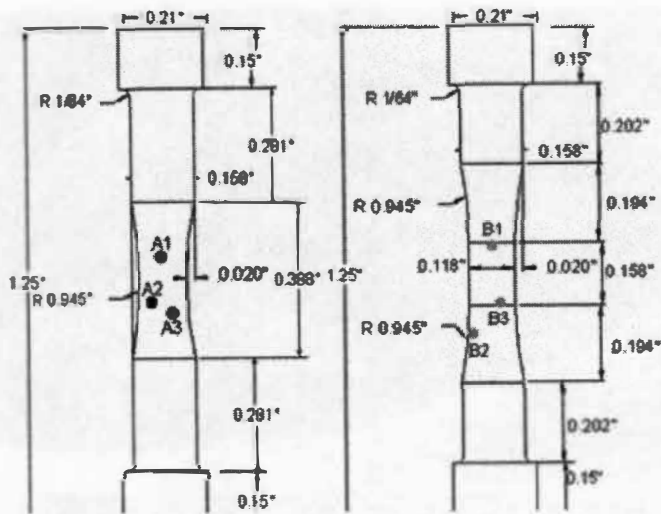


Figure A-109: Relative Locations of Crack Initiation/ Fracture Surface for Geometry A (Left) and Geometry B (Right).

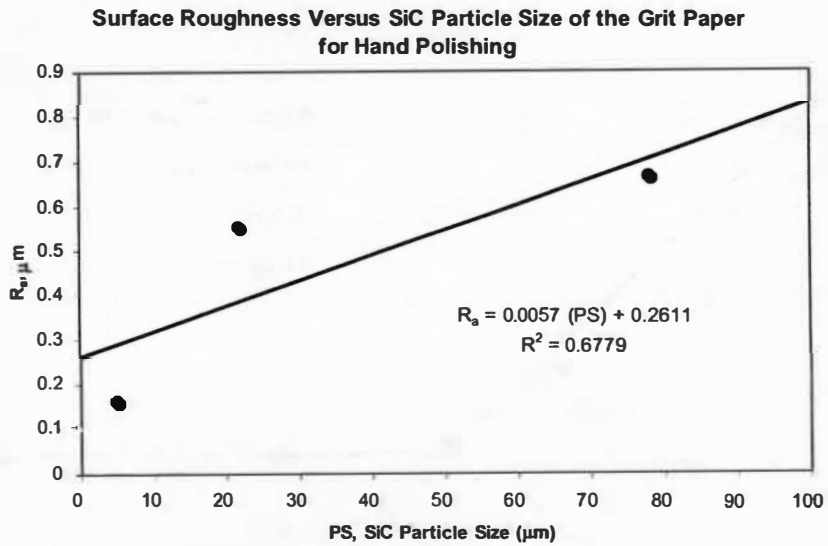


Figure A-110: Surface Roughness, R_a , Versus Particle Size of Silicon Carbide Grinding Paper for BMG-11.

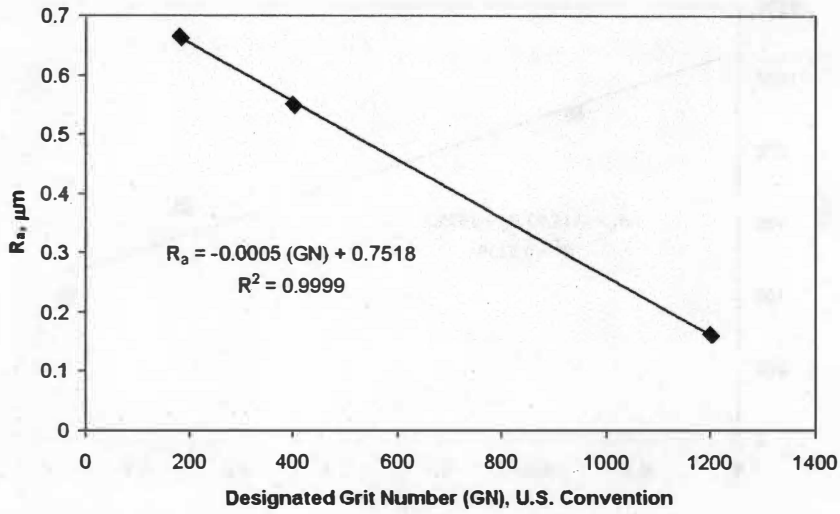


Figure A-111: Surface Roughness, R_a , Versus U.S. Designated Grit Number of Silicon Carbide Grinding Paper for BMG-11.

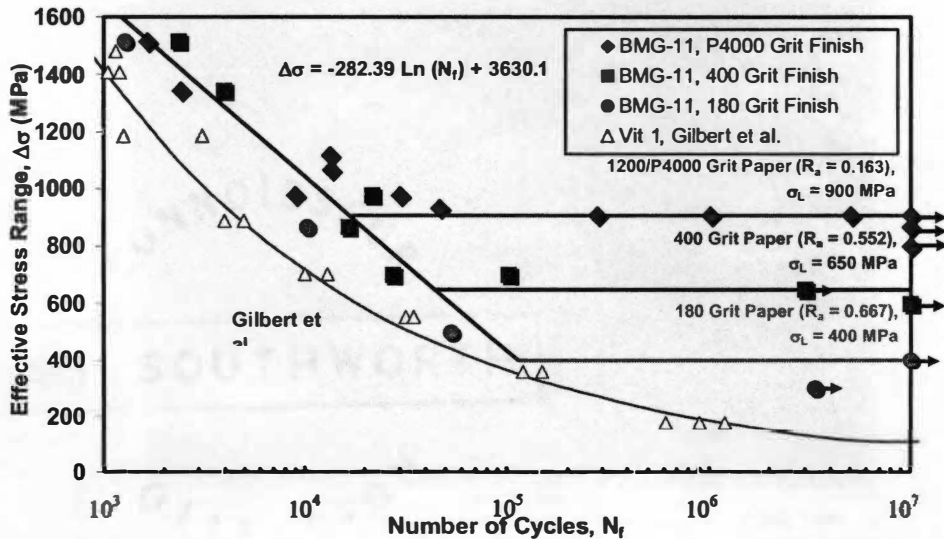


Figure A-112: Comparing the Stress-Range / Fatigue-Life Data of Notched BMG-11 Specimens Tested in Air with Various Finishes. The R Ratio Was 0.1 and the Frequency Was 10 Hz.

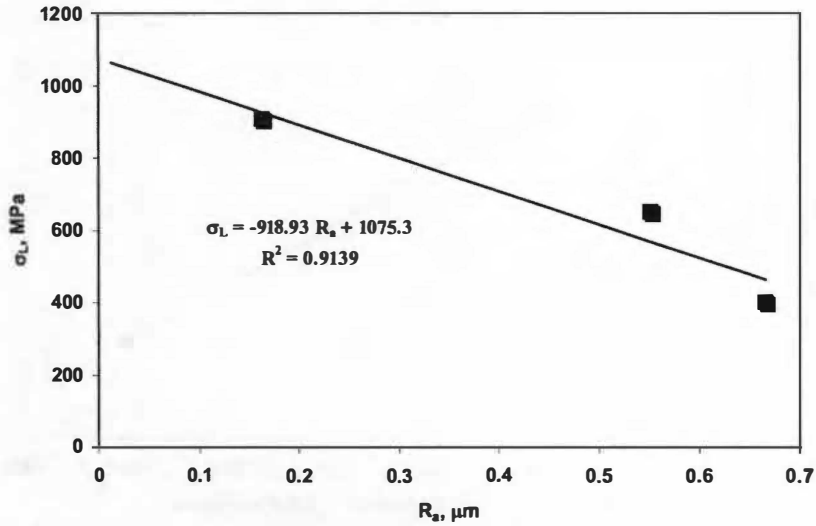


Figure A-113: Fatigue Endurance Limit Versus the Surface Finish for BAM-11.

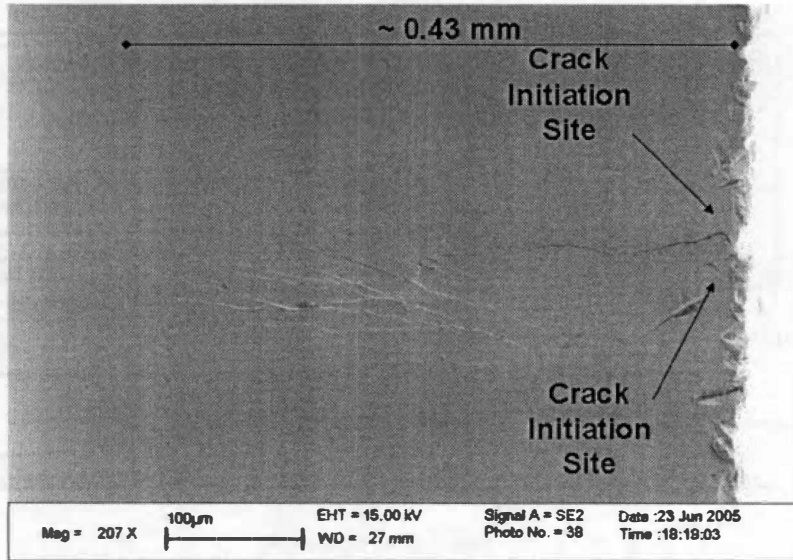


Figure A-114: Secondary Electron Image of Crack in a Square Beam, 3-Point Bend Specimen Finished with 180 Grit Paper.

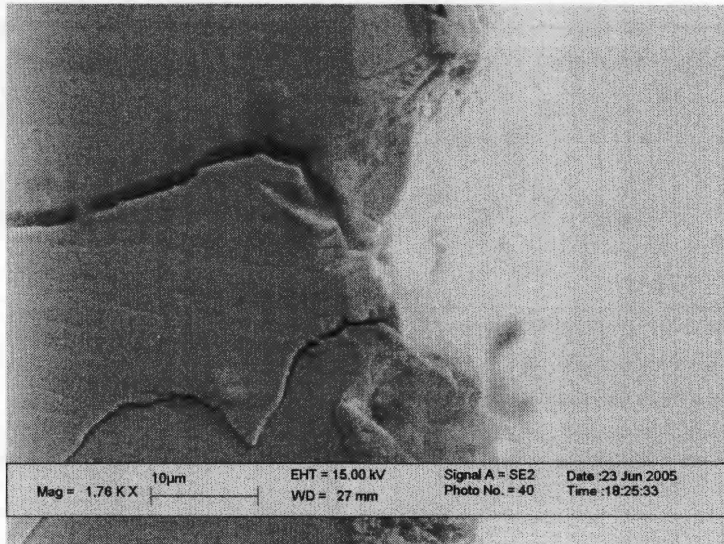


Figure A-115: Secondary Electron Image of the Two Crack Initiation Locations in a Square Beam, 3-Point Bend Specimen Finished with 180 Grit Paper.

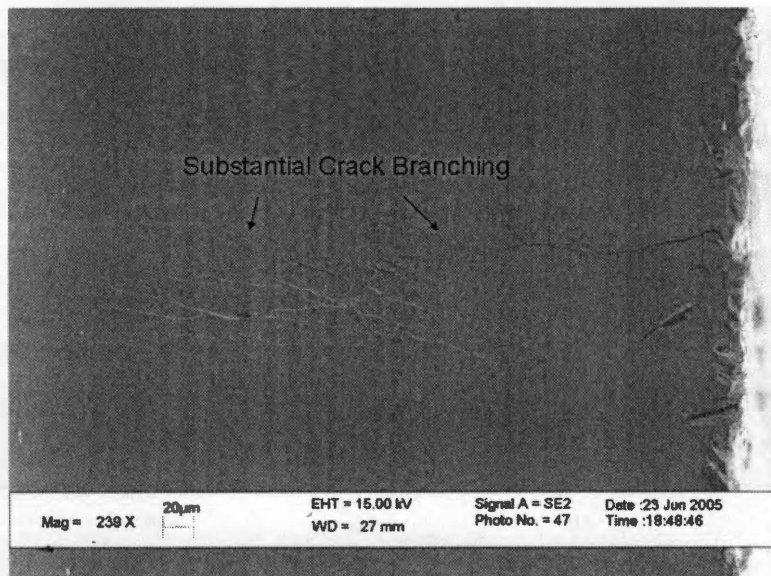


Figure A-116: Secondary Electron Image of the Severe Crack Branching that Occurs to a Square BMG-11 Beam Tested in 3-Point Bending with 180 Grit Paper Finish.

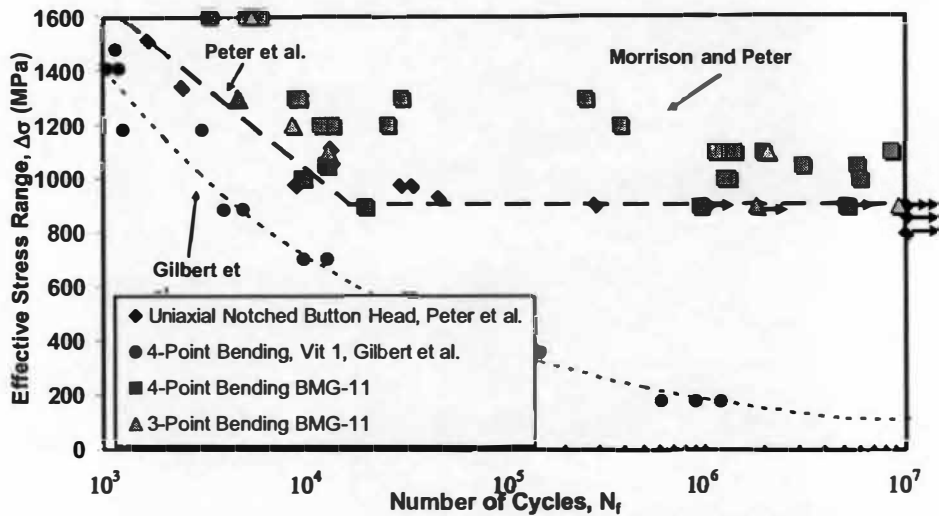


Figure A-117: Stress-Range / Fatigue-Life Data of 3-Point Bending [101], 4-Point Bending [100], and Uniaxial BAM-11 Specimens Tested in Air [6,7]. Gilbert et al.'s 4-Point Bending Results for Vit. 1 Are Included [1-5]. The R Ratio Was 0.1 and the Frequency Was 10 Hz.

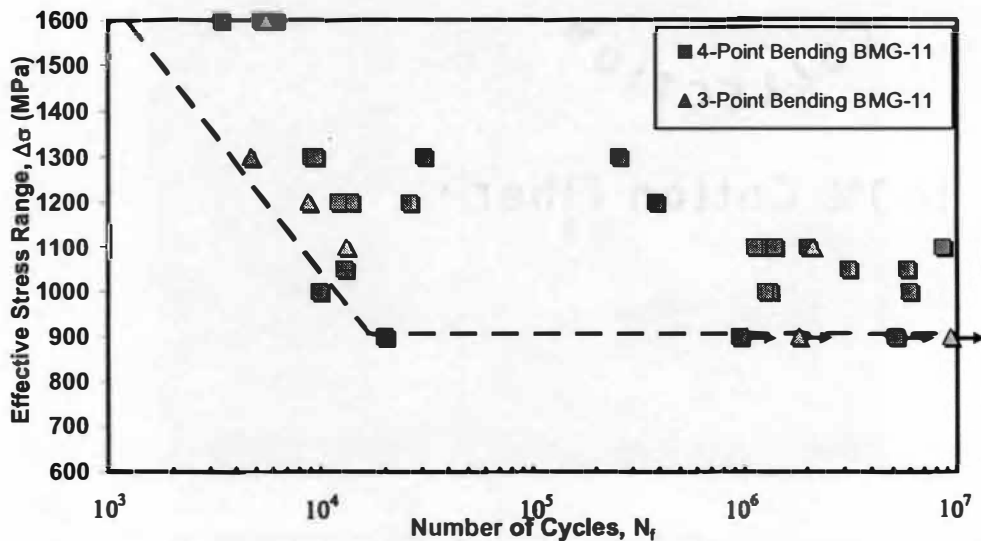


Figure A-118: Stress-Range / Fatigue-Life Data of 3-Point Bending [101] and, 4-Point Bending [100]. Arrows Indicate the Sample Did Not Fracture. The R Ratio Was 0.1 and the Frequency Was 10 Hz.

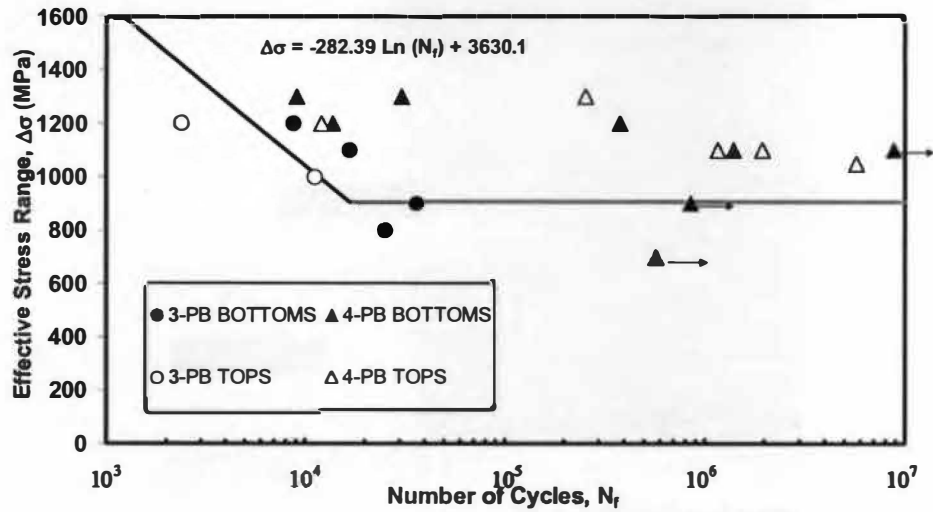


Figure A-119: Stress-Range / Fatigue-Life Data of 3-Point Bending and 4-Point Bending BMG Specimens Tested in Air Designating Whether the Sample Came from the Top or the Bottom of the Ingot. The R Ratio Was 0.1 and the Frequency Was 10 Hz.

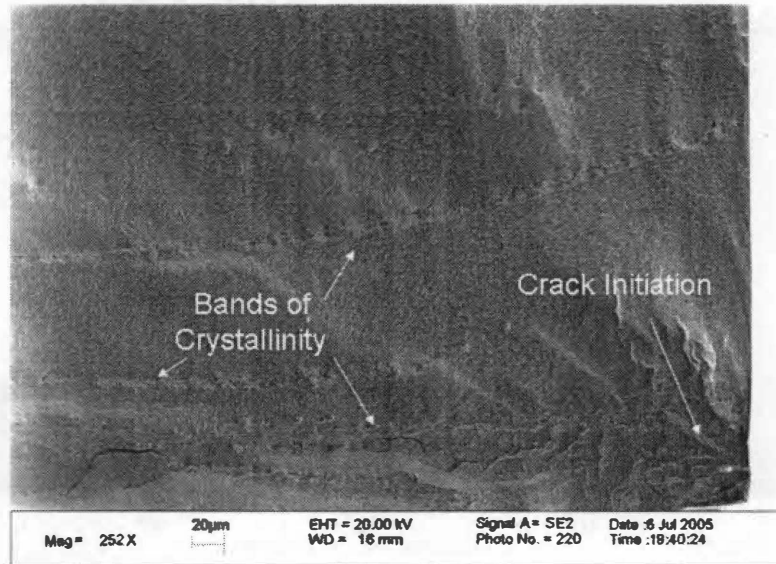


Figure A-120: Secondary Electron Image of Fracture Surface in the Fatigue Region of 3-Point Bend Specimen that Failed Near 13,000 Cycles. Notice Crystalline Band Running Near the Crack-Initiation Site. Another Sample from the Same Ingot Underwent Over 1 M Cycles.

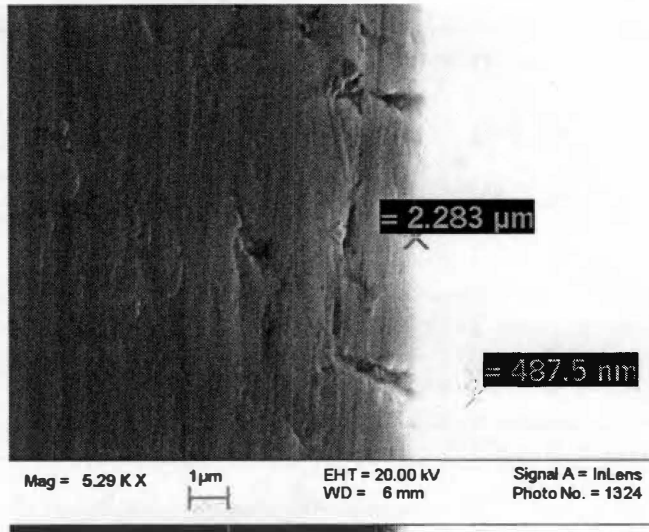


Figure A-121: An In-Lens, Secondary Electron Image of the Surface Finish Near the Corner of a Polished Beam Specimen Before Testing.

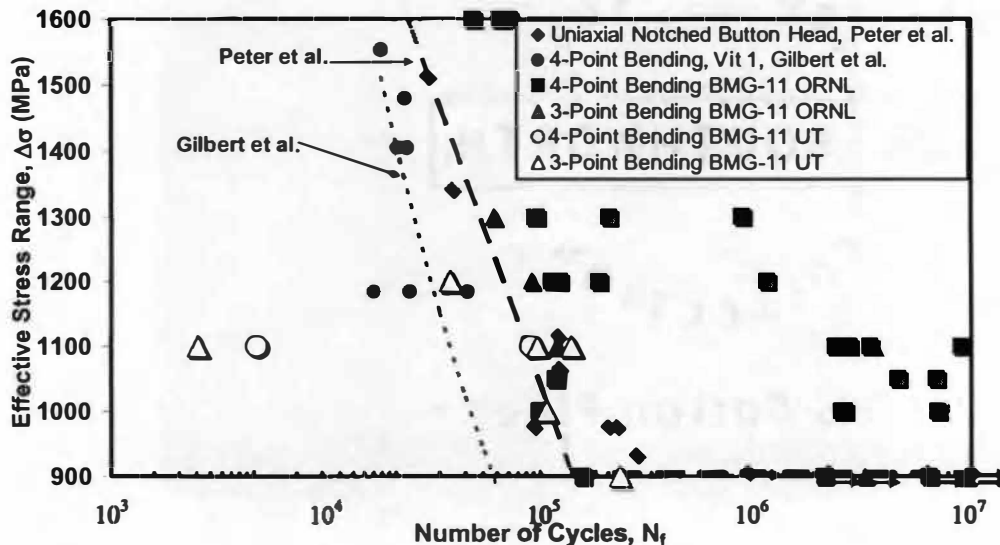


Figure A-122: Stress-Range / Fatigue-Life Data of 3-Point Bending, 4-Point Bending and Uniaxial BAM-11 Specimens Tested in Air with Low Results from Samples Made Using New Arc Furnace (UT). Gilbert et al.'s 4-Point Bending Results for Vit. 1 Are Included [1-5]. The R Ratio Was 0.1 and the Frequency Was 10 Hz.

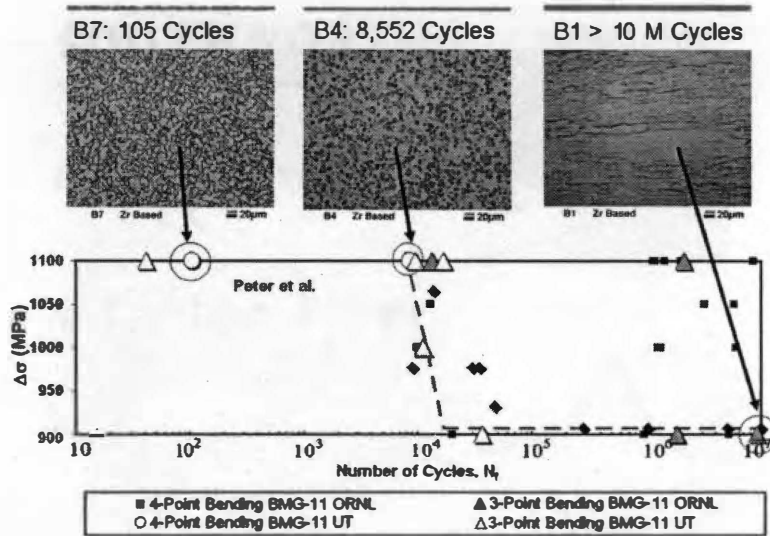


Figure A-123: Optical Micrographs of Two Samples Tested at 1,100 MPa and Compared with a BMG-11 Sample that Underwent 1 M Cycles at 900 MPa. The R Ratio Was 0.1 and the Frequency Was 10 Hz.

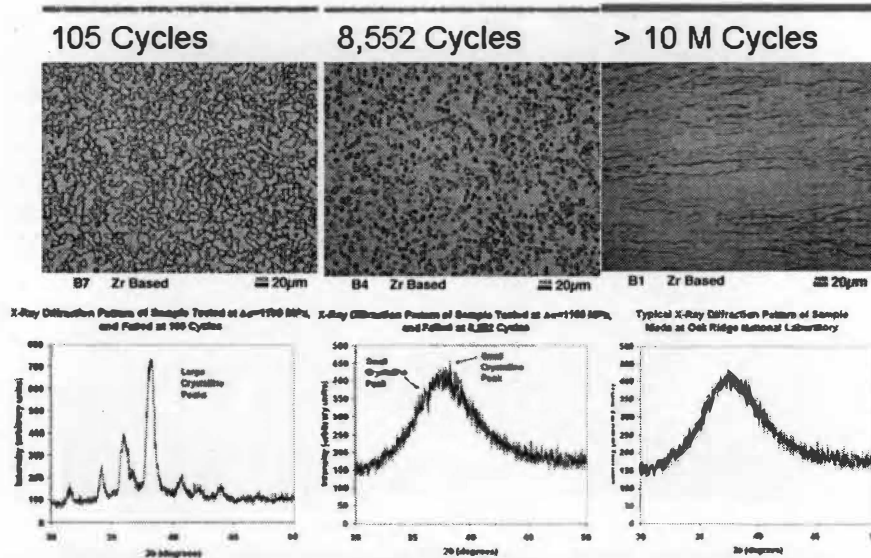


Figure A-124: Optical Micrographs and X-Ray Diffraction Patterns of Two Samples Tested at 1,100 MPa and Compared with a BMG-11 Sample that Underwent 1 M Cycles at 900 MPa.

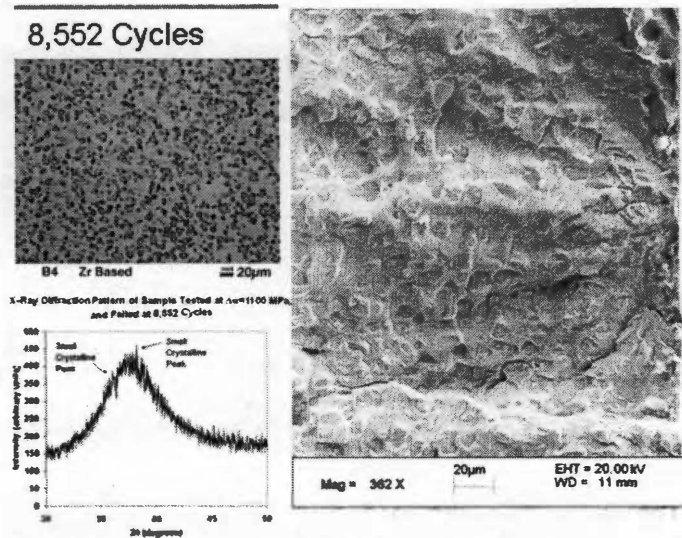


Figure A-125: Optical Micrograph, X-Ray Diffraction Pattern, and Secondary Electron Image of the Sample Tested at 1,100 MPa and Failed at 8,552 Cycles.

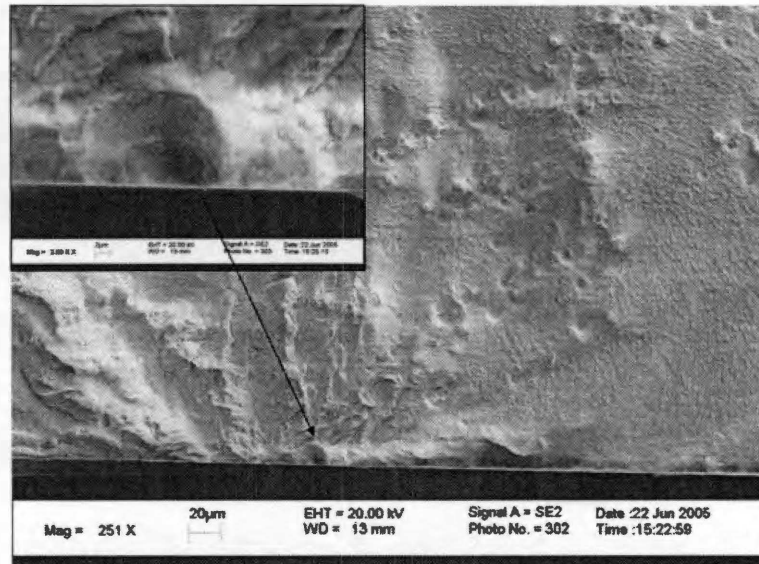


Figure A-126: Secondary Electron Images of Fatigue Area of Fracture Surface of Specimen T4. Crack Initiated at a Crystal.

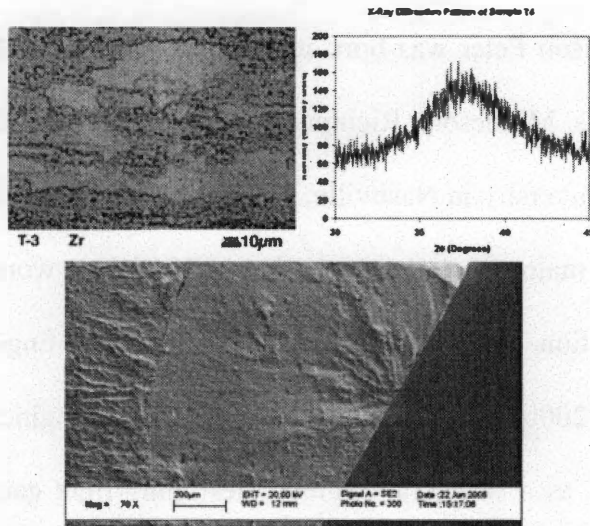


Figure A-127: Optical Micrograph, X-Ray Diffraction Pattern, and Secondary Electron Image of the Sample Tested at 1,100 MPa and Failed at 9,562 Cycles.

VITA

William Hutchison Peter was born in Columbus, Ohio on March 24, 1974. He grew up in Minneapolis, Minnesota; Richmond, Virginia; and Knoxville, Tennessee. He attended Vanderbilt University in Nashville, Tennessee, and graduated with a Bachelor's of Engineering with a major in civil engineering in 1996. He worked as a geotechnical engineer and construction materials lab manager for Patrick Engineering, Inc for two years. From 1998 to 2000, Mr. Peter worked at Structural Engineering Solutions, LLC and Metal Truss, LLC as a structural engineer designing light gauge steel framing and trusses. He enrolled in the department of Materials Science and Engineering at the University of Tennessee, Knoxville, in the summer of 2000. He spent five years studying the lifetime science of advanced materials. Specifically, Mr. Peter has performed research in the fatigue and corrosion of metallic glasses. In 2002, Mr. Peter received a Master of Science; and in 2005, he received a Doctor of Philosophy in Materials Science and Engineering, both in the major of Materials Science and Engineering.

William Hutchison Peter is currently engaged in a post-doctorate fellow position at the Oak Ridge National Laboratory in Oak Ridge, Tennessee. He is in the Materials Processing Group of the Metals and Ceramics Division studying the processing of intermetallics, metallic glasses, and other advanced materials.

4535 0545 15
11/09/05 HFB